UCLouvain

epl

École polytechnique de Louvain

Tuning Residual Stresses in Ultrathin Membranes for Resonant Frequency Control

Author: **Eléonore Masarweh**
Supervisors: **Denis Flandre, Laurent Francis**
Readers: **Jean-Pierre Raskin, Nicolas André**
Academic year 2020–2021
Master [120] in Electro-mechanical Engineering

Abstract

This master thesis proposes a design and fabrication process for ultrathin CMOS-compatible membranes with resonant frequency tuning enabled by residual stress control in thin film stack.
In recent years, interest towards non-invasive monitoring of industrial high-voltage power electronics equipment has strongly increased, especially in the field of partial discharge detection. Partial discharges are incomplete dielectric breakdown in electric insulation material causing long term deterioration and eventually destruction of the affected piece of equipment. Such events can be detected using membrane based ultrasound microphones. This works explores the possibility to increase the sensitivity and the embeddability of membranes.
A simple analytical design process based on Matlab modeling is proposed and confirmed by Comsol simulations of multilayer membranes. Eight designs are proposed, four square and four circular designed for resonant frequencies ranging from 70kHz to 300kHz. The design parameters are the thickness of the membrane, its width and the equivalent residual stress across the full thin film stack and are respectively fixed at 1µm, 400 to 1600µm and 50MPa. Simulations and models show close alignement within less than 5% for first mode resonant frequency.
Fabricated membranes have measured thickness around 975nm, width within 40µm margin above the design and measured equivalent residual stress in stack around 70MPa. They are characterized using laser vibrometry. Their measured first mode resonant frequency lies within a 5% error margin around the expected value from models. Comparison between detected frequency for higher mode and Comsol simulation results show maximum 20% of error.

Aknowledgements

The months that lead to the completion of the present work were a steep learning curve for me. This was made possible thanks to the support of numerous persons.

First, I would like to thank my two promotors Prof.Denis Flandre and Prof. Laurent Francis. Their follow-up of my work, their availability and their guidance was of great help in the elaboration and the realization of this master thesis. Their advice was really precious at every step of the work.

The support received from Nicolas André makes me feel very grateful: his answers to my constant questions and the countless hours of training and supervision in the Winfab and on the measurement setups in the Welcome were key to my ability to complete the process. He is always up to discuss about the results or the next steps. His ability to come up with tons of new ideas every time he blinks never fails to amaze me. He helped me sharpen my curiosity for scientific research and build trust in my results at the same time.

I also thank Thibault Delhaye for the sharing of his Comsol expertise and ability to rescue any broken simulation; Iman Sabri Alirezaei for the opportunity to add my designs to his for the photomask order and Prof. Fares Tounsi for the discussions about context and possible applications.

I aknowlegde the generous help of the Winfab staff : Michael Coulombiers, Christian Renaux, Miloud Zitout and Sebastien Faniel for their advice on specific steps, their availability, their expertise and their help with the use of some machines. I also have a thought for those who I shared spaces and machines with during the process : Marie-Stéphane Colla, Roselien Vercauteren, the VOCSens team, and all others. Specials thought goes to all of those who had to share the Oxford Plasmalab machine with me these last weeks : Romain Tuyaerts and Quentin van Overmeere, your patience and your flexibility were really nice.

I am really grateful to the A.188 office team for welcoming me those last months and offering me a comfortable workspace and a great atmosphere for the data processing and redaction steps.

Last but not least, I can not forget all the friends I have lived incredible experiences with during these years, especially Charline van Innis, for every shared moment, be it the hard ones or the most exciting ones, and Pauline de Crombrugghe for our shared beginings in the adventure towards the smaller dimensions. My family also receives a special thought for their presence and support throughout my full academic path, especially my dad for reading my work. And I could not be too grateful to my partner, Martin Lefebvre, for helping me believe in my abilities and his encouragements about my "not that bad" work.

Contents

List of Figures vi

List of Tables ix

1 Introduction 1

2 State of The Art 3
2.1 Partial discharges . . . 3
2.1.1 Description of the phenomenon . . . 3
2.1.2 Consequences . . . 5
2.1.3 Emitted signals and detection of partial discharges . . . 5
2.2 Context of this work . . . 6
2.3 PD detection using AE sensing . . . 6
2.3.1 AE signal characteristics . . . 6
2.3.2 Current sensors for PD detection trough AE sensing . . . 7
2.4 Membranes and resonant behavior . . . 9
2.4.1 Defining membranes in theory and MEMS fabrication contexts . . . 9
2.4.2 Basic of static mechanical behavior of membranes and their use in transduction 11
2.4.3 Resonant behavior of membranes . . . 11
2.4.4 Stress control in material stacks for membranes . . . 12

3 Scope of the work 14
3.1 Preliminary design choices . . . 14
3.2 Design and fabrication process limitations . . . 14

4 Models and simulations 16
4.1 Theoretical models for resonant membranes . . . 16
4.1.1 Analytical models for resonant frequencies of prestressed square membranes . . 16
4.1.2 Analytical models for resonant frequencies of circular membranes . . . 17
4.1.3 Sensitivity studies of the analytical models . . . 18
4.2 Modelling the stacks . . . 19
4.3 Results of the models . . . 21
4.4 COMSOL simulations of simple membranes . . . 22
4.4.1 Simulating the stack for membranes with multilayer material . . . 24
4.4.2 Multilayer membranes in vacuum . . . 25
4.4.3 Multiphysic acoustic-shell simulation for damping effect estimation . . . 29
4.5 Comparison of simulation results with analytical models . . . 31

5 Fabrication process **33**
5.1 Mask design for test membranes . . . 33
5.2 In-process metrology techniques . . . 35
5.2.1 Ellipsometry for thickness measurement of transparent layers . . . 35
5.2.2 Curvature-based residual stress measurement in wafer using Stoney formula . . . 36
5.3 Sectional view of the membranes and process sheet . . . 37
5.4 Stack layers fabrication process and stress control . . . 38
5.4.1 Wet thermal oxidation . . . 38
5.4.2 PECVD silicon dioxide layer . . . 40
5.4.3 PECVD silicon nitride layer . . . 40
5.5 Backside aluminium mask . . . 40
5.5.1 Aluminium backside layer . . . 40
5.5.2 Backside lithography with membrane mask . . . 42
5.5.3 Aluminium backside mask realisation . . . 42
5.6 Etching of the membranes . . . 42
5.6.1 Dicing of the wafers . . . 42
5.6.2 Dies preparation for etching . . . 43
5.6.3 Deep RIE of membranes . . . 43
5.6.4 Die release from support wafer . . . 44
5.7 Grinding dies to reduce the impacts of etching non-idealities . . . 44
5.8 Results of the fabrication process . . . 46

6 Measurements methods **50**
6.1 Taken measurements . . . 50
6.1.1 Principles behind white light interferometry for topology scanning . . . 50
6.1.2 Basics of the laser-Doppler vibrometry . . . 51
6.2 Sample preparation . . . 51
6.3 Measurement setups . . . 53
6.3.1 Set-up for topography determination . . . 53
6.3.2 Polytec setup for a vibrometric measurement . . . 53
6.4 Topology of membranes . . . 54
6.4.1 Procedure for topology scanning . . . 54
6.4.2 Post-processing and artefacts . . . 55
6.5 Vibrometric measurement . . . 56
6.5.1 Procedure for measurement taking . . . 56
6.5.2 Settings choices . . . 56
6.6 Set of scans and choice of parameters to analyse . . . 56

7 Results and discussion **58**
7.1 Topographic results analysis . . . 58
7.2 Laser vibrometry results for standard thickness dies . . . 60
7.2.1 Double side polished wafer - Wafer 5 . . . 61
7.2.2 Dies from standard wafers 4 and 6 . . . 62
7.3 Vibrometric exploratory measurement of resonant frequency for membranes on grinded dies . . . 65
7.3.1 Grinded dies from wafer 4 . . . 65
7.3.2 Grinded dies from wafer 6 . . . 69
7.4 Results comparison with analytical models, design parameters and simulation outcomes 69
7.4.1 First mode comparison between analytical models, Comsol simulation and real measurements . . . 71
7.4.2 Higher modes comparison with Comsol simulation . . . 71
7.5 Interesting pathways for further improvements on the present results . . . 74
7.5.1 Model for circular designs . . . 74
7.5.2 Simulation of damped eigenfrequencies . . . 74

7.5.3 Fabrication 74
7.5.4 In process stress metrology 75
7.5.5 Complementary measurements propositions 75
7.6 In context application 76

8 Conclusion **77**

A Appendix A : Alternative process using LPCVD **79**

Bibliography **81**

List of Figures

2.1 Representation from [1] of a high volatge insulation with a gas filled void a) capacitor equivalent of the insulator where PD occurs b) equivalent circuit diagram with spark gap F during PD 4
2.2 Voltage waveforms of the equivalent circuit diagram in Figure 2.1 showing the PD occurance, u_z is the absolute critical value enabling the local breakdown [1] 4
2.3 Four models of configurations of partial discharges and their respective spectrum a) plate-plate, b) needle-plate, c) ball-plate, d) floating model from [9] 8
2.4 Detection sensitivity for a sensor working around resonant frequency (intrinsic frequency) or far below (flat response range) [9] 8
2.5 Membrane building techniques 10
2.6 Illustration of the results of the main etching types 10
2.7 Comparison between a) a standard PZT sensor stack and b) the proposed stress regulated PZT sensor in [29] 13
2.8 Final etched PZT sensor from [29] 13

4.1 Nodal circles and nodal diameters, respectively m and n in Table 4.1 and illustration of mode m=2, n=1 from [33] 18
4.2 Sensitivity of the model 4.4 from [21] to a) the thickness of the membrane, b) the side lenght of the membrane and c) the residual stress in the stack 19
4.3 Sensitivity of the model 4.9 to a) the thickness of the membrane, b) the side lenght of the membrane and c) the residual stress in the stack 19
4.4 Design curves for the silicon nitride layer to obtain the goal stress of 50 MPa with a silicon dioxide layer determined relatively to it for a total thickness of 1 μm of the stack 21
4.5 Selected stack designs based of Figure 4.4 21
4.6 Design space for 1µm-thick square membranes based of model 4.4 22
4.7 Design space for 1µm-thick circular membranes based of model 4.9 22
4.8 Design curves for a) square membranes and b) circular membranes extracted from the design spaces above. The red dots indicate the chosen membrane sizes. 23
4.9 Proposed designs for each type of stack, the membrane cavity is fully open on the backside as the membranes are fully clamped 23
4.10 Model Builder from COMSOL for the implementation of a layered material 24
4.11 Stack composition in Layered Material 25
4.12 Interface definition and position in Layered Material 25
4.13 Stack view of the layered material 25
4.14 Illustration of mode shapes for the six computed eigenfrequencies of a square membrane 26
4.15 Illustration of mode shapes for the six computed eigenfrequencies of a circular membrane 26
4.16 Six first eigenfrequencies for a Type A-stack membrane a) square and b) circular shape 27

4.17 Six first eigenfrequencies for a Type B-stack membrane a) square and b) circular shape 27
4.18 Six first eigenfrequencies for a Type C-stack membrane a) square and b) circular shape 27
4.19 Total kinetic energy frequency response of the 1850μm diameter membrane in vacuum 29
4.20 Geometry for multiphysics acoustic-shell simulation 29
4.21 Model builder of the acoustic-shell multiphysics simulation 30
4.22 Total kinetic energy frequency response of the 1850μm diameter membrane in air . . . 31
4.23 Comparison of the first eigenfrequency between analytical model 4.4 and the results of the Comsol simulation of each stack type 32
4.24 Comparison of the first eigenfrequency between analytical model 4.9 and the results of the Comsol simulation of each stack type 32

5.1 Illustration of the structures 33
5.2 Full mask designed for the process 33
5.3 Dies configuration a) α : 1600 μm of side length and δ : 1200 b) α : 1850 μm of diameter and γ: 1350 c) ϵ : 800 μm of side length and 900 μm of diameter d) ζ : 400 μm of side length and 600 μm of diameter, the value of every parameter indicated in this Figure is given in Table5.1 35
5.4 Example of stack provided to the ellipsometer software 36
5.5 Rapid evaluation of the radius [36] 37
5.6 Fitted polynomial process for the silicon nitride layer on sample WF4 from following process 37
5.7 Cross-sectional schematic view of the step by step process 39
5.8 Quality patterns a) resist and aluminium mask, b) results of the etching of the polished backside, c) results of etching on a rough backside 42
5.9 Dies ready for etching, glued with resist on an aluminium-coated substrate 43
5.10 Pictures taken in SEM showing a) the trench caused by an isotropic etch step, b) results on double polished wafer with 1" isotropic etch steps and c) results on standard wafers with 14" isotropic etch steps 44
5.11 Coating process for a) type A process and b) type B process 47
5.12 400 μm membrane pattern on a grinded die a) general result and diffraction effects and b) imperfections : rounded corners and irregular borders 48
5.13 Comparison between a) before and b) after etching of the aluminium mask in a 950 μm ciruclar pattern on grinded die, c) SEM imaging after RIE etching of a 400μm pattern on grinded die, the imperfections of the aluminum mask are visible in the top layer . . 48
5.14 Broken membrane from wafer 7 a) crack in the film and b) rolling up of the film under the residual stresses in it 48

6.1 Michelson interferometers a) general case [42] and b) Polytec configuration [43] 51
6.2 Illustration of the principle of laser-Doppler vibrometry [45] 51
6.3 Samples on a) metal and b) glass plates 53
6.4 Set up for topology measurements of the membranes 53
6.5 Adjustment of the angle of the goniometer a) before : fringes can not be distinguished, b) after : fringes are well spread 54
6.6 Polytec Set up for vibrometric measurement: here the cable has crocodile ends and is fastened to the edge of the chuck, the metal plate secured to the platform, the piezoelectric disc glued on the plate, the zoom and the laser are adjusted above the sample. 55

7.1 Membrane during topology measurement 58
7.2 Intensity of the reflection corresponding to the membrane from Figure 7.1 59
7.3 Topology results of a 600 µm diameter membrane 59
7.4 Profile line of the curvature measurement of the 400µm square membrane from wafer 4 60
7.5 Profile line of the curvature measurement of the 1350µm circular membrane from wafer 4 60
7.6 Displacement plot of the vibrometric measurement of the 1600µm membrane from wafer 5 61
7.7 1350µm membrane from wafer 5, partially glued 61

7.8 SEM images of the grass piles in membranes of wafer 6 a) 400µm square membrane b) 600µm circular membrane and c) close up 63
7.9 Comparison of the membrane state for grass piles for square membranes of the wafer 4 a) 400µm b) 800µm c)1200µm and d) grass from the backside of a membrane 63
7.14 Irregular membrane film from 800µm square membrane from wafer 4 65
7.10 Spectrums obtained from membranes of the wafer 4 with the identifiable modes indicated 66
7.11 Spectrums obtained from membranes of the wafer 5 with the identifiable modes indicated 67
7.12 Spectrums obtained from membranes of the wafer 6 with the identifiable modes indicated 68
7.13 a) Glued corner of 1600µm membrane from wafer 4 grinded die and b) irregular look of the measurement 69
7.15 41 mode of the 950µm membrane 69
7.16 Spectrums obtained from membranes of grinded dies of the wafer 4 with the identifiable modes indicated 70
7.17 Spectrums obtained from membranes of grinded dies of the wafer 6 with the identifiable modes indicated 70
7.18 Comparison between the model used for design, the FEM simulation results in Comsol and the fabricated membranes for the square designs 72
7.19 Comparison between the model used for design, the FEM simulation results in Comsol and the fabricated membranes for the circular designs 72
7.20 Mode shapes of the 800µm square membrane from wafer 5 a) 11 b) Circ. 10 c) 12 and d) 31 73
7.21 Mode shapes of the 800µm square membrane from wafer 5 a) 00 b) 01 c) 20 and d) 21 73

A.1 Final membrane structure for Type C process 79

List of Tables

2.1 Sensors comparison for PD detection from research (R) and industry (I) 9

4.1 C_{mn} values for the low vibration mode from [18] 18
4.2 C_{mn} values for the low vibration mode from [18] 18
4.3 Material parameters of silicon dioxide from [34] and silicon nitride [35] 20
4.4 Available materials and deposition processes for stack design and expected residual stresses [36] 20
4.5 Design choices for the membranes sizes related to the expected frequencies 23
4.6 Eigenfrequencies values in kHz from Comsol simulation in vacuum depending on the type of stack and the side length of a 1µm thick square membrane 28
4.7 Eigenfrequencies values in kHz from Comsol simulation in vacuum depending on the type of stack and the side length of a 1µm thick circular membrane 28
4.8 Eigenfrequencies of 1850μm diameter membrane in air 31

5.1 Parameters used in the mask design for the different dies 34
5.2 Process sheet 38
5.3 Stack layer thicknesses and residual stress measurements, values with asterix are extrapolated from another wafer of the same process 41
5.4 Bosh process recipe 44
5.5 Grinded dies 45
5.6 Adaptation of the process sheet for grinded dies 45
5.7 Results of the type A process 49
5.8 Results of the type B process 49

6.1 Sets of samples 52

7.1 Topology measurements of membranes from wafer 4 59
7.2 General results for first mode resonant frequency, width measurements marked with * are taken using the Polytec and are thus approximations, the frequency marked ** was measured on a partially glued membrane 64
7.3 Comparison of the higher modes frequencies with Comsol prediction for 800µm square membrane from wafer 5 73
7.4 Comparison of the higher modes frequencies with Comsol prediction for 950µm circular membrane from wafer 5, i : nodal circles j: nodal diameters 73

A.1 Process sheet for Type C stack 80

1 Introduction

This master thesis proposes a design process for ultrathin membranes with control of their resonant frequency. The proposition is to tune residual stresses in the thin film stack composing the membranes to achieve this goal. This approach is part of the large research field for Micro Electro-Mechnical Systems (MEMS) sensors improvement. The design specifications are driven by a chosen application in the field of industrial monitoring.

In the last years, Internet of Things (IoT) applications have boomed and invaded the everyday life. Remote sensors and connected objects can be found everywhere, in all possible domains of applications. Some of these only exist to fulfill the curiosity and desire of consumers to follow the trend but can be deeply irrelevant. On the other hand, IoT nodes and non-invasive monitoring can make a difference in the industrial domain by preventing failures thanks to the detection of the early signs of defects. The high-voltage industry has been focusing for years on the detection of partial discharges that can be related to over 85% of reported failures of equipments.

This text begins with a contextualisation of Partial Discharges (PD) as destructive events that occur in high-voltage equipment when the insulation partially fails and starts to degrade. The signals that these events produce are investigated with a focus on acoustic emission. Acoustic emission detection is interesting as it allows for non-invasive monitoring and, although it is already in use, it is still an unconventional method to detect PD in industry nowadays. The use of low-range ultrasound MEMS microphones currently implies bulky equipments to solve a lack of sensitivity issue. In response to this problem, designing membranes-based sensors with an enhanced sensitivity through the use of resonant modes could be of interest. The basics of the mechanical behavior of a membrane and the precise positioning of its eigenfrequencies are investigated. Residual stresses are found to be a key parameter of eigenfrequencies and some research on common methods to control these is done to complement the State of the Art Chapter.

The Scope of The Work Chapter further defines the exact objectives that are pursued. This work only covers the design and fabrication of resonant membranes, but does not discuss the transduction process. Another specification of this work is to keep the bill of material as simple and embeddable as possible. This directed the choice to exclusively with CMOS-compatible dielectrics. The main goal is set on implementing a stress-controlled multilayered stack.

The following steps all go towards a proof of concept of the use of stress controlled stacks in ultrathin dielectric-only membranes to control their resonant frequency. As detailed in Models and Simulation chapters, theoretical models with all the needed parameters were either found in the literature or proposed for designing both the membranes and the stack compositions. A fast design method based on these theoretical models is implemented using Matlab. The expectations of these designs are then compared to Comsol Multiphysics simulations before fabrication of the effective membranes.

The realisation challenges of the stress-controlled stacks are detailed in Fabrication process Chapter. Once the stack is completed, two main fabrication processes are tested, one on standard thickness wafers, the other on thinned dies. The goal is to determine the impact of several non-idealities, linked to etching membranes in thick dies, on the quality of the resulting devices and to validate the methods to process thinned dies individually.

The samples resulting from both processes are finally measured with a setup based on laser vibrometry and compared to the theoretical expectations in terms of eigenfrequencies. The setups are detailed in Measurement Methods Chapter and the results are presented and discussed in the last chapter.

2 State of The Art

The goal of this first chapter it to provide the necessary background to set the framework of this master thesis. The specifications for the membrane design are driven by an application of industrial equipment monitoring in the domain of the high-voltage electrical network. These equipment can suffer from partial discharges, incomplete insulation breakdowns that deteriorates the insulating material and can cause further damage. Monitoring these events with ultrasound microphones in a non-invasive technique to detect them, although unconventionnal.

The first section discusses the state of the art in the partial discharge detection field, defines the emitted signals and makes a quick inventory of the mainstream ways to detect these. The main goal is to set the context of this work. Partial discharges are a very broad subject and the second section explains why the subject is narrowed down to the use of membrane based ultrasound microphones for acoustic emission detection. In section 2.3, the acoustic emission signal and sensing methods in the case of PD detection are reviewed. The last two sections lay the basics for membranes with a specific focus on their resonant behavior and the residual stress control in multi-layer material stacks respectively.

2.1 Partial discharges

Partial discharges are small dielectric breakdowns that occur inside a defect or lower density region in an insulating material [1]. This can provoke further damage in the material and eventually end in a full short-circuit of the insulation. Partial discharges need high voltage to occur and is thus mostly seen in grid equipment such as transformers, lines or any other power electronics equipment.

The first part of this section focuses on defining the partial discharge phenomenon and the associated signals that are emitted. Second part summarises the type of sensors that are used in industry or in research to detect them nowadays.

2.1.1 Description of the phenomenon

According to the IEC standards, partial discharges are "localised electrical discharge that only partially bridges the insulation between conductors and which can or can not occur adjacent to a conductor" [2]. These discharges are also named incomplete breakdowns as they do not impact the insulation strength in the beginning [1].

Higher local electric field stress concentrations generally means a specific part of the insulation will be more prone to PD. These zones can be of several aspects : (i) a cavity, either a defect or a small crack, in a solid dielectric, (ii) a sharp edge, either in void or any other gaseous insulator, or (iii) a region showing a lower density in a liquid insulator. Physically, PD can take place in any insulation at any

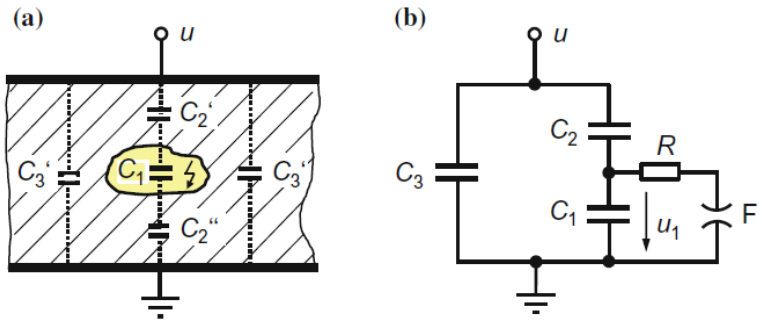

Figure 2.1: *Representation from [1] of a high volatge insulation with a gas filled void a) capacitor equivalent of the insulator where PD occurs b) equivalent circuit diagram with spark gap F during PD*

voltage. However, there is almost no need to test for them at low voltages since they would not be among the main causes of failure. Partial discharges are typically a high-voltage equipment problem. The typical voltage to start testing for partial discharges in the industry lies between 2.5kV and 3.3KV [3].

The conditions for a partial discharge to occur are an electric field reaching the local critical value for impact ionisation and the presence of a free electron inside the cavity, void or low density region [1, 2, 4]. This electron can then trigger an electron avalanche inside the defect. The behavior of an insulator where a PD occurs can be approximated by an equivalent circuit of capacitors such as presented in Figure 2.1. The smaller permittivity of the enclosed gas increases locally the electric field strengh above the critical value for impact ionization. When the PD triggers, a current flows through the dielectric and shares the accumulated charges between the two capacitors representing the insulation.

The way a partial discharge prepares and occurs can then be approximated with the following development : in the preparation step, the capacitors C_1 and C_2 get charged proportionally to the voltage at their terminals, following expression $u_1(t)$ in Equation 2.1. Next, the PD occurs and as current flows, the voltage across C_1 brutally discharges to reach a small residual voltage. These two steps are repeated with C_1 charging, PD firing and C_1 discharging as long as vol tage $u_{10}(t)$ stays above the critical value. The waveforms are visible in Figure 2.2 [1].

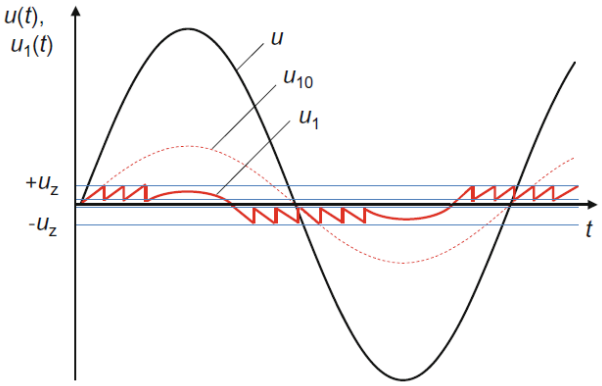

Figure 2.2: *Voltage waveforms of the equivalent circuit diagram in Figure 2.1 showing the PD occurance, u_z is the absolute critical value enabling the local breakdown [1]*

$$u_1(t) = u_{10}(t) = \frac{C_1}{C_1 + C_2} u(t) \qquad (2.1)$$

PD can be classified in several types depending on the configuration of the equipment, its insulation and its surroundings. These types are :

- internal discharges : found in solid insultation, in defects such as voids, cavities or small cracks in dielectric materials. They are the most rare and difficult to sense as they usually can not be accessed for direct measurement. Most of the time, they show slow propagation and slow failure mode. However, they are among the most hazardous for the equipment as they can remain unoticed until complete breakdown of the insulation. [1, 3, 4]
- treeing : consisting of discharge impacts in solid insulation that progressively form tree-like discharge channels through the material. These occur continuously.
- surface discharges : PD occuring across insulation surface. These are very common and the

easiest to both spot and fix. [1, 3, 4]

- corona : specific name of PD firing only in gaseous media with no immediate proximity of any liquid or solid insulation. These PD typically emit chemical markors and can be seen visually. However, most of them are not very hazardous. [1, 3, 4, 2]
- contact discharge on floating metal objects in high field conditions : when a metallic object triggers a PD by changing the topology of the normal insulation. [1, 3, 4, 2]

2.1.2 Consequences

Inside the insulation, the potential consequences of partial discharges are multiple, especially for the internal discharges. At first, no change occurs in the insulation strength of the material but, on the long run, exposure to this phenomenom can progressively deteriorate the material. PD generates heat and chemical changes around its region of occurrence. It can also promote the propagation of small cracks. All of these, together with other deterioration mechanisms, reduce slowly the insulation strength and erode the material, causing treeing. The issue of it can be a total breakdown of the insulation leading to short-circuits or even destruction of a piece of equipment. [1, 2, 3, 4, 5]

Such incidents occurring on the electrical network can generate large power outages and be the cause of the destruction of other pieces of equipment. According to the industry, over 85% of asset failures can be related to partial discharges [5]. Moreover, if a full breakdown of an insulation occurs, workers or civilians could be harmed by the discharge. Detecting the partial discharges and monitoring them enables to prevent such incidents and accidents.

2.1.3 Emitted signals and detection of partial discharges

When PD occur, they result in various signal that can be sensed. Some of these are linked directly to the PD itself, others are direct consequences of it. They are summarized in this list [2, 1]:

- electrical signal variations on the conductor of the equipment,
- electromagnetic wave resulting from the variation of the electrical field in the material, that can be sensed in the RF region or in the visible light spectrum,
- temperature variation due to dissipation of energy,
- chemical marks linked to reactions involving the insulating material, including potential burning or evaporation,
- acoustic signal emitted by the stress wave that propagate in the insulator and then in air, this acoustic signal is called Acoustic Emission (AE).

.
Depending on the type of PD, these signals can be more or less easy to sense. The most challenging type of PD to detect is the internal one because of the difficult access to these signals for measurements. Most of the time, they can be detected through electric signal variations at their terminals, RF sensing or AE measurements. Specific computer assisted methods are deployed to both detect the PD and find the source and new ones are being developed. [1]

The PD signal itself is characterized by the time it takes to charge the capacitor to the critical value and then to discharge it and is most of the time shaped as a narrow current pulse, close to a Dirac pulse. They can be approximated by the superposition of two exponential functions. Most PD show rising and falling time of some microseconds, which places them under the MHz range, but the external ones can have frequencies as high as the GHz range. More continuous PD also exist in gases and are

called pulseless PD [1].

The PD are commonly measured as a an equivalent charge corresponding to the integration of the current pulse. Most of the time, this pulse charge value is expressed in pC and is invariant from discharge to discharge. Typical values range from below $1pC$ up to more than $1000pC$. Since most PD are not easily accessed for direct measurement, a method called apparent charge test can be used to retrieve the charge value. [1, 4] This apparent charge is defined as "that charge which, if injected within a very short time between the terminals of the test object in a specified test circuit, would give the same reading on the measuring instrument as the PD current pulse itself"[2].

The emitted signal depends on the power in the line or equipment, the value of the capacitance of the defect resulting in the PD and the value of the critical voltage for the defect material. Most of time the energy of the discharge is proportionnal to the charge squared and all other emitted signals are proportional to the energy of the discharge. [6] As an indication of the order of magnitudes that can be encountered, currents above 1.3A can be observed in 20kV equipments with discharges having a rise time of 50ps and transferred charge of 114pC [7].

In order to have correct measurement, calibration of the sensors and signal processing chain is needed because instruments and situations for PD testing vary. [1]

2.2 Context of this work

This section describes the scope of the present work in the context of PD detection. It details the choices made to limit the subject of this master thesis around a precise type of sensing and specific parameters to focus on during the rest of the work.

PD detection is a very broad subject, given the numerous signals that are emitted for each discharge. In this context AE detection, seems to be interesting as it is among the non-invasive techniques. It consists in monitoring the ultrasonic acoustic emissions that result from the PD using microphones. Moreover industry already uses AE sensing for PD detection but it is still considered a non-conventionnal method [4]. It can detect PD of the external type, directly occuring in air or the acoustic wave emitted in solid materials and then propagated in air.

The choice is hence to focus especially on AE detection using membranes as acoustic waves are linked to a pressure variation. Making the membranes complementary metal-oxide-semiconductor (CMOS) compatible could be of interest for integration of the sensor and the data processing circuit on the same chip. The following sections will explore the context and state of the art around these two aspects.

2.3 PD detection using AE sensing

The acoustic emission signal has been chosen as it is already used in the industry, however, most of these sensors seem to not be CMOS compatible. Most of the articles report needs for very high sensitivity as the signal often shows very small amplitude. [6]

First part of this section explores the signal characteristics of the AE signals and especially the frequencies of it. Second part reviews some sensors that can be found in recent research articles on PD detection using AE sensing or in the industry.

2.3.1 AE signal characteristics

The main characteristics of a signal are its frequency and its intensity. In this case, the signal is acoustic. This section reviews the frequency content of the signal first before focusing on the question

of the intensity.

The frequency characteristics of a PD signal depend on various parameters including the equivalent capacitor value of the PD-prone region, the frequency of the signal on the conductors in the equipment and the attenuation of the signal in the different material that it crosses. Initial signal often is a very short pulse with very broad spectrum around several megahertz. This spectrum is then impacted strongly along its propagation. Acoustic resonance in the cavity can already generate signal with several resonant peaks. Three main phenomenons can be identified as impacting the frequency content of the signal [6]:

- Frequency-dependent velocity, linked to dispersion : It causes a variation of the arriving time of the different frequency components to the sensor.
- Frequency-dependent propagation paths : The different paths cause different wave components to hit the sensor with relative time lags.
- Absorption in the different materials on path : This phenomenon impacts more the higher frequency components.

The changes in signal that it causes can be summarised as a smoothing of the signal depending on the propagation distance : the signal risetime becomes slower and the pulse duration is spread. The multiple reflections, wave-types and velocity variations also can cause echoes of the wave. [6, 8]

To approximate the available signals, four typical configurations were reproduced in testbenches in [9]: plate-plate, needle-plate, ball-plate and floating model. These are illustrated in Figure 2.3 along with the respective spectrum sensed by a lead-zirconium-titanate (PZT) piezoelectric sensor for each configuration. They give a frequency range for the largest amplitude signal part between 50 to 170 kHz. This corresponds to the low ultrasonic spectrum.

The intensity of the sensed signal is directly linked to the amplitude of the received sound wave. At the source of the PD, the amplitude of the acoustic wave is proportional to the energy of the discharge. This is already very variable from discharge to discharge. Various factors can cause attenuation on the signal amplitude : geometrical spreading and division of the wave among different propagation paths, transmission losses at each interface from medium to medium and different absorption in each medium. [6, 8] At the sensor itself, other parameters like incidence angle can further impact the sensed signal. [6]

2.3.2 Current sensors for PD detection trough AE sensing

This section shows a small selection of sensors that where either recently developped in resarch or that are currently sold in the industry for PD detection using AE sensing. They are presented in Table 2.1.

It can be seen in this table that the informations about sensitivity are not normalised. This is due to the impossiblity to quantifiy the equivalent charge that would be measured as the signal varies strongly from equipment piece to another.

These sensors are most of the time either glued on the equipments [11], which is a more invasive operation, or used as portative devices with bulky waveguides. [6, 14] The main problem is always the attenuation of the signal amplitude that can become to small to be detected. The only solutions are either to reduce the distance the wave must cross to meet the sensor, concentrate dispersed wave or increase the sensitivity of the sensor. Combining these solutions is often necessary.

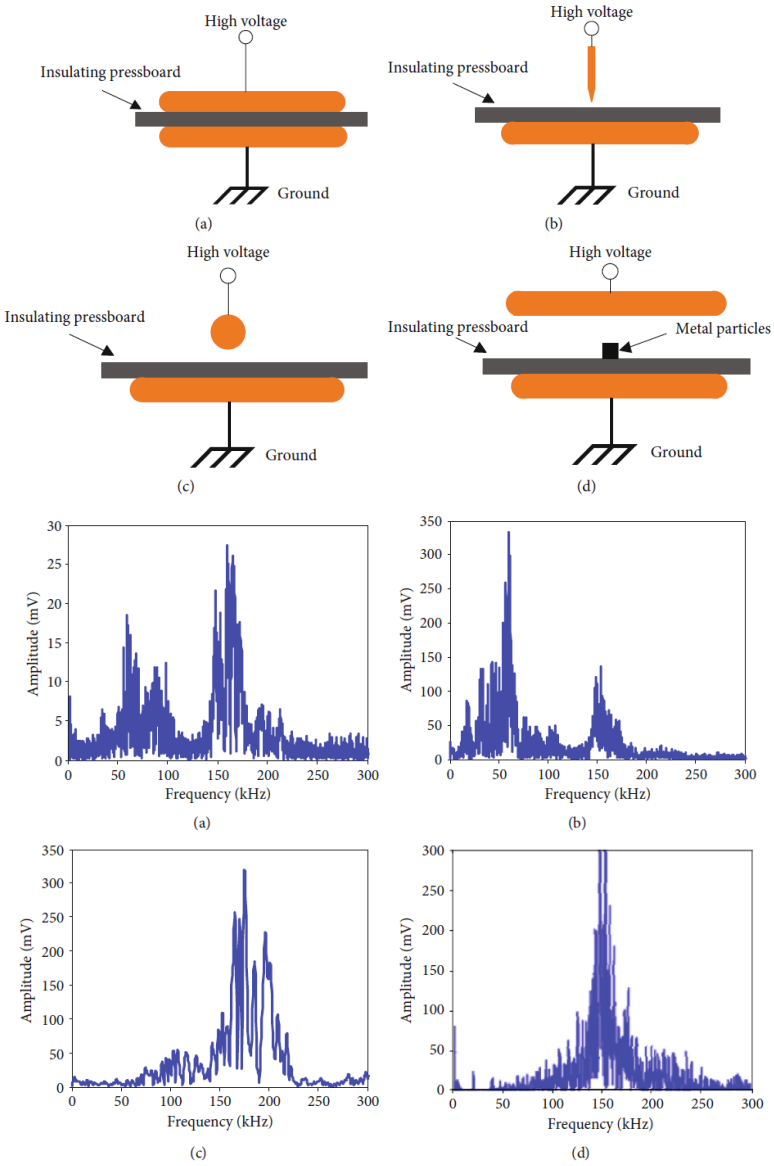

Figure 2.3: *Four models of configurations of partial discharges and their respective spectrum a) plate-plate, b) needle-plate, c) ball-plate, d) floating model from [9]*

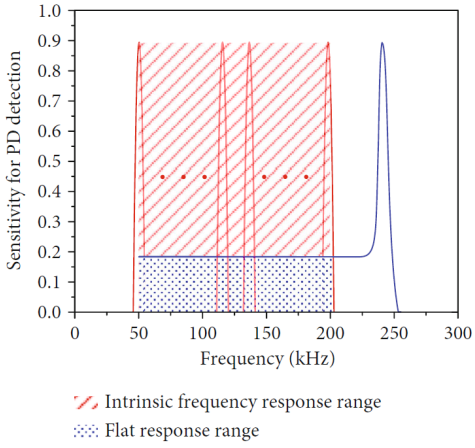

Figure 2.4: *Detection sensitivity for a sensor working around resonant frequency (intrinsic frequency) or far below (flat response range) [9]*

One of the solutions to improve the sensitivity of a membrane-based sensor is to work at resonant frequency. This is proposed in [6, 9]. Figure 2.4 illustrates the advantages of working at resonant frequency in terms of higher sensitivity but also the associated inconvenience of having a much narrower bandwidth.[6, 9] The Figure also illustrates the idea of selecting several membranes with different resonant frequencies to use them together to cover a larger bandwidth like an acoustic filter bank.

Sensor type (R or I)	Membrane Form, Size, Thickness	Resonant Freq. [kHz]	Freq. Range [kHz]	Sensitivity	Res.	Dyn. Range	Temp. Range °C
FP interferometer (R) [10]	Circ. 2mm ⌀ 25µm thick.	91	Up to 100	552Pa/fringe	2,8 Pa	N/A	N/A
FP interferometer (R) [9]	Circ. 1.5 to 1.8 mm ⌀ 40 µm thick.	195,3 to 169.7 (resp.)	Up to 200	0,1nm/Pa to 1,4nm/Pa	N/A	N/A	N/A
PZT (R) [9]	N/A	150	50 to 180	-80 to -70 dB	N/A	N/A	N/A
PZT (PAC WD AH17) (I) [11]	N/A	125 450	125 to 1000	-56dB (ref V/m/s) -61dB (ref V/µbar)	N/A	N/A	-65 to 177
Piezores. Kulite (I) [12]	N/A	125	N/A	-127dB (ref V/µbar)	4,47 µV/Pa 35.5kPa	1.12Pa to	-55 to 260
Ultraprobe 9000 PZT (I) [13]	N/A	20 to 100 Tunable	N/A	Detects 0.127 mm ⌀ leak @0.34 bar @ distance of 15.24 m	N/A	N/A	0 to 50

Table 2.1: *Sensors comparison for PD detection from research (R) and industry (I)*

2.4 Membranes and resonant behavior

Membranes are often used in the sensors proposed in Section 2.3.2 above. Working on the membrane transduction enhancement, from a mechanical wave to stress variation, can increase the sensitivity of any sensor using this mechanical structure. This section reviews the membranes by begining with generalities about it, including a contextual definition, the main fabrication techniques to create MEMS membranes, the basics of their static behavior and how their are usually exploited in MEMS sensors. A second subsection covers the resonant behavior of membranes and the existing theoretical models for this behavior.

2.4.1 Defining membranes in theory and MEMS fabrication contexts

This section begins with a definition of the term membrane depending on the different contexts that will be along the theoretical design process and the fabrication steps. Two definition of theoretical objects a physical membrane can be identified to are first stated. Next, a definition of a physical membrane in the context of MEMS is proposed before covering the basics of the fabrication.
Theoretically, according to [15], a membrane is a thin structure with two dimensions largely superior to the third. It is an idealised and simplified object. This structure can be assimilated to a surface in space and its bending rigidity is considered to be so low it can be neglected. It sustains only tensile loads through in-planne stresses. The main parameters that define it are its mass per unit of surface area and the tension applied to it per unit of length of its boundary.

Another theoretical object that is very close to the membrane is the plate : here as well, two dimensions are largely superior to the third. It is composed of linear elastic material and considered to be of uniform thickness. The main difference is that a plate has a rigidity in bending and deforms primarly in flexion along the axis perpendicular to the plane of the plate. These deformations must remain

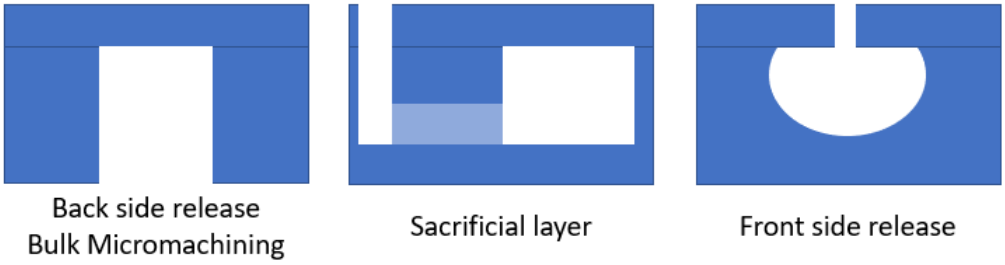

Figure 2.5: *Membrane building techniques*

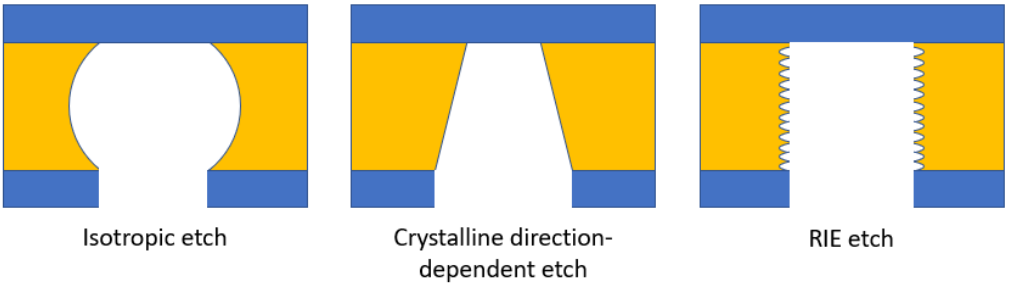

Figure 2.6: *Illustration of the results of the main etching types*

small in comparison to the thickness of the plate.[15]

Comparing these two definition to each other, on one hand the model of the membrane is close to a soap bubble or a piece of soft fabric stretched on an embroidery hoop and on the other hand the plate resembles a piece of Bristol paper.

In the context of MEMS fabrication, a membrane is a thin layer of material with two dimensions of the same order of magnitude and a third dimension, the thickness, which is of a smaller order of magnitude. It is a released structure, meaning there is no layer underneath that supports it and it is maintained in place from its sides. The clamped part of its edges is not always continuous. In certain case, a membrane can also be called a diaphragm. [16]

The realisation of MEMS membranes can be achieved through several processes. Some of the most used are detailled in this paragraph but further information can be found in [17]. The most common way to build a MEMS membranes uses are :

- Bulk micromachining : The principle is to stack the layers of materials that will compose the membrane one above another. These layers can include designs for other functional parts of the membrane such a resistors, wires or electrodes. Once these layers are in place, the membrane is released from the backside using an etching technique. The etching can be performed using gas, plasma, liquid etchant or a reactive ion etching (RIE) process that alternates between plasma etching and plasma deposition of a material.

- Front side release : This technique relies on the etching of material under the membrane layers by an isotropic etchant. It implies that the membrane either presents a gap or is not fully clamped.

- Use of a sacrificial layer : In this case, the membrane layers are build on top of another layer that is made to be etched from an opening that can be further away from the membrane than in the case of front side release. Here as well the technique relies on an isotropic etchant.

These three membrane building techniques are illustrated in Figure 2.5 and the etching types in Figure 2.6.

2.4.2 Basic of static mechanical behavior of membranes and their use in transduction

The basics of the mechanical behavior of a fully clamped membrane can be found in [18] and [16]. If a pressure is applied to a membrane, it causes the membrane to deflect in a predictible way :

$$\frac{Eh^3}{12(1-\nu^2)}\left(\frac{\partial^2}{\partial x^2}+\frac{\partial^2}{\partial y^2}\right)\left(\frac{\partial^2}{\partial x^2}+\frac{\partial^2}{\partial y^2}\right)w(x,y)=p \tag{2.2}$$

where

- $\frac{Eh^3}{12(1-\nu^2)}$ is the flexural rigidity of the material,
- $w(x,y)$ is the steady displacement caused by the pressure p applied

The deflection of a square membrane of side $2a$ can thus be found as :

$$w(x,y)=\frac{pa^4}{47}\frac{Eh^3}{12(1-\nu^2)}\left(1-\frac{x^2}{a^2}\right)^2\left(1-\frac{y^2}{a^2}\right)^2 \tag{2.3}$$

And the stress at the surface of it :

$$T_{XX}=-0.51\frac{pa^2}{h^2}\left[\left(1-\frac{y^2}{a^2}\right)^2\left(1-\frac{3x^2}{a^2}\right)+\nu\left(1-\frac{x^2}{a^2}\right)^2\left(1-\frac{3y^2}{a^2}\right)^2\right] \tag{2.4}$$

A symmetric expression can be found for T_{YY}.
The maximal deflection is found at the centre of the membrane and the maximal stress can be found at the center of its sides. This can easily be adapted to a circular membrane : the maximal deflection is also at the center of it and the maximal stresses can be found all along the border, at the surface of the membrane.

This position of maximal deflection makes the circular membranes especially suitable for transduction that relies on the transformation of displacement to an electrical signal as the displacement at their centre will be larger. Such transductors can be capacitive or use interferometry. This is found in Fabri-Perot interferometers [9]. On the other hand, the repartition of stresses makes membranes square good candidates for application where the transduction transforms stresses in an electrical signal like piezoresistors or piezoelectric sensors.

As seen above in equation 2.3, the typical quantity to sense with a membrane is the pressure applied on it. It is thus often used in application such as microphones for sound or ultrasounds, pressure sensors for gas in chambers, etc. In such sensors, one of the main parameters for a good mechanical Figure of Merit (FOM) is the thickness of the membrane. The mechanical FOM actually depends on the ratio between the area and the square of the thickness for typical piezoresistive pressure sensors [19].

2.4.3 Resonant behavior of membranes

When in resonance, mechanical structures present higher deformation at higher speed than at other nearby frequencies. The type of displacement depends on the mechanical wavelength provoking this deformation.

The deformation type is called the mode shape associated to a resonant frequency or eigenfrequency of the structure. In the case of membrane, the mode shapes depend on the form of the membrane : for a square membrane, the mode shapes follow sinusoidal functions across the membrane whereas for circular ones, it follows Bessel functions. [20] Computing the frequencies associated with each mode can be done by solving the differential equation for the position of the nodes of the mode. However, this method is long and fastidious so a more straightforward model is of highest interest.

The resonant behavior of membranes depends on various parameters : size of the membrane, thickness, modes, material, residual stresses inside the membrane, type of clamping etc. Several theoretical models exist to compute the eigenfrequencies of a membrane taking some of these parameters in account. Most of them consider either a membrane that has no specified thickness or a plate that has no tensile residual stress. [21, 18, 15, 20] The ones that were chosen for this master thesis are discussed in the next chapter. Selection was made based on the presence of the maximum design parameters present in model. The chosen parameters to work with are the thickness and the area of the membrane [19] and residual stresses.

With every other parameter fixed, controlling the stress in a membrane is key to controlling its resonant frequency. It also impacts its position at rest. The film composing the membrane can be in buckling if the residual stress in it is compressive. [22] Occurrences of such a control of the residual stresses inside a stack in a membrane or other released designs such as cantilevers can be found in literature. The materials used vary strongly and most of these stacks are fairly thick and complex (many layers). These are investigated in the next section.

2.4.4 Stress control in material stacks for membranes

Controlling the stress inside a stack in order to control different parameters among which the resonant frequency of the fabricated structure has been done previously. This section summarizes the attempts that were found the be the closest to the ongoing project.

The residual stress in a material comes from difference in thermal expansion coefficient between the different materials deposited one on top of another in a stack. [23] This thermal expansion coefficient is a material parameter. It can vary with the quality of the deposited material, its crystalline structure, its density, etc.[24] The deposition technique has strong impact on it but it can also be modified after deposition by thermal treatments. [25]

To measure the stress in deposited thin films, several methods exists. Some imply to measure the annealing temperature of the layer but such techniques completely change the stress in the material to retrieve its previous value. [25] Among the non invasive techniques that preserve the sample, articles mention the use of the Stoney formula coupled to a curvature measurement of the sample. These measurements must be taken after each manipulation to know the stress in the thin film of interest.[26, 27, 28]

The stress in stacks of multiple thin films can be controlled in several ways : the material themselves can be chosen specifically for their stress level after a specific deposition technique corresponding to the wanted stress, altered in term of residual stress through thermal treatments or stacked one above another to compensate the stresses of one layer with another. Since finding materials with the wanted stress level is not always possible and thermal treatments only give a partial solution to the problem, stacking is the most common solution. [29]

Various goals can be achieved through stress regulation. It can be used to ensure that cantilevers will not stick to the substrate once released or avoid that it rolls over itself [30], to ensure membranes are not buckling [22, 31, 19] or control their resonant frequencies [29] and behaviour in deflection [32]. Several stress regulating stacks can be found in articles.

Most of the stacks use either silicon dioxide (SiO_2) for a more compressive layer or silicon nitride (Si_3N_4) to increase tension. These two materials can be thermally treated to change their stress. Undoped SiO_2 is typically deposited with a compressive stress, often around 300 MPa, weither the deposition technique is plasma-enhanced chemical vapor deposition (PECVD) or a thermal oxidation. [26] It can be thermally treated using thermal cycling to reduce the residual stress. [25] For Si_3N_4, the residual stress is typically tensile and thermal cycling can be used to increase it. It can reach around

1 GPa. Specific deposition technique enable to make SiNx layers with controlled stresses between -300 MPa compressive and 300 MPa tensile. [26]

The article that proposes the closest project to the subject proposes a stress regulated stack for membranes used in PZT sensors. Square membranes with thicknesses between 25 and 225 μm for a side length of 1 to 4 cm. These membranes present natural frequencies (first mode), between 506 and 33 283 Hz. The layers used for residual stress regulation are a thermal silicon dioxide layer of 300nm and a low pressure chemical vapor deposition (LPCVD) silicon nitride layer of 100nm. The comparison between a standard PZT stack and the stress regulated proposed stack are displayed in Figure 2.7. To make the membranes, the etching was done from the backside and stopped at the right thickness in the silicon layer silicon. [29]

These membranes and other proposed released structures, in general, are very large and relatively thick, which makes them bulky but sturdy. However such large membranes can be difficult to embed in a portative apparatus and can not be embedded in CMOS circuits.

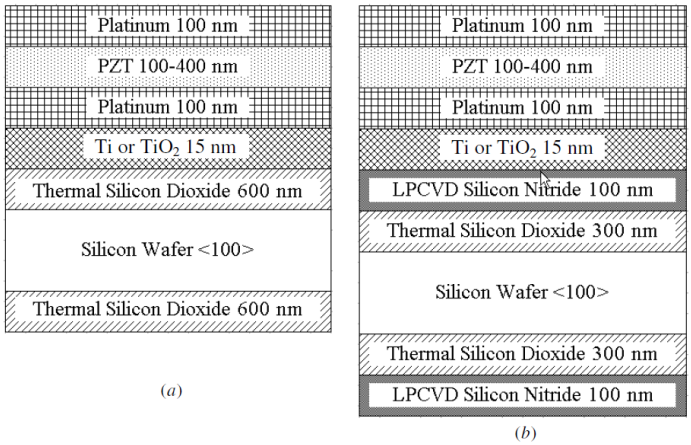

Figure 2.7: *Comparison between a) a standard PZT sensor stack and b) the proposed stress regulated PZT sensor in [29]*

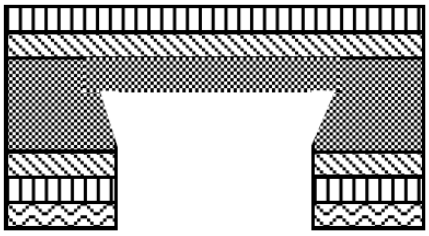

Figure 2.8: *Final etched PZT sensor from [29]*

3 Scope of the work

This goal of this chapter is to define the scope and objectives of the next chapters inside the context defined in the preceding Chapter 2. Preliminary design choices are exposed and the limitations of the design and process are then explained.

3.1 Preliminary design choices

As seen in the State of the Art, sensitivity is a key parameter to improve the detection of PD and membranes show higher displacement either at very low frequencies or in resonance. This master thesis investigates the possibility to use membranes in resonance to increase the sensitivity of ultrasound microphones.

The proposed sensing membranes would be a set of acoustic filters consisting of membranes smaller than 2mm of side, each with a resonant frequency in the 70kHz-170kHz range. This will require membranes to be both thin and present a low residual stress stack.

Membrane shapes will be reduced to squares and circles. These are the most usual shapes and the most efficient when it comes to transduction : square membranes maximise the stress concentrated areas on the membrane sides and circular shaped ones favours larger deformation and displacement.

The first design choices aim to reduce the complixity of the stack and to use CMOS compatible materials. The chosen materials will be SiO_2 and Si_3N_4. These two materials can be deposited using different methods to control their residual stress and can also be thermally treated for stress reduction or increase. SiO_2 and Si_3N_4 are among the most common CMOS compatible dielectric and have been used previously for stress control as presented in the State of the Art section 2. Moreover they are both easily accessible in the Winfab laboratories where the experimental part of this master thesis is performed.

3.2 Design and fabrication process limitations

During this project, only the membrane set is developed. No transduction will be added on it at this stage of the work. This master thesis will focus on the numerous mechanical parameters that can play a role in the determination of the eigenfrequencies of a membrane. To this end, the membranes are first modelled to enable design choices to be made and then simulated to confirm the model before fabrication. The models and simulations are then compared and adapted to the values obtained for each parameter during the fabrication.

In terms of fabrication, the process to produce ultra-thin low-stress membranes with very simple stack designs will be investigated. Several process variations will be compared to one another. The impact

of substrate thickness on the quality of the obtained samples will be considered.

No test set-up for partial discharge is available at the UCLouvain. Building such a set-up required to much time for a master thesis, especially along with the membrane fabrication. The measurements of the resonant frequency of the membranes is hence performed using a laser vibrometry measurement set-up.

4 Models and simulations

This section describes the simulations that have been performed in order to verify the chosen theoretical model and predict the behaviour of the membranes once fabricated. First, the chosen theoretical models and their sensitivity to different parameters are presented. These models are used for design choices regarding the membrane sizes and the stack design. Next, the implementation of the simulations that have been performed in this work is detailed. The simulations have been adapted to the design choices, for the stacks and the membrane sizes. Two types of simulations were used, a simple simulation of the membrane in vacuum and a multiphysics acoustic-shell simulation to investigate the response of the membrane in the air.

4.1 Theoretical models for resonant membranes

The theoretical models used here were chosen for their simplicity and easy implementation in Matlab in order to perform rapid sensitivity studies to different parameters and make design decisions. The main goal is to have models taking the residual stress into account since it can be be used to tune the resonant frequency of a membrane or another structure.

4.1.1 Analytical models for resonant frequencies of prestressed square membranes

A theoretical model for membranes presenting residual stresses is developed in [21] for square or rectangular shapes. The membranes presenting residual stresses will also be called prestressed as they present a non-zero stress at rest. The model is developed for fully clamped membranes. This means that all the edges of the membrane are attached to the surrounding substrate and that the border is thus considered as totally fixed.

This model states that the frequency is given in function of the thickness of the membrane, its side lengths and its material parameters as :

$$f = \frac{\pi h}{4}\sqrt{\frac{E}{3\rho(1-\nu^2)}}\sqrt{\left(\frac{G_{n_i}}{a}\right)^4 + \left(\frac{G_{n_j}}{b}\right)^4 + \frac{2J_{n_i}J_{n_j}}{(ab)^2}} \tag{4.1}$$

where:

- h is the thickness of the membrane [m],
- E is the Young modulus of the membrane material [Pa],
- ρ is the density of the material [kg/m^3],
- ν is the Poisson coefficient [-],
- a and b are the side lengths of the membrane [m],

- n_i and n_j are the modes of each of the side of the membrane respectively [-].

and

$$G_n = \begin{cases} 1,506 & \text{if } n = 1 \\ n_j + 1 & \text{if } n > 1 \end{cases} \tag{4.2}$$

$$J_n = \begin{cases} 1,248 & \text{if } n = 1 \\ G_n^2 \left(1 - \frac{2}{\pi G_n}\right) & \text{if } n > 1 \\ n^2 & \text{if } n > 10 \end{cases} \tag{4.3}$$

At this point, no stress is taken into account yet. Stress impact on the resonant frequency gives the following model, where f_σ is the frequency of the prestressed membrane, still from [21] where σ is the residual stress in the membrane in Pascals [Pa] :

$$f_\sigma = \sqrt{f^2 + \frac{\sigma}{4\rho}\left(\frac{J_{n_i}}{a^2} + \frac{J_{n_j}}{b^2}\right)} \tag{4.4}$$

In this master thesis, the rectangular membranes considered will be square. The used model is hence a simplification of the first proposed model 4.4 :

$$f_\sigma = \sqrt{f^2 + \frac{\sigma}{4\rho a^2}(J_{n_i} + J_{n_j})} \tag{4.5}$$

$$f = \frac{\pi h}{4a^2}\sqrt{\frac{E}{3\rho(1-\nu^2)}}\sqrt{G_{n_i} + G_{n_j} + 2J_{n_i}J_{n_j}} \tag{4.6}$$

The frequency taking the stress in account f_σ is thus directly proportional the inverse of the surface $\frac{1}{a^2}$ and to the thickness h as long as it is thick enough so that its contribution is not overpowered by the stress dependent component. For other terms, the frequency f_s is proportional to their square root : the material rigidity $\sqrt{\frac{E}{3(1-\nu^2)}}$, the stress σ and the inverse of the density of the material $\frac{1}{\rho}$.

4.1.2 Analytical models for resonant frequencies of circular membranes

Various models are available for the circular membranes but none of the found models took in account the thickness and the residual stress at the same time. These models are first listed and compared before laying down some hypothesis and proposing the used model in this master thesis.

First model 4.7 is given in [18]. It is close to the model used in previous section for square membranes. However, it does not account for the impact of residual stresses on the eigenfrequencies :

$$f_{mn} = \frac{C_{mn}h}{2\pi d^2}\sqrt{\frac{E}{12\rho(1-\nu^2)}} \tag{4.7}$$

where non preveiously mentionned parameters are:

- C_{mn} are constants depending on the number m of nodal circles and n of nodal diameters,
- d is the diameter of the membrane [m]

The C_{mn} constants are given in Table 4.1 and nodal circles and diameters are illustrated in Figure 4.1.

Nodal diameters Nodal circles	n=0	n=1	n=2
m=0	40.8	84.9	139.4
m=1	159.1	–	–
m=2	355.6	–	–

Table 4.1: *C_{mn} values for the low vibration mode from [18]*

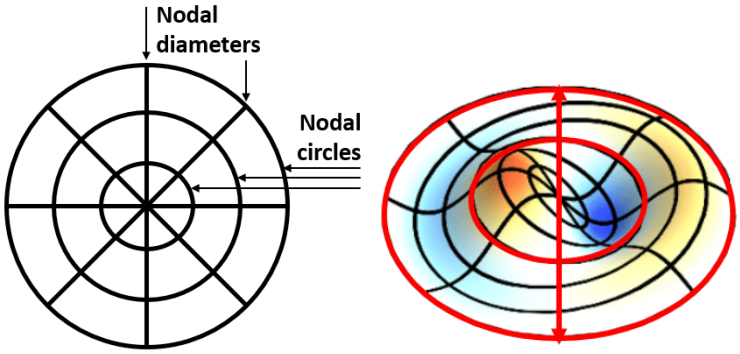

Figure 4.1: *Nodal circles and nodal diameters, respectively m and n in Table 4.1 and illustration of mode m=2, n=1 from [33]*

The second model 4.8 from [15] does include the effect of the stress but is neglecting the impact of the thickness. The model is detailed here below :

$$f_{ij} = \frac{\lambda_{ij}}{2}\left(\frac{S}{\gamma_A}\right)^2 \tag{4.8}$$

with the non previously mentionned parameters :

- λ_{ij} are mode-dependent constants given in Table4.2
- S is the stress in the membrane
- γ_A is the mass of material per unit of area of the membrane

Nodal diameters Nodal circles	i=0	i=1	i=2	i=3
j=0	–	–	5.253	12.23
j=1	9.084	20.52	35.25	52.91
j=2	38.55	59.86	83.9	111.3
j=3	87.8	119.0	154.0	192.1

Table 4.2: *C_{mn} values for the low vibration mode from [18]*

Using the model proposed for the square membranes as an example, we propose an approximate analytical model for circular prestressed membranes. It takes in account the same parameters as the model 4.4 or their equivalent for a circular shape. It is built using a similar form and only account for modes with zero nodal diameters. The proposed expression for the estimation of the eigenfrequencies in the circular shape case is :

$$f_{mn,\sigma} = \sqrt{f_{mn}^2 + \frac{\sigma}{4\rho}\frac{n+1}{d^2}} \tag{4.9}$$

4.1.3 Sensitivity studies of the analytical models

The sensitivity of the proposed models is then investigated to propose a reasonable design space for all parameters playing in the design of soon-to-be fabricated membranes. The main parameters conditioning the resonant frequencies of membranes beside material parameters are the thickness of the membrane, its side length, or diameter, and its stress.

The model 4.4 allowed to produce curves of sensitivity of a square membrane. An illustration of these curves can be seen in Figure 4.2.

In Figure 4.2 a, the frequency is increasing linearly with the thickness if the stress is not included in it. It is also the case for thick stressed membranes. However, in very thin membranes, the stress is taking over. This occurs even if its value is relatively low, such as 50 MPa here.

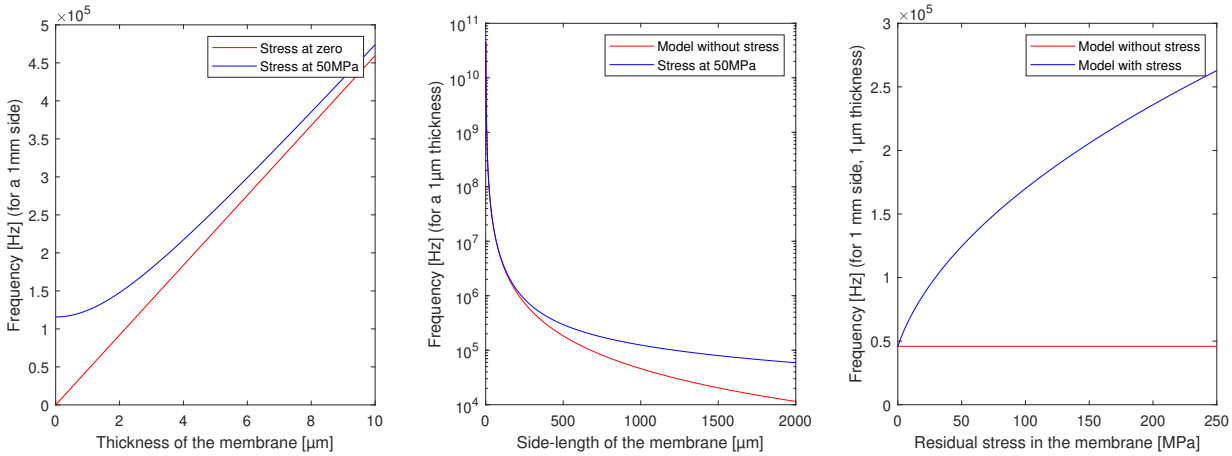

Figure 4.2: *Sensitivity of the model 4.4 from [21] to a) the thickness of the membrane, b) the side lenght of the membrane and c) the residual stress in the stack*

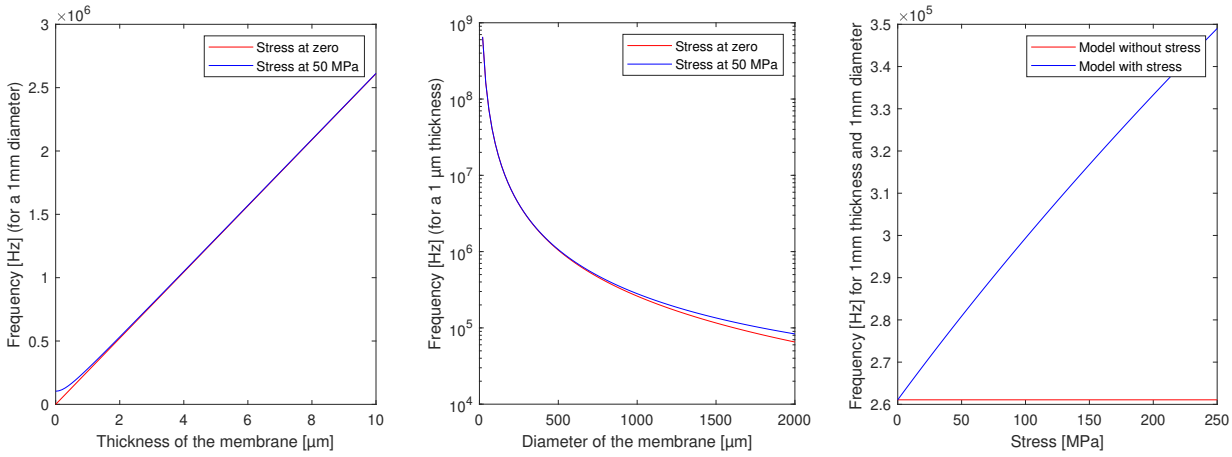

Figure 4.3: *Sensitivity of the model 4.9 to a) the thickness of the membrane, b) the side lenght of the membrane and c) the residual stress in the stack*

The Figure 4.2 b shows the sensitivity of the model to the side length of the membrane. It decreases quadratically with the side if no stress is taken into account. However, stress reduces this effect.

Last frame, Figure 4.2 c shows the impact of the stress on a membrane with a 1 μm thickness and a 1mm side length. The increase is proportional to the square root of the stress.

Very similar conclusions can be made for the proposed model for circular membranes 4.9, even though the effects of stress seem to be less significative in this case. However, this model remains an approximation for design. The sensitivity curves of it are displayed in Figure 4.3.

4.2 Modelling the stacks

In order to model the stacks, several parameters need to be addressed. The stacks must be designed to fulfil both thickness and residual stress requirements. In order to enable this, an equivalent material representing the full stack is needed. To this end, equivalent material parameters for the density, Young's modulus and Poisson's ratio are modelled. The equivalent residual stress is also determined using a simple weighted average model in order to allow for quick estimation and rapid design decisions. Last, some stack design are proposed for a fixed residual stress and thickness.

4.2.0.1 Equivalent material parameters

The materials used inside the proposed stacks are SiO_2 and Si_3N_4. In order to estimate the properties of an equivalent material, their characteristics are given in Table 4.3.

It can be seen that the densities are close so their are assumed to be close enough to have the same value. The chosen value is taken as being in the intersection of both ranges. The large ranges can be explained by the fact that this parameter can be impacted by the deposition technique used. For the Young's modulus and the Poisson's ratio, weighted averages were used with the layer thickness as weight.

Material parameter	SiO_2	Si_3N_4
Density ρ [kg/m^3]	2170 to 2650	2370 to 3250
Young's modulus E [GPa]	66.3 to 74.8	166 to 297
Poisson's ratio ν	0.15 to 0.19	0.23 to 0.28

Table 4.3: *Material parameters of silicon dioxide from [34] and silicon nitride [35]*

4.2.0.2 Equivalent residual stress in stack

The simplest approach was used in this work and the equivalent residual stress is considered to be the weighted average of the residual stress in each layer. The model is therefore simply :

$$\sigma_{eq} = \frac{\sum_{i=1}^{n} \sigma_i t_i}{\sum_{i=1}^{n} t_i} \tag{4.10}$$

with :

- σ_{eq}, the equivalent residual stress of the full stack,
- σ_i, the residual stress is layer i,
- t_i, the thickness of the film of layer i,
- n the number of layers in the stack.

Material	Deposition process	Expected residual stress [MPa]
SiO_2	Wet thermal oxidation	-300
SiO_2	PECVD and thermal annealing	-70
Si_3N_4	LPCVD and thermal treatment	1050
Si_3N_4	PECVD	300

Table 4.4: *Available materials and deposition processes for stack design and expected residual stresses [36]*

In this case, the layers were assumed to be either SiO_2 or Si_3N_4 with various deposition methods resulting in various residual stresses in the deposited layer. Thermal treatment for stress annealing were also taken in account. Some very classical deposition or growing techniques for thin films were chosen based on the available machines in the Winfab facility. The list of thin film types is given in Table 4.4.

The goal of the designed stack are to have equivalent residual stress close to 50MPa and a thickness of 1μm. These values can at this stage be considered as examples used in the following Figures as the choice for these parameters is done later in the design process. This can be done by using two to three materials with at least two presenting opposite residual stresses.

The first step was to adapt a stack used in previous projects of the laboratory [37, 31]. It is based on one 400nm layer of wet thermally oxidised SiO_2. The second layer is Si_3N_4 deposited using LPCVD and thermally treated to increase the residual stress. The final layer is made out of SiO_2, PECVD deposited and thermally treated for stress annealing. The thickness of the thermally oxidised SiO_2 was preserved and the two other layers are determined according to the goal stress.

Next step was to design stacks with a same total thickness but different material layers. The propositions are a Type A stack with thermally deposited SiO_2 and PECVD Si_3N_4 and a type B stack featuring a PECVD SiO_2, thermally treated for stress annealing and a PECVD Si_3N_4 layer on top. The design curves for these stacks and the one adapted from the silicon oxide-nitride-oxide (ONO) stack in [37, 31] are represented in Figure 4.4. The three stack designs matching the 50MPa residual stress goal are displayed in Figure 4.5. The goal is to compare these stacks to each other in terms of fabrication ease and eventually performances afterwards.

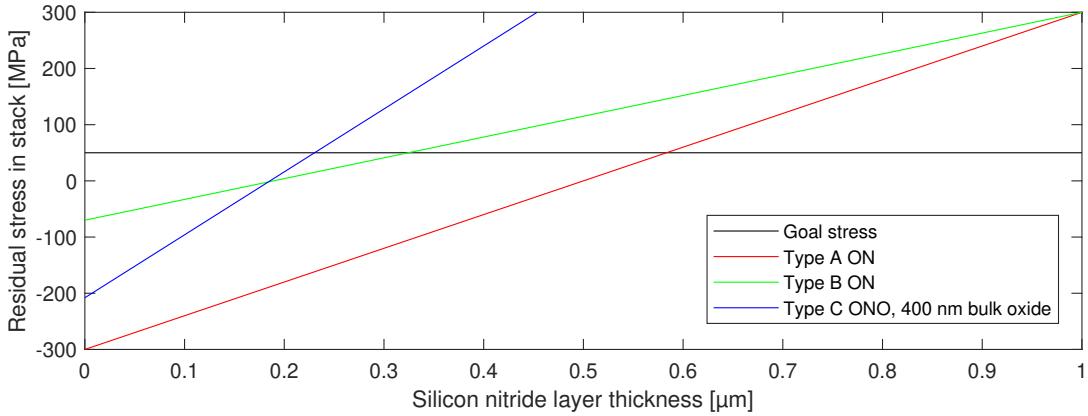

Figure 4.4: *Design curves for the silicon nitride layer to obtain the goal stress of 50 MPa with a silicon dioxide layer determined relatively to it for a total thickness of 1 µm of the stack*

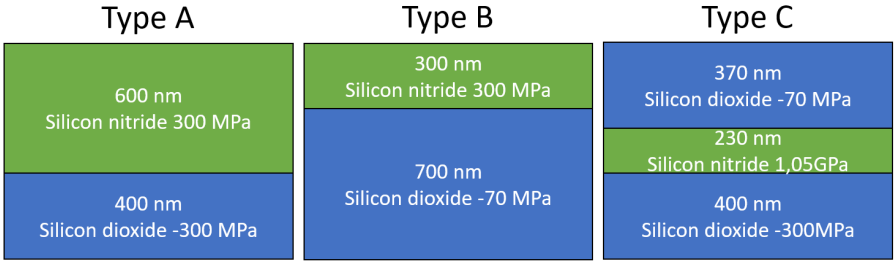

Figure 4.5: *Selected stack designs based of Figure 4.4*

4.3 Results of the models

Using these models and comparing to some references, parameters can be chosen to head towards a design curve and then membranes to simulate and fabricate.

Based on the observation that a high aspect ratio between the membrane side length and its thickness is better for low resonant frequencies, as seen in Figures 4.2 a and b, it is decided to go for thin membranes. The choice is made to use 1µm-thick stacks as thinner membranes would not enable to lower the frequency much more. This thickness is also of the same order of magnitude as in [37, 31].

Each of the stack designs from Figure 4.5 can thus be used in this project. The sensitivity curves can then be compiled in design spaces. The Figures 4.6 and 4.7 present the design spaces for respectively square and circular membranes.

The 50 MPa tensile stress is chosen as it gives frequencies in the order of magnitude that is needed for PD detection for less-than 2mm side membranes. It also seems to be a low but attainable value with SiO_2/Si_3N_4 stack in [29]. Plus, an increase in the stress has strong impact on the resonant frequency.

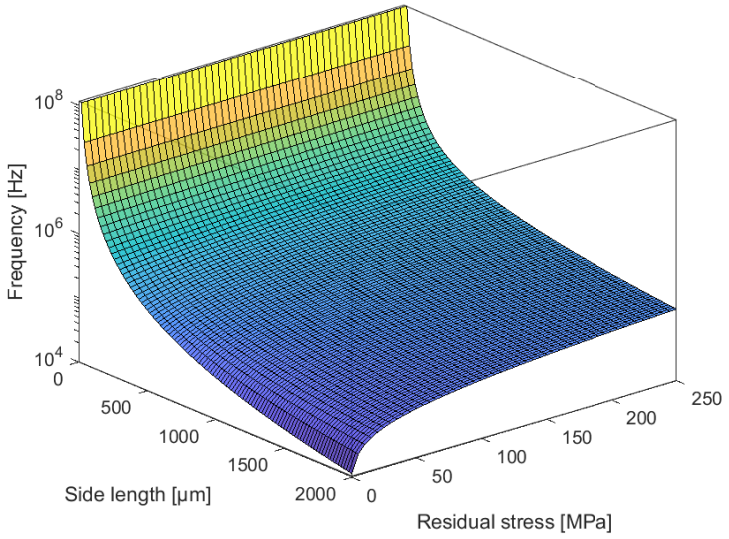

Figure 4.6: *Design space for 1µm-thick square membranes based of model 4.4*

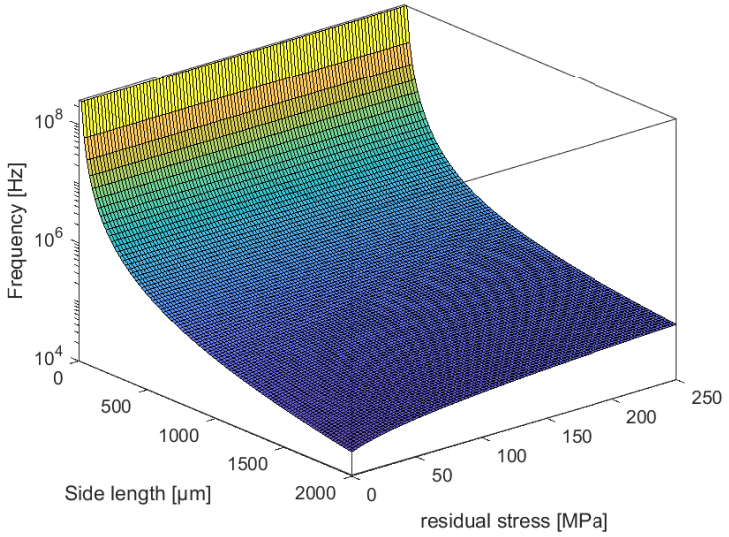

Figure 4.7: *Design space for 1µm-thick circular membranes based of model 4.9*

The design curves for a 1µm thickness and a 50 MPa tensile residual stress are shown in Figure 4.8. Several membrane sizes have been selected to form the acoustic filter set with resonant frequencies at interesting values for the examined signals. The membranes sizes were chosen to be as given in Table 4.5 and are also indicated in Figure 4.8 as the red dots.

Each of these membrane sizes will be simulated for each of the proposed stacks in the next sections. The proposed designs are displayed in Figure 4.9. The membranes are fully clamped as in the theoretical models.

4.4 COMSOL simulations of simple membranes

This section details the simulations that have been performed using the Comsol Multiphysics software. This software enables to perform finite elements method (FEM) simulations and link together several physical aspects of a same project in one simulation.

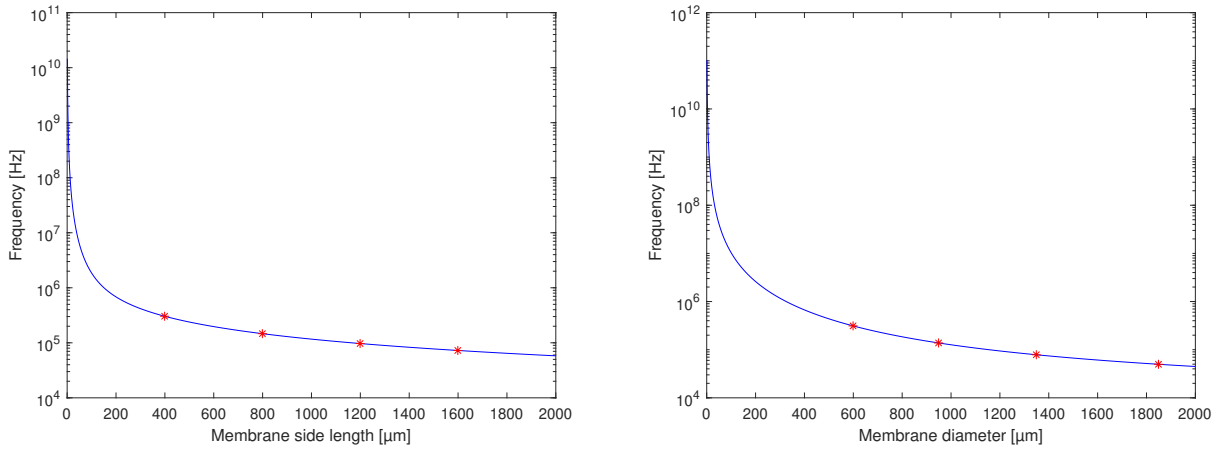

Figure 4.8: *Design curves for a) square membranes and b) circular membranes extracted from the design spaces above. The red dots indicate the chosen membrane sizes.*

Form	Diameter or side length [µm]	Expected first mode frequencies [kHz]
Square	1600	73
Square	1200	97
Square	800	147
Square	400	304
Circle	1850	50
Circle	1350	79
Circle	950	138
Circle	600	312

Table 4.5: *Design choices for the membranes sizes related to the expected frequencies*

In this project it was first used to understand better the behavior of the multilayered stack of material and its impact on eigenfrequencies of the future fabricated membranes. This simulation was performed in vacuum at first to simplify the situation and isolate the effect of the stack.

A multiphysic simulation was also performed to link acoustics and mechanics. The goal here was to underline the effects of damping that could be expected in air. This simulation is important as the effective measurement for resonant frequency are done at atmospheric pressure. Actually measuring the real membranes in vacuum would have required a very complex setup but would have allowed to determine the exact effect of damping by comparison with atmospheric pressure results.

Other parameters such as temperature were left constant at this stage. Varying these could change the obtained frequencies as the residual stresses in a membrane are the result of different thermal ex-

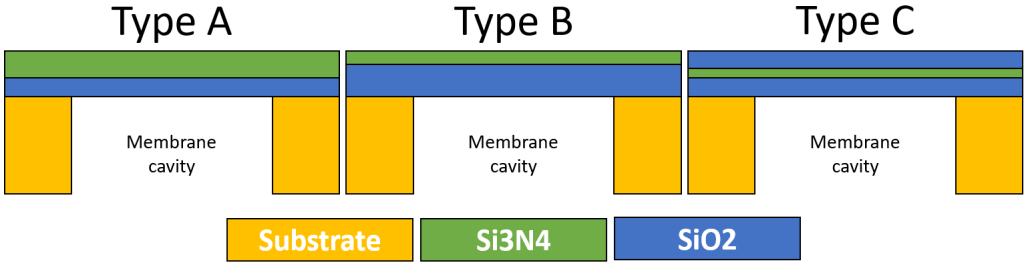

Figure 4.9: *Proposed designs for each type of stack, the membrane cavity is fully open on the backside as the membranes are fully clamped*

pansion coefficients in the different materials composing a stack. The chosen materials in this project were either thermally oxidised at temperatures as high as 900 to 1100°C or deposited using a PECVD facility at around 300°C. Given this, it is considered that small temperature variations would have small impact on the residual stress in the stacks.

4.4.1 Simulating the stack for membranes with multilayer material

Comsol offers a possibility to simulate layered linear elastic materials by creating an equivalent material. This material combines the properties of all the materials according to the stack design in terms of thickness, fiber or cristallographic orientation and order of the materials in the stack and it generates a set of equivalent mechanical properties.

Using this equivalent material design allows to use a more precise stack behavior for finite element methods (FEM) simulation of the membranes. This model is more precise than simply working with the equivalent material proposed in section 4.2 that relies on weighted averaging of most parameters.

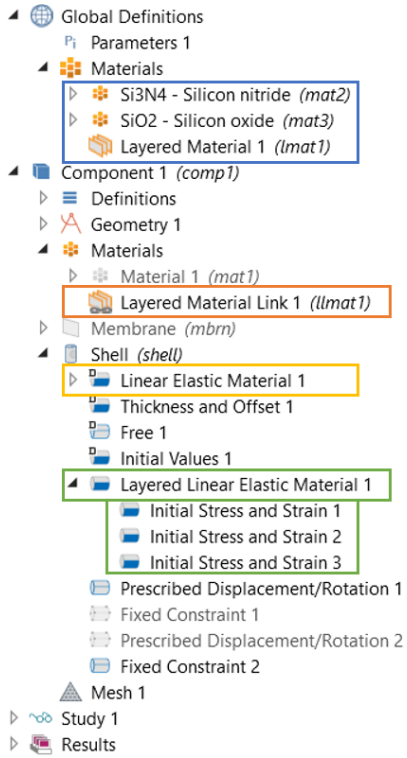

Figure 4.10: *Model Builder from COMSOL for the implementation of a layered material*

First step to create a multilayer stack is to select the materials that will compose it under the "Materials" section of the "Global Definitions". Once these are gathered, they can be assembled in the same section as a "Layered Material". This can be seen in the blue frame in Figure 4.10 presenting the Model Builder window that structures every Comsol simulation.

The "Layered Material" can then be defined. It consist of a list of every layer in the stack and allows to specify their order, thickness, material from the selected list and rotation from a reference orientation. This orientation setting is especially useful for material that have specific crystallographic structures or that includes fibres. It was left to zero in this project. The resulting stack definition can be seen in Figure 4.11 and the stack representation in Figure 4.13 for the Type C ONO stack proposed in this project.

The interfaces must also be defined. Their position must be given as in Figure 4.12.

Once the multilayer material is defined, it can be used in a component. The first step is to use a link in the Material section of the component, as in the orange frame in Figure 4.10. Next, under the Shell description, both the "Linear elastic material" and the "Layered Linear Elastic Material" options under the shell module are necessary to use the multilayer material. They are located in yellow and green frames of Figure 4.10 respectively. The initial stresses and strain can then be applied layer by layer under the "Layered Linear Elastic Material 1" of the Shell module. This enables the adaptation of the residual stress in each layer of the membrane.

Layer	Material	Rotation (deg)	Thickness (m)	Mesh elements
Box oxide	SiO2 - Silicon oxide (mat3)	0.0	thic_box	2
Stack Si3N4	Si3N4 - Silicon nitride (mat2)	0.0	thic_nit	2
Stack oxide	SiO2 - Silicon oxide (mat3)	0.0	thic_ox	2

Figure 4.11: *Stack composition in Layered Material*

Interface	Position (m)
Box oxide down	0
Box oxide-Stack Si3N4	thic_box
Stack Si3N4-Stack oxide	thic_box+thic_nit
Stack oxide up	thic_box+thic_nit+thi...

Figure 4.12: *Interface definition and position in Layered Material*

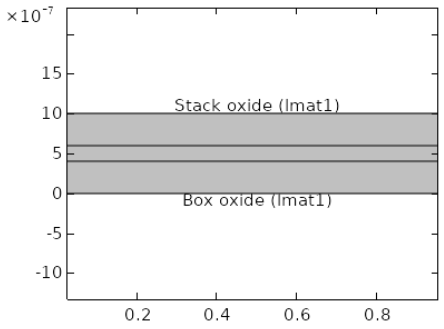

Figure 4.13: *Stack view of the layered material*

4.4.2 Multilayer membranes in vacuum

This section explains what simulations were put in place using the multilayer material option that was covered in section 4.4.1 and how they were used to anticipate fabrication results. First, the simulation building is reviewed and the boundary conditions are examined. Next, the studied parameters and the computations run are detailed. Last, results are presented and the first resonant modes obtained are compared to the theoretical design curves from section 4.3.

Geometrically, the membrane is built using a work plane and its form is traced in plane geometry. It is kept as simple as possible to reduce computation time. The forms used here are either a square or a circle. This is sufficient since the thickness of the object is set in the shell or membrane module afterwards. These choices were made based of a Comsol model [38] as the present simulation was firstly adapted from a tutorial to simulate simple vibrating objects. In this case, the shell module of Comsol was used to create the objects to study instead of the membrane module due to compatibility issues with the Layered material option [39].

In the model builder from Figure 4.10, the first parameters are the thickness. Thickness is set to the global thickness of the stack. Next come the initial stress and strain that were discussed in section 4.4.1 and are set for each layer to the expected residual stress from fabrication. Last are the boundary conditions. Since the membrane is considered as fully clamped, it is decided to used a prescribed displacement of zero along the z-axis and a fixed constraint on each of the borders of the membrane.

The same simulations were repeated for each form and each stack design. The studied parameters were the six first eigenfrequencies of the membranes and their frequency response. These are computed in vacuum for this simulation so damping is always zero and the quality factor is hence infinite.

4.4.2.1 Results of the multilayered simulation

The results in terms of eigenfrequencies are represented in Figures 4.16, 4.17 and 4.18. It can be seen that each of the graphs present only four visible datapoints instead of the six awaited. This is caused by the fact that some resonance modes occur at very close frequencies. This can also be noted when examining the data from Tables 4.6 and 4.7.

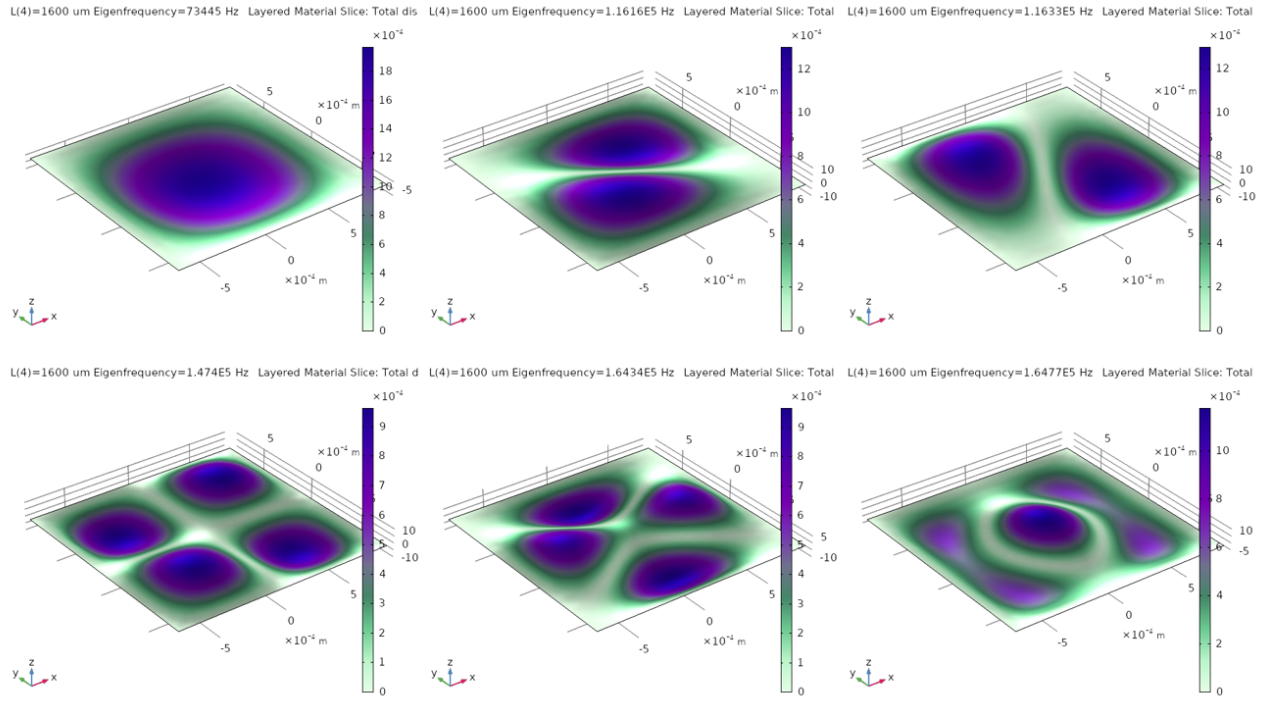

Figure 4.14: *Illustration of mode shapes for the six computed eigenfrequencies of a square membrane*

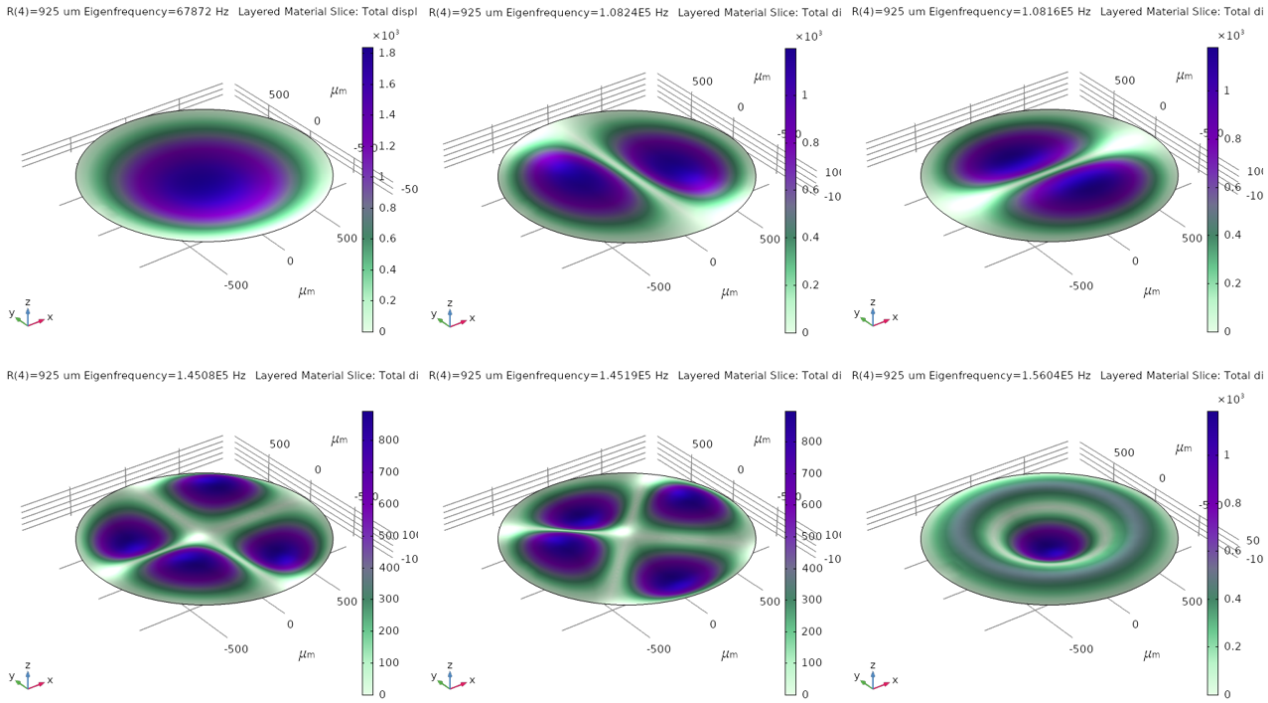

Figure 4.15: *Illustration of mode shapes for the six computed eigenfrequencies of a circular membrane*

The six modes share the same shapes across all stacks and are illustrated in Figures 4.14 and 4.15. When comparing between square and circular shapes, the tendency is to have lower resonant frequencies for every mode if the membrane is circular. This is in line with theoretical models available in the state of the art [20] and can be linked to the fact that deflection is larger in circular membranes than in square ones. The obtained mode shapes are however very similar from square to circular form. Last phenomenon that can be noted is the pairing of two very close resonant frequencies for very similar modes can be observed in both case. Since the presented mode shapes look so similar, having very close eigenfrequencies makes sense. However, the question of considering them as the expression of a

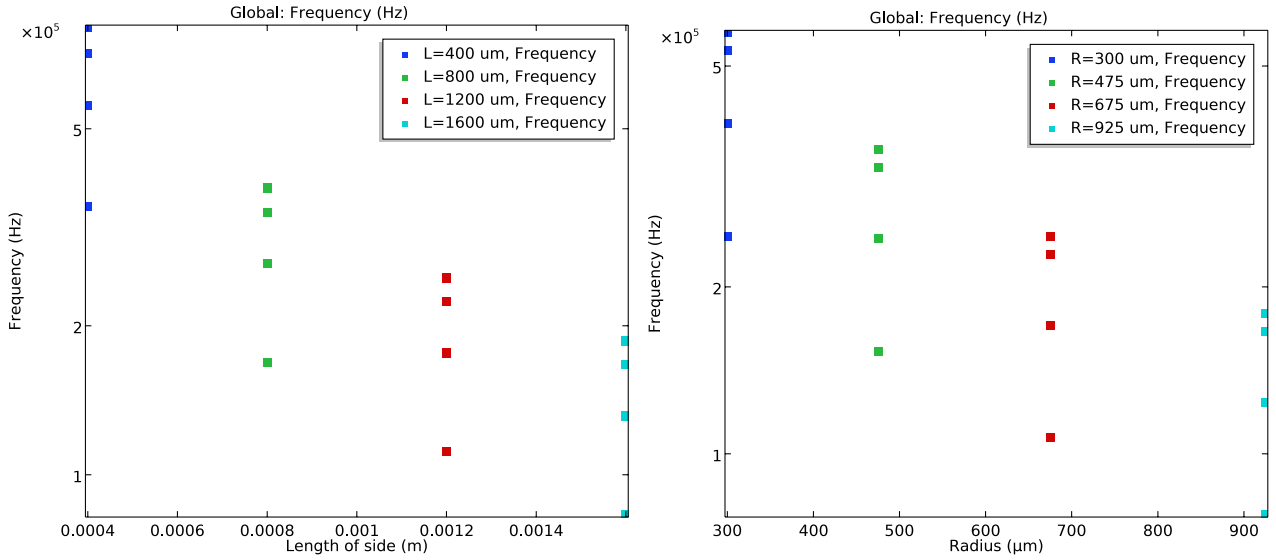

Figure 4.16: *Six first eigenfrequencies for a Type A-stack membrane a) square and b) circular shape*

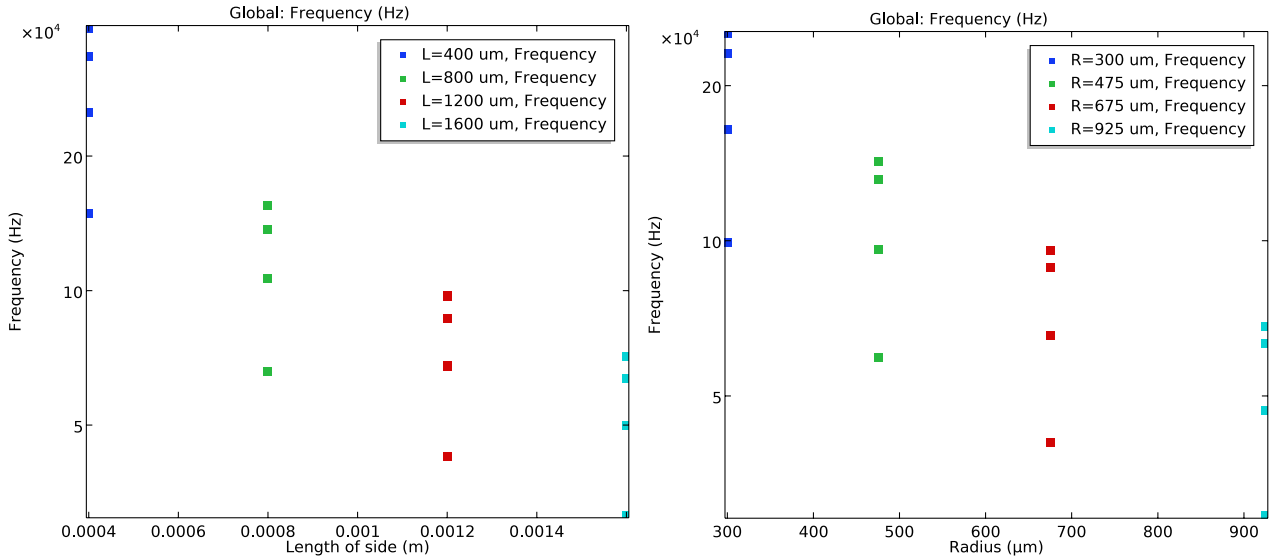

Figure 4.17: *Six first eigenfrequencies for a Type B-stack membrane a) square and b) circular shape*

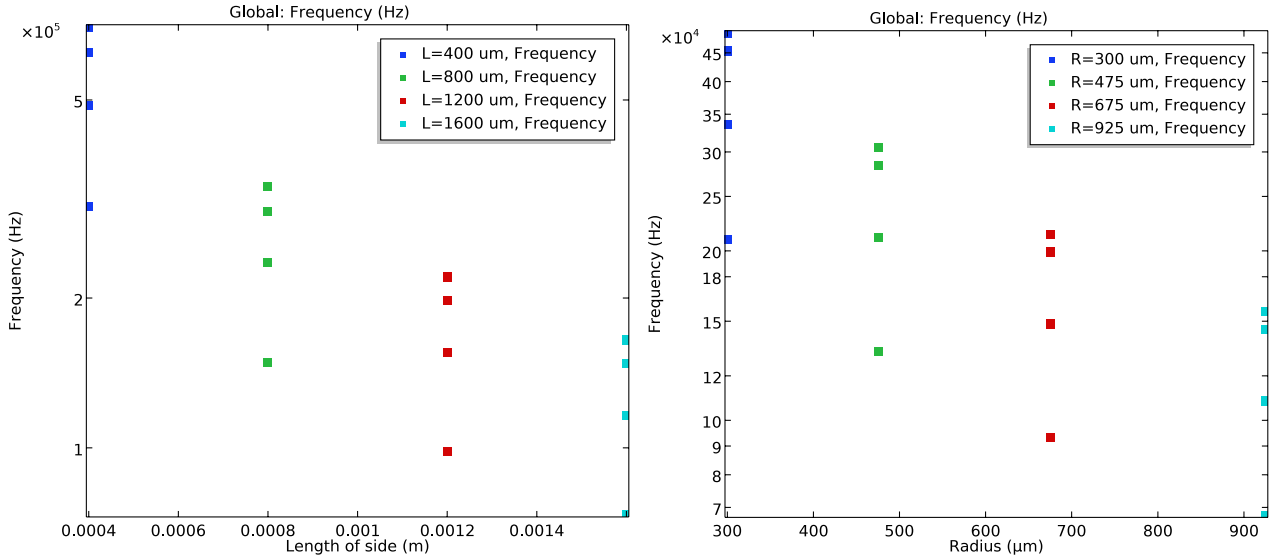

Figure 4.18: *Six first eigenfrequencies for a Type C-stack membrane a) square and b) circular shape*

same mode shape could be asked. Actually, no difference would be made between these mode shapes in a theoretical model only accounting for the number of nodes per side or the nodal diameters and circles.

Comparing the stacks, the frequency values obtained for the Type B stack are significantly lower than the ones obtained with the two other stacks. This tendency can be seen for all sizes, all modes and both shapes. The ratio between the Type B stack values and the ones of other stacks is between 1/2 and 1/3. Since the tendency is a general behaviour, it could be linked to the Type B stack. It is composed of thermally annealed PECVD SiO_2 and PECVD Si_3N_4. As it is the only stack relying entirely on thermally treated SiO_2 for the compressive layer, it could impact the computation of the equivalent material parameters of the stack. This could be confirmed or not by measures after fabrication.

Stack	Size	Mode 1: 11	Mode 2: 12	Mode 3: 21	Mode 4: 22	Mode 5: 22 bis	Mode 6: 31
Type A	1600	83.1	131.4	131.6	166.7	186.0	186.4
Type A	1200	111.2	176.0	176.3	223.4	249.4	249.9
Type A	800	168.5	267.0	267.2	339.0	379.2	379.7
Type A	400	348.2	556.2	556.4	710.7	800.1	800.5
Type B	1600	31.8	49.9	49.9	63.5	71.1	71.3
Type B	1200	42.5	67.7	67.8	86.6	97.2	97.4
Type B	800	65.9	106.2	106.3	136.8	154.8	155.0
Type B	400	148.5	250.3	250.3	333.8	386.5	387.2
Type C	1600	73.4	116.2	116.3	147.4	164.3	164.8
Type C	1200	98.3	155.5	155.7	197.3	220.3	220.7
Type C	800	148.7	235.6	235.8	299.0	334.3	334.7
Type C	400	306.1	488.0	488.2	622.4	699.7	700.1

Table 4.6: *Eigenfrequencies values in kHz from Comsol simulation in vacuum depending on the type of stack and the side length of a 1µm thick square membrane*

Stack	Size	Mode 1: 00	Mode 2: 01	Mode 3: 01bis	Mode 4: 02	Mode 5: 02bis	Mode 6: 20
Type A	1850	77.7	123.9	123.9	166.3	166.3	178.7
Type A	1350	106.9	170.6	170.6	229.1	229.1	246.3
Type A	950	153.0	244.4	244.5	328.7	328.7	353.7
Type A	600	246.1	394.3	394.4	532.6	532.7	574.1
Type B	1850	29.3	46.8	46.9	63.2	63.2	68.1
Type B	1350	40.7	65.4	65.4	88.7	88.7	95.6
Type B	950	59.3	96.0	96.1	131.5	131.6	142.4
Type B	600	99.2	164.4	164.4	230.7	230.7	251.9
Type C	1850	67.9	108.2	108.3	145.1	145.2	156.0
Type C	1350	93.0	148.3	148.5	199.1	199.2	214.2
Type C	950	132.3	211.1	211.3	283.6	283.9	305.3
Type C	600	209.8	335.5	336.1	452.5	453.3	487.8

Table 4.7: *Eigenfrequencies values in kHz from Comsol simulation in vacuum depending on the type of stack and the side length of a 1µm thick circular membrane*

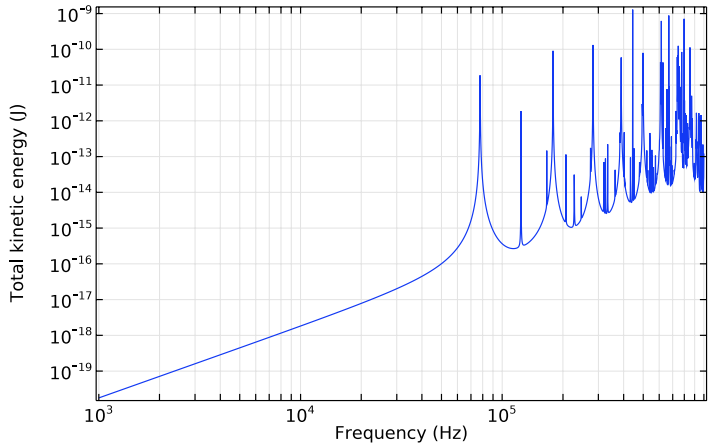

Figure 4.19: *Total kinetic energy frequency response of the 1850µm diameter membrane in vacuum*

The frequency response is also extracted in term of kinetic energy. It can be seen in Figure 4.19. It can be observed that the first mode is around 80kHz, close to the 77.7 kHz awaited. The other modes also show high kinetic energy which reflects the speed of the membrane. However, it does not mean the displacement will be as large as the one of the first mode. A large speed can be obtained if displacement is very large or if frequency of the periodic movement is very high.

4.4.3 Multiphysic acoustic-shell simulation for damping effect estimation

This section describes the multiphysics acoustic-shell simulation that was put together to investigate the impacts of damping on the previously obtained results. The main goal is to compare the frequency response and the eigenfrequencies for a 1850 μm-diameter membrane in air to the vacuum version above.

First step is to build the simulation. It was done using the multiphysics interfaces from Comsol Multiphysics. The main difference with the simulation from section 4.4.2 lies in the geometric construction and in the used modules to build the studied objects. The same implementation was used for the layered material of the membrane.

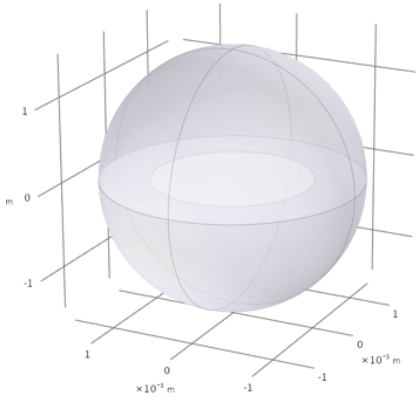

Figure 4.20: *Geometry for multiphysics acoustic-shell simulation*

The geometry is built to include the impact of air on the membrane. To do this, the membrane is included into an simplified die-like environment. First, the membrane and the area around are defined in a workplane and next a sphere is built around this workplane. The membrane will be assigned the same layered material as in the multilayer simulation and the sphere will assigned air. The illustration of this geometry is visible in Figure 4.20. The geometry section is framed in blue in Figure 4.21.

To build the modules of this simulation, two modules are used : the "Pressure Acoustics, Frequency Domain" one and the "Shell" one. Both are linked by the "Multiphysics" module where the interface between the two domain of application is coordinated. This coupling is adapted from the Comsol tutorial [40].

In the acoustic module, framed in orange in Figure 4.21 the pressure acoustics is applied to the two half-spheres. An "Interior Sound Hard Boundary (Wall)" is applied around the membrane to figure the die that would not let sound pass through. To finish this module, a constant pressure is applied under the membrane, here set at the atmospheric pressure. The same assembly was done in the shell module as in section 4.4.2. The domain selection only covers the membrane. This section is framed in green Figure 4.21.

Last, the multiphysics coupling is applied to the membrane using an "Acoustic-Structure Boundary". This coupling is framed in yellow in Figure 4.21.

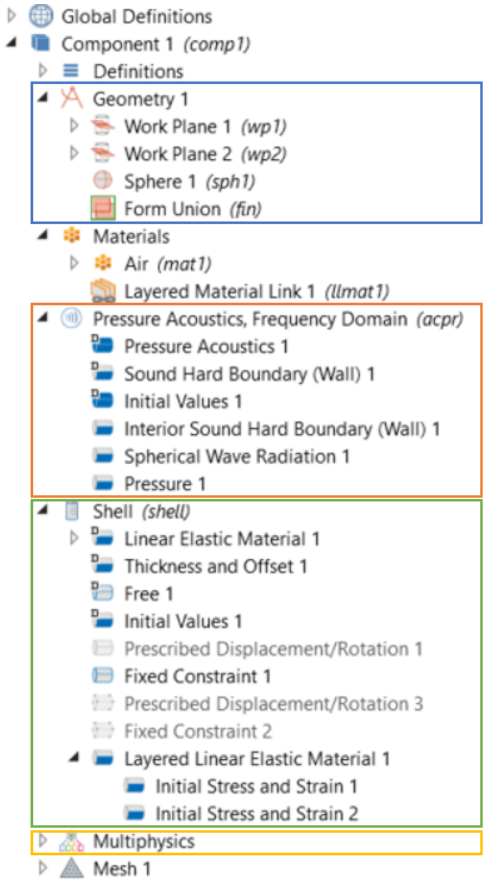

Figure 4.21: *Model builder of the acoustic-shell multiphysics simulation*

This simulation was done to understand the damping behavior. To simplify, it was only done for one case to compare it with the multilayer in vacuum. The chosen case is the 1850μm diameter with the type A stack.

4.4.3.1 Results of the acoustic-shell multiphysics simulation

The same results were extracted as for the multilayer simulation : the frequency response in term of kinetic energy of the membrane and the eigenfrequencies with the mode shapes. Here the damping and quality factor were also extracted. These results can be seen in Figure 4.22 and Table 4.8 respectively. The mode shapes are the same as in section 4.4.2.

Comparing the Table 4.8 with the total kinetic energy frequency response in Figure 4.22, the six first modes can be identified as the four first peaks in the graph. This is due to the same phenomenon of pairing of mode shapes observed in section 4.4.2. In this case, the modes all show smaller kinetic energy as they are higher.

Mode Shape	Frequency [Hz]	Damping factor [x10^{-6}]	Quality factor [x10^{5}]
00	3896	3.5	1.4
01	8318	0.4	13.3
01 bis	8380	0.4	13.1
02	14 227	0.1	63.7
02 bis	14 497	0.1	35.9
10	15 289	4.4	1.1

Table 4.8: *Eigenfrequencies of 1850µm diameter membrane in air*

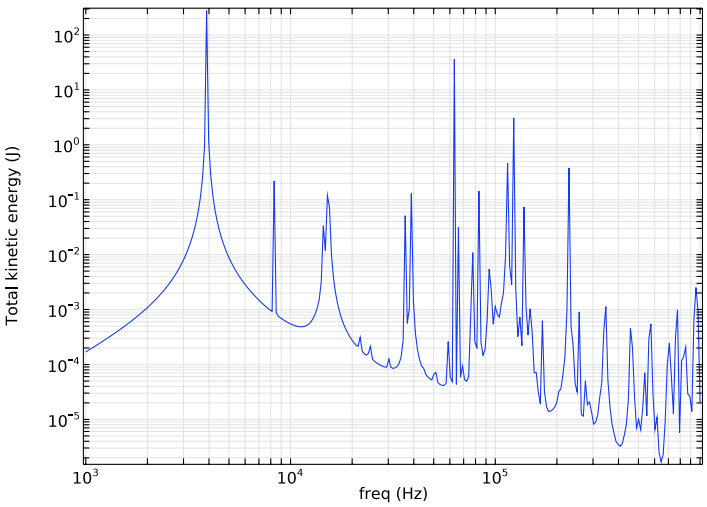

Figure 4.22: *Total kinetic energy frequency response of the 1850µm diameter membrane in air*

4.5 Comparison of simulation results with analytical models

This section compares the simulation results obtained using Comsol Multphysics with the expected values from the analytical models used in section 4.3 for design. The main goal is to anticipate on how the planned fabrication could impact the resonant frequencies.

Figures 4.23 and 4.24 compare the frequency of the first resonant mode for each membrane size and stack for respectively a square and a circular membrane. It can be observed that the Type A and C stacks expected values are close to the model predictions is both case whereas Type B simulations present way lower frequencies. This follows the observation from section 4.4.2.

Comparing between the square and circular cases, it can be noted that the simulation and model are closer for the square shape than the circular. The model proposed for the circular membranes seems to be close enough to simulation yet not perfectly precise. The datapoints from the simulations follow a flatter curve than the one proposed so the diameter impact is probably overestimated in the model. The expected resonant frequency of the larger membranes could thus be larger than expected and the smaller ones would show lower first mode.

Regarding the simulation in air, the values of the eigenfrequencies from Table 4.8 are much lower than these obtained for the same membrane in vacuum. The effect of damping is not taken in account in the theoretical models. However the simulation from section 4.4.3 suggests that it could strongly decrease the resonance frequency even though the residual stress is tensile. This strong decrease is estimated to be a around factor 7.5 between the values from Table 4.8 and these from Table 4.7. Such a factor is stronger than what was found in the state of the art where the strongest factor was less than 2 [41].

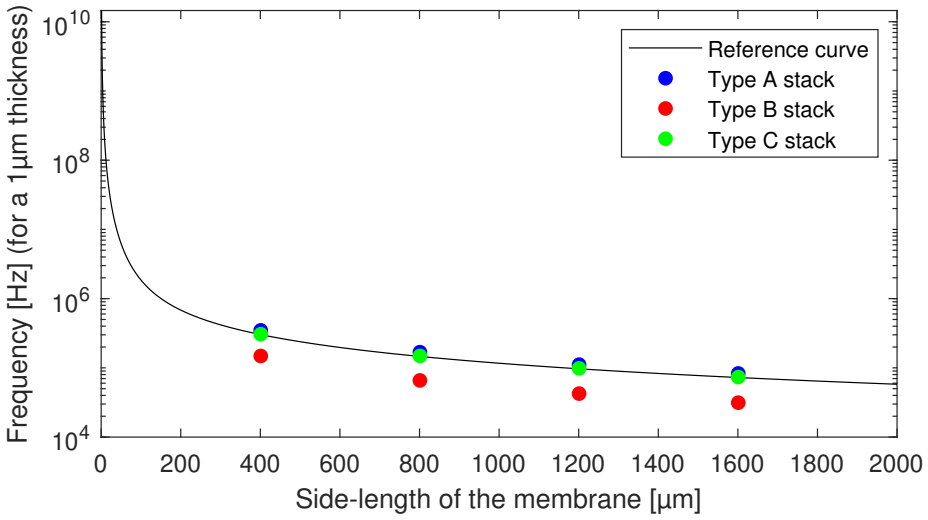

Figure 4.23: *Comparison of the first eigenfrequency between analytical model 4.4 and the results of the Comsol simulation of each stack type*

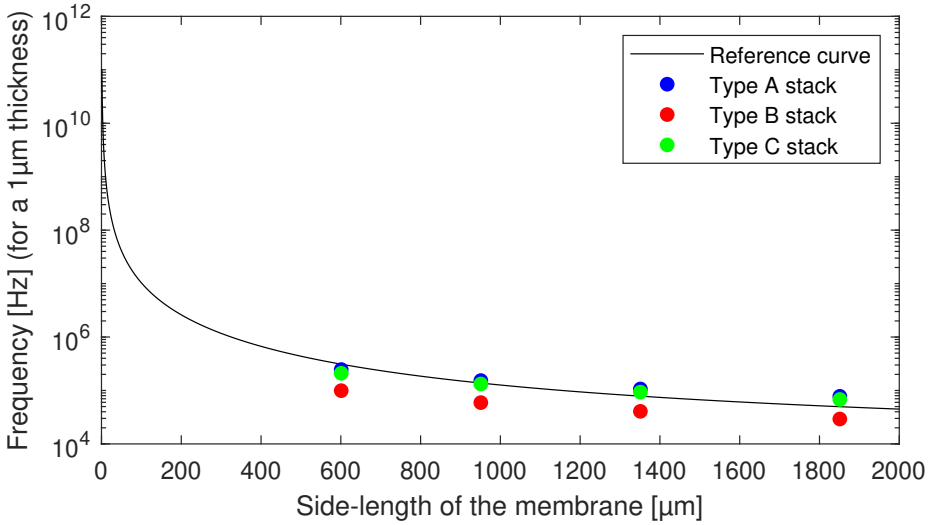

Figure 4.24: *Comparison of the first eigenfrequency between analytical model 4.9 and the results of the Comsol simulation of each stack type*

5 Fabrication process

This section details the fabrication process that have been realised in this work. The main goal of this process is to create membranes, such as represented in Figure 5.1 with controlled first mode resonant frequencies based of the design choice done in the "Models and simulation" Chapter 4 in order to test them. The main parameters of interest are the membrane thickness, its width and the global residual stress in its stack. This should serve as preliminary process validation towards a full sensor using membranes of this type.

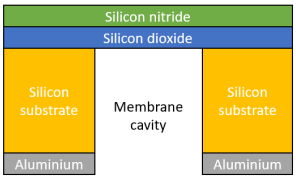

Figure 5.1: *Illustration of the structures*

The mask design based of the design choices that have been made in the previous section is first presented, followed by the process sheet and sectional views of the stacks. Next, the processing is detailed in three sections : the stack itself, the backside aluminium mask and the etching of the membranes. The interests and impacts of grinding the dies before the etching is then discussed before the presentation of the resulting membranes.

5.1 Mask design for test membranes

This process only requires one mask in order to release the membranes from the backside of the substrate. The proposed design includes several sizes and both square and circular membranes. Since this is a test process in order to validate the membrane design, the membranes have been grouped by size and by form for the larger ones to ease the process. Six dies designs have been proposed and incorporated in a mask set for another process. All of these have been designed using the Cadence software.

Grouping the membranes by size ensures a more even etching since the decision was made to etch the dies once diced. Etching dies instead of a whole wafer at a time enables to test the etching recipe used and to adapt it to the membrane sizes and form since etching is a surface-to-etch and density dependent process. This is linked to the aspect-ratio dependent etching (ARDE) phenomenon. In this case, the aspect ratio between the depth to etch and the side length or diameter of the membranes varies from 1:1 to 1:6 approximately. The choice to group them ensures that the finish of the etching can be adapted to the aspect ratio and that overetching does not break some membranes.

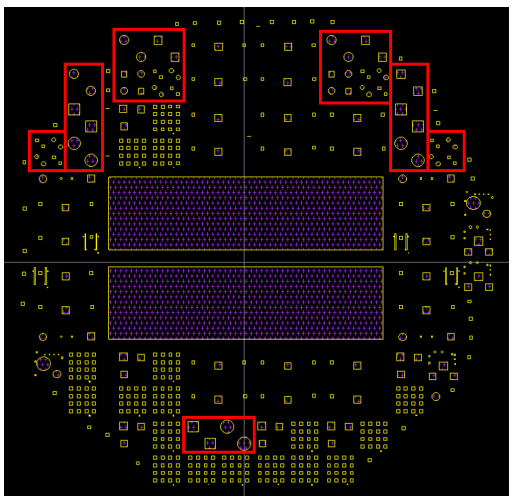

Figure 5.2: *Full mask designed for the process*

The diagonal placement of the membranes on the dies aims to make the density of etched surface as constant as possible over the die. It also improves the mechanical integrity of the die after etching, resulting in less fragile dies.

Regarding the design, the membranes should be of the same size as the mask and etching is planned to be done from the backside because they are designed to be fully clamped membranes. RIE will thus be chosen over TMAH, liquid etchant that presents a varying selectivity across the different crystalline orientations of the silicon substrate, and XeF_2, an isotropic gas etchant, since both circular and square membranes are on the same die for small designs. A TMAH-release would not preserve the form of the designs on the mask for the circular membranes and a XeF_2-etching would distort the pattern of square membranes to the point of making it almost totally circular.

In total six dies are designed with four basic configurations that are displayed in Figure 5.3. The parameters for each design including the size of the membranes in the design, the used configuration and the values of every mask design parameter indicated in the configuration Figure 5.3 are given in Table 5.1.

The configurations a is used for the dies with large square membranes, with side-length of 1600 μm for design β and 1200 μm for the δ one. The die design α with 1850 μm diameter membranes and the γ one with 1350 μm both use configuration b. Each of these dies features two membranes of the same form and size, placed in diagonal to ensure the surface density to etch is as constant as possible. These designs are displayed in Figures 5.3 a and b.

Last two configurations, b and c, feature the smaller membranes. Configuration c is used for die design ϵ compiling the membranes with a diameter of 950 μm and the ones with a side length of 800 μm. They present the same diagonally organised pattern as the configurations a and b but four membranes, two square and two circular ones, are placed on each diagonal. This die design is presented in Figure 5.3 c. Last configuration is used for design ζ. This design features 600μm-diameter membranes and their 400 μm-side homologous. The diagonal disposition is kept and the die gathers 8 membranes, 4 of each form as shown in Figure 5.3 d displays it.

Finally, once all the dies were designed, they were assembled all together on the mask dedicated to the backside release of membranes. These designs share the mask with another process and are indicated with red frames on the final design of the full mask in Figure 5.2. The dies used for this process are located on the sides of the mask, which results often in etching properties being less constant. However since etching will be done die per die and can thus be replaced at the center, this will not have much impact.

Die design	α	β	γ	δ	ϵ	ζ
Membranes sizes [µm]	⌀ 1850	1600	⌀1350	1200	⌀950 & 800	⌀600 & 400
Die design	B	A	B	A	C	D
a	-	1600	-	1200	800	400
b	-	450	-	650	850	600
c	1850	-	1350	-	950	600
d	375	-	575	-	775	450
e	5000	5000	5000	5000	5000	5000
f	2500	2500	2500	2500	2500	2500
g	-	-	-	-	-	500
h	-	-	-	-	-	400

Table 5.1: *Parameters used in the mask design for the different dies*

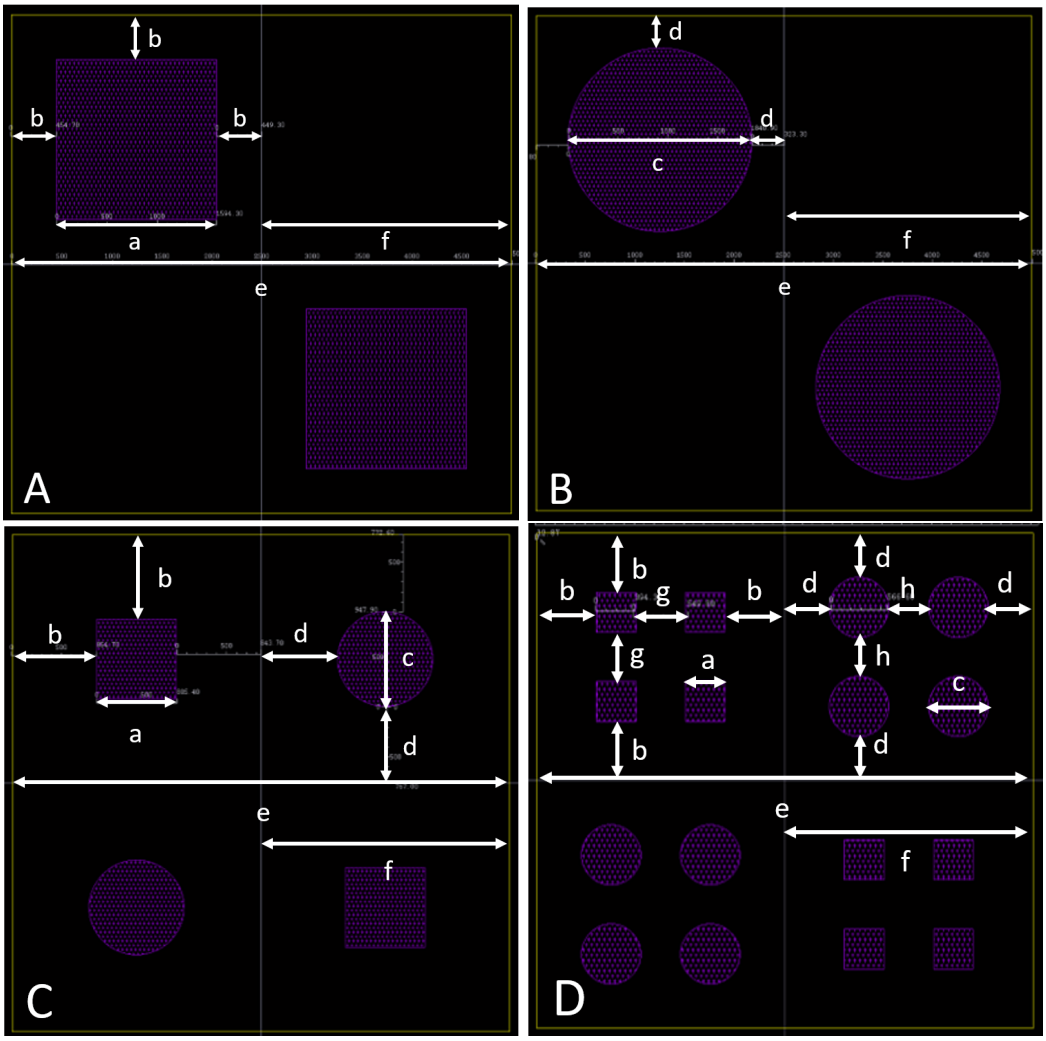

Figure 5.3: *Dies configuration a) α : 1600 μm of side length and δ : 1200 b) α : 1850 μm of diameter and γ: 1350 c) ϵ : 800 μm of side length and 900 μm of diameter d) ζ : 400 μm of side length and 600 μm of diameter, the value of every parameter indicated in this Figure is given in Table5.1*

5.2 In-process metrology techniques

To evaluate the on-going process and ensure each step has been done correctly before heading to the next, several metrology techniques are used. In this process, ellipsometry and profilometry were used for several purposes. This section reviews quickly the metrology techniques and their use in the process.

5.2.1 Ellipsometry for thickness measurement of transparent layers

The Sentech spectroscopic ellipsometer available in the Winfab facility was used for the measurements of the thin deposited dielectric films. The main purpose of such measurement in this project is to determine the thickness of the deposited films to check whether or not they comply with the requirements. The obtained thickness value was then used in the computations of the residual stress in the film.

The main principle behind spectroscopic ellipsometry is to measures the change in polarization of a light beam after it gets reflected on a material stack. To analyse properly the obtained results, they are compared to a reference and fitted. To this end, a model of the stack of the exposed sample must be provided to the software of the apparatus. An example of one of the model used is given in Figure 5.4.

The results do not only include the thickness of the observed film but its optical characteristics as well. In this project, the refractive indices were only used as an indication of the material quality since their values do not impact directly the resonant frequency of the membranes. However, they allowed to adapt recipes to have a correct quality of PECVD-deposited materials. The quality of the material was assessed by comparing the obtained refractive index to the reference.

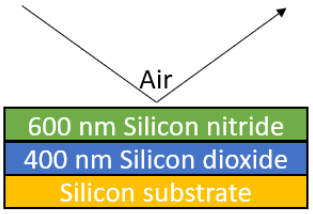

Figure 5.4: *Example of stack provided to the ellipsometer software*

5.2.2 Curvature-based residual stress measurement in wafer using Stoney formula

Controlling the stress in a stack of material requires to take measurement of the global curvature of the wafer at each step and compare this measurement with the preceding one to determine by how much the stress evolved in the just-done step. This measurement procedure is explained before going into the details of each oxidation or deposition technique that is used in the material stack.

In order to control the residual stress, the wafer curvature has been measured before and after each manipulation with a profilometer. This curvature measurement is then used with the Stoney formula to determine the residual stress resulting from the manipulation.

The measurement is taken with the Vecoo Dektak 150 profilometer along 5,5cm on 60 seconds generating 18 000 measuring points. The wafer is always measured along the diameter perpendicular to the flat to ensure the comparison is approximately made between the same points since there are no designs on the frontside of the wafer to guide the choice of the measured diameter. To ensure correct results, the wafer must be placed on three supporting balls on the chuck of the profilometer.

The next step is the measurement processing to retrieve the residual stress. Two methods have been used: one simply based on the maximum observed height in two consecutive measurements, the other based on the second derivative of a polynomial interpolating the difference between two consecutive measurements. The first method was used in laboratory for quick order-of-magnitude indications while the second required Matlab for processing the data but allowed for higher precision.

The Stoney formula used for the quick order-of-magnitude estimation is the following :

$$\sigma_f = \frac{E_s d_s^2}{6(1-\nu_s)d_f}\left(\frac{1}{R_{post}} - \frac{1}{R_{pre}}\right) \tag{5.1}$$

where the notation stands for:

- σ_f, the average residual stress in the film of interest after the manipulation,
- E_s, the Young modulus of the substrate,
- d_s, the thickness of the substrate,
- d_f, the thickness of the film of interest,
- ν_s, the Poisson coefficient of the substrate,
- R_{post}, the radius of the wafer after the manipulation,
- R_{pre}, the radius of the wafer before the manipulation

For rapid estimation, assuming the hypothesis $R \gg L$ is verified, the radius are approximated based on the maximal height of the curved wafer [36]:

$$R = \frac{\left(\frac{L}{2}\right)^2}{2h_{max}} \tag{5.2}$$

where, as in Figure 5.5 :

- R is the radius,
- L is the length of the measurement,
- h_{max} is the maximal deflection of the wafer

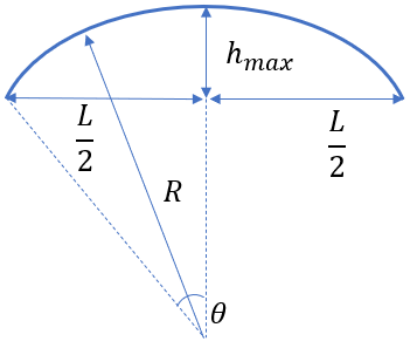

Figure 5.5: *Rapid evaluation of the radius [36]*

Using Matlab enables to access function such as polynomial fitting. Stoney formula is based on the difference in curvature before and after the executed step. Fitting a second order polynomial on the measurement means adapting its curvature to that of the wafer. With the same reasoning, fitting on the point-by-point delta between the two reference measurements gives a second order polynomial whose second order term corresponds to the curvature change. This is illustrated in Figure 5.6 for a silicon nitride layer.

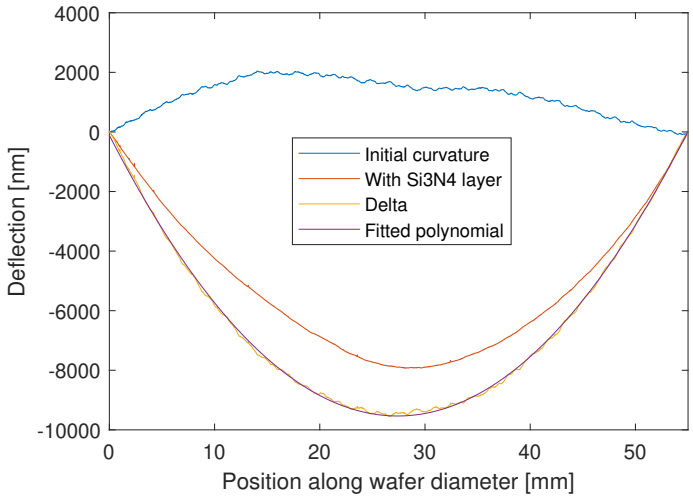

Figure 5.6: *Fitted polynomial process for the silicon nitride layer on sample WF4 from following process*

The version used for Matlab processing of the data is given here : 2004 Malhaire

$$\sigma_f = \frac{E_s d_s^2}{6(1-\nu_s)d_f}\frac{d^2P}{dx^2} \tag{5.3}$$

where, outside of previously given parameters :

- P is a polynomial function fitted by Matlab on the delta between measured points after and before manipulation,
- x is the axis along which the measurement was taken

The stress measurements made during the process are given in Table 5.3. In this table, both values using the curvature radius estimation and the fitted polynomial method are given for comparison. It can be seen that these values are very similar in most cases. However, for very large curvature changes, the curvature radius method seems to be overestimating and the fitted polynomial, underestimating. The value can be assessed to be in the range between the two given bounds. This can be seen in the post-thermal treatment results for the nitride layer in wafer 7 and 8.

5.3 Sectional view of the membranes and process sheet

This process is meant to test the fabrication of membranes and the two stacks of material that were the results of the simulation in section **??**. Process type A relies on using a wet thermal oxidation whereas process type B uses an SiO_2 PECVD deposition. These two process are meant to be compared regarding the residual stress in stack, their reproductibility and their complexity. The Table 5.2 gives the full process sheet for both type and Figure 5.7 gives a cross-sectional view of the device at each

step of its fabrication.

Step	Process step type	Type A	Type B
M0	Palmer	x	x
M1	Dektak 5500mm, 60s	x	x
1	Standard cleaning with HF bath	x	x
2	Wet Thermal Oxidation in Koyo 1 furnace	400 nm	-
3	SiO_2 deposition in PECVD Oxford chamber	-	700 nm
M2	Ellipsometer	x	x
4	Protective blue resist coating 3000rmp, bake at 120°C for 90s	x	-
5	Backside SiO_2 stripping in BHF bath	x	-
6	Protective resist stripping in Barrel (10 min from 200 to 500W)	x	-
M3	Dektak 5500mm, 60s	x	x
7	Stress annealing in Tempress furnace 800°C for 30min, 0.5L/s N2	-	x
M4	Dektak 5500mm, 60s	-	x
8	Si_3N_4 deposition in PECVD Oxford chamber	600nm	350nm
M5	Ellipsometer	x	x
M6	Dektak 5500nm, 60s	x	x
9	Stress increase in the Si_3N_4 layer 404°C	2x3min	15min
M7	Dektak 5500nm, 60s	x	x
10	Aluminium metalisation of backsides in VST	500nm	500nm
11	LPIII and backside AZMIR resist coating 4000rpm, 90°C 90s	x	x
12	Lithography with designed membrane mask 200W 2s	x	x
13	Lithography development and post-exposure bake 120°C 90s	x	x
M8	Lithography check on microscope	x	x
14	Aluminium etching in H3PO4, 2min 30s	x	x
15	Backside resist stripping in Barrel (10 min from 200 to 500W)	x	x
16	Frontside protective resist coating 3000rpm, bake at 130°C for 120s	x	x
17	Dicing	x	x
18	Die gluing on wafer	x	x
19	Deep RIE of Si layer in Oxford etching chamber	Full layer	Full layer
M9	Dektak measurement of the etched membrane	x	x
20	Release of the die in acetone	x	x

Table 5.2: *Process sheet*

5.4 Stack layers fabrication process and stress control

This section details the first steps of the process that focus on making the stack of material that compose the membranes and handling the residual stresses in each layer of material to eventually obtain the 50 MPa residual stress goal. During this process, the stacks have been fabricated using only PECVD, wet thermal oxidation and thermal treatment because of impossibility to use an LPCVD equipment. However, a different stack could be done using LPCVD deposited silicon nitride. This stack and potential process is detailled in Appendix A.

5.4.1 Wet thermal oxidation

The wet thermal oxidation was performed on wafers from process A, as refered in Table 5.3. It was done in the Koyo furnace. The aimed thickness was 400nm and the expected stress was 300MPa compressive, corresponding approximately to the nominal stress in such a stack.

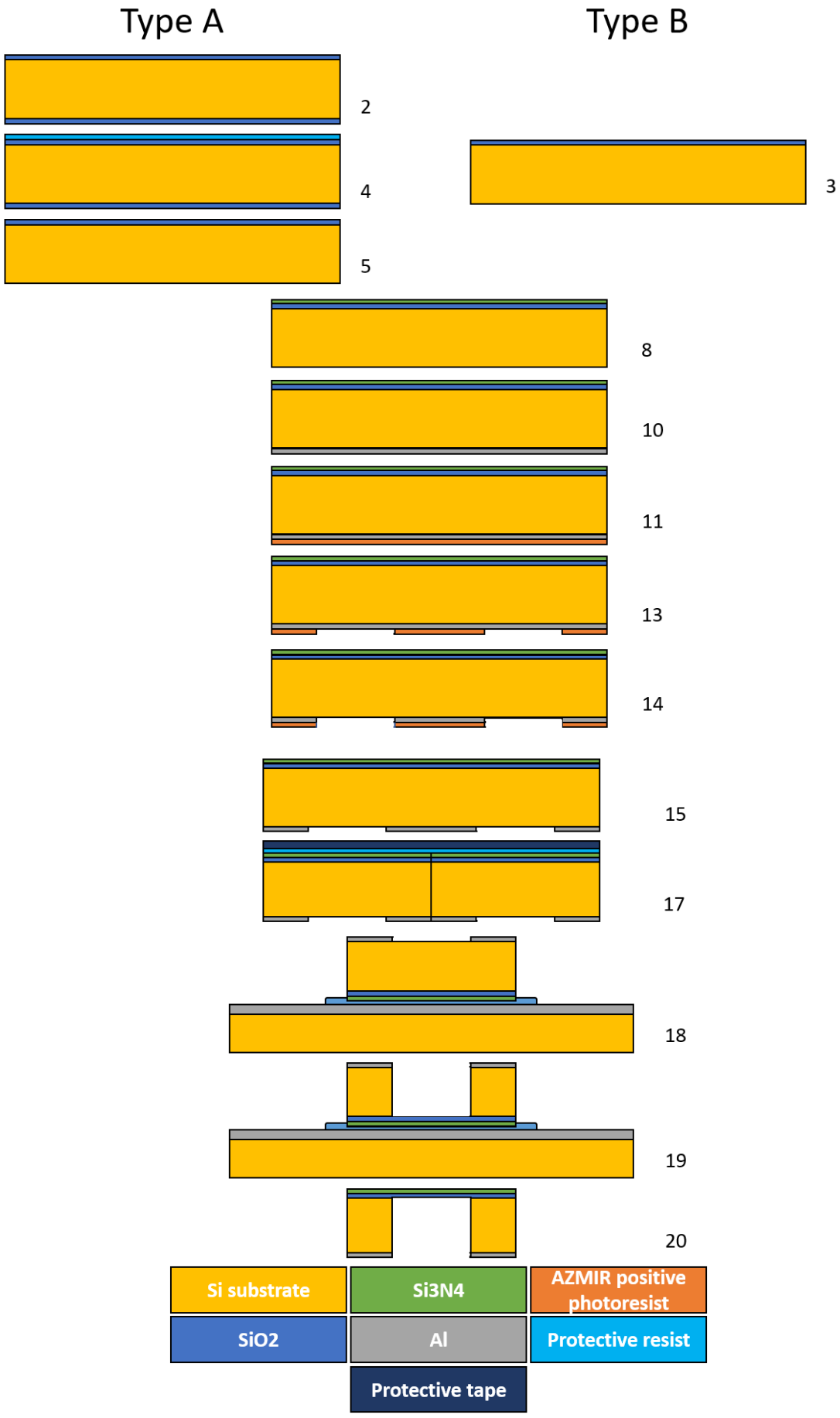

Figure 5.7: *Cross-sectional schematic view of the step by step process*

The results of this oxidation are presented in Table 5.3. The 402+/-2nm thickness corresponds to the expectations and the measured compressive stress of 300MPa after etching of the backside SiO_2 layer is also fully aligned.

5.4.2 PECVD silicon dioxide layer

Type B process relies on a PECVD silicon dioxide layer. Requirements were a 700nm-thickness and a stress of 300MPa after deposition in PECVD chamber of the Oxford, followed by an annealing in the Tempress furnace to reach 70MPa compressive stress. The results are reported in Table 5.3.

The deposited SiO_2 was obtained using the Oxford PECVD chamber. The parameters for the gas flows were 100 SiH4, 700 N2O and 1000 N2 at a pressure of 1 bar and a temperature of 300°C. To do the annealing, the wafers were placed in the Tempress furnace at 800°C for 30 minutes under a nitrogen (N2) flow of 0.5 L/s.

The obtained thickness was within a 10% margin, which was considered as acceptable. The measured stress before annealing is inline with the expectations, however the stress after annealing, measured at around 150MPa compressive, is twice higher than awaited.

5.4.3 PECVD silicon nitride layer

Both Type A and B processes required a PECVD silicon nitride (Si_3N_4) layer. The recipe used in the Oxford PECVD chamber was the following : 600 sccm SiH4, 21 sccm NH3, 700 sccm N2 at a pressure of 1 bar and a temperature of 300°C.

The results are given in Table 5.3. The thicknesses are correct to +/-10% but the measured residual stresses in the nitride layer are lower than expected, as the nominal residual stress for stochiometric nitride with this recipe is 300MPa tensile. The obtained 200MPa in average are below the expectations and does not comply with the requirements of the design. When the equivalent global stress for the full stack is computed, it falls in compressive range. The goal is to ensure a tensile residual stress and keep it around 50MPa.

In order to compensate for this difference, a thermal treatment has been used. The tests that were done to come up with the temperature that was used are detailed in Appendix 5.3. The Tempress furnace was used at 404°C, its minimal temperature. The wafers of Type B process were treated for 15 minutes resulting in a high tensile stress estimated around 800MPa tensile in the nitride layer. After thermal treatment, the equivalent stress in the full stack is around 170MPa. Type A wafers have been treated for 2 times 2'30". This allowed to increase slowly the stress to the awaited 290MPa and have a resulting stack global stress arround 40MPa. The exact values are given in Table 5.3.

5.5 Backside aluminium mask

The choice of a backside aluminium mask was made to ensure good results for the subsequent etching whatever the chosen technique between RIE, TMAH or XeF_2. When using RIE, a conductive layer is needed on the sample and aluminium can play this role, along with the good selectivity between aluminium and silicon during a SF_6 etching. If XeF_2 is used, the selectivity is good as well with an aluminium mask. Also, the aluminium mask has less risk to be etched by XeF_2 than a SiO_2 mask if some water was to be present in the chamber.

5.5.1 Aluminium backside layer

The thickness of the mask was fixed at 500nm as a trade-off between a thin mask that has a better precision of the etched pattern since the liquid aluminium etchant is isotropic, is quicker to deposit and a thick mask ensures that even with a non-zero selectivity towards aluminium, the mask would

Type	Wafer	Step	Exp. Thick. [nm]	Obt. Thick. [nm]	Measured Defl. [nm]	Meas. Film	Est. Stress [MPa]	Proc. Stress [MPa]
A	WF4	Initial measurement	-	387 [µm]	-1988	-	-	-
A	WF4	Wet Thermal Oxidation	400	401	-	SiO_2	-298	-287
A	WF4	PECVD Si_3N_4	600	564.5	7891	Si_3N_4	211	203
A	WF4	Backside SiO_2 etch	-	965.5	-2019	FS	-0.3	-0.6
A	WF4	Thermal treatment	-	965.5	3848	FS	73	67
A	WF5	Initial measurement	-	277[µm]	3399	-	-	-
A	WF5	Wet Thermal Oxidation	400	404.5	-	SiO_2	-230	-233
A	WF5	PECVD Si_3N_4	600	562.5	22 338	Si_3N_4	208	212
A	WF5	Backside SiO_2 etch	-	967	7276	FS	25	26
A	WF5	Thermal treatment	-	967	15 365	FS	76	73
A	WF6	Initial measurement	-	387[µm]	-1499	-	-	-
A	WF6	Wet Thermal Oxidation	400	402	-	SiO_2	-314	-306
A	WF6	PECVD Si_3N_4	600	578	8493	Si_3N_4	208	204
A	WF6	Backside SiO_2 etch	-	980	-1965	FS	-5.8	-4.5
A	WF6	Thermal treatment	-	980	4652	FS	76	72
B	WF7	Initial measurement	-	390 [µm]	-700	-	-	-
B	WF7	PECVD SiO_2	700	769	-	SiO_2	-286*	-294*
B	WF7	Thermal annealing	755	-	-8418	SiO_2	-123	-130
B	WF7	PECVD Si_3N_4	300	338.5	-3804	Si_3N_4	167	168
B	WF7	Thermal treatment	-	338.5	14 953	Si_3N_4	847	259
B	WF7	Thermal treatment	-	-	14 953	FS	173	168
B	WF8	Initial measurement	-	276 [µm]	-10 300	-	-	-
B	WF8	PECVD SiO_2	700	757	-	SiO_2	-286*	-294*
B	WF8	Thermal annealing	-	754	-2400	SiO_2	-111	-119
B	WF8	PECVD Si_3N_4	300	345.79	-14650	Si_3N_4	166	180
B	WF8	Thermal treatment	-	-	20 937	Si_3N_4	798	254
B	WF8	Thermal treatment	-	-	20 937	FS	174	172
B	WFT	Initial measurement	-	387 [µm]	-1135	-	-	-
B	WFT	PECVD SiO_2	700	855	21400	SiO_2	-286	-294
B	WFT	Thermal annealing	-	850	9300	SiO_2	-115	-121
B	WFT	PECVD Si_3N_4	300	418	4479	Si_3N_4	139	142
B	WFT	Thermal treatment	-	-	Broken	-	Broken	Broken

Table 5.3: *Stack layer thicknesses and residual stress measurements, values with asterix are extrapolated from another wafer of the same process*

not be completely etched but is longer and more difficult to deposit. The mask thickness by itself is not a critical parameter and it is hence chosen for simple practical considerations.

The backside aluminium layer has been deposited in the VST with a goal thickness of 500nm. The obtained thickness was 510nm.

5.5.2 Backside lithography with membrane mask

The aluminium mask is patterned by standard lithography. The first step is to coat the wafer with AZMIR positive resist on the backside. The pre-exposure bake was done at 90°C for 90s. The exposure parameters were 200W for 2s. The post-exposure bake (PEB) was then made for 90s as well at 120°C. The last step is development using AZ 726 MIF developper. The development is done with the standard procedure.

5.5.3 Aluminium backside mask realisation

Once the development was done, the aluminium layer is etched to transfer the pattern from the resist mask to the aluminium. This is done using a H3PO4:IPA 5:2 solution bath at a temperature between 55 and 65 °C. Depending on the surface to etch, the etching is stopped 15 seconds after the dispersion of the bubbles in patterns to etch. This duration is chosen to ensure that all residues in pattern can be etched and prevent overetching at the same time.

The quality patterns can the be controlled to verify the quality of the etching of the mask, these are shown in Figure 5.8. It can be seen that the quality patterns are well defined for thin standing structures if bigger than 1µm and thin etched gaps larger than 2µm are well defined. Thinner aluminium lines are lifted off because of overetching. Since the membranes are large compared to these patterns, the quality is considered good enough to guaranty the edge to be sufficiently straight. On the rough backside, the 3, 4 and 5µm structures are well defined. The same conclusion is drawn from this.

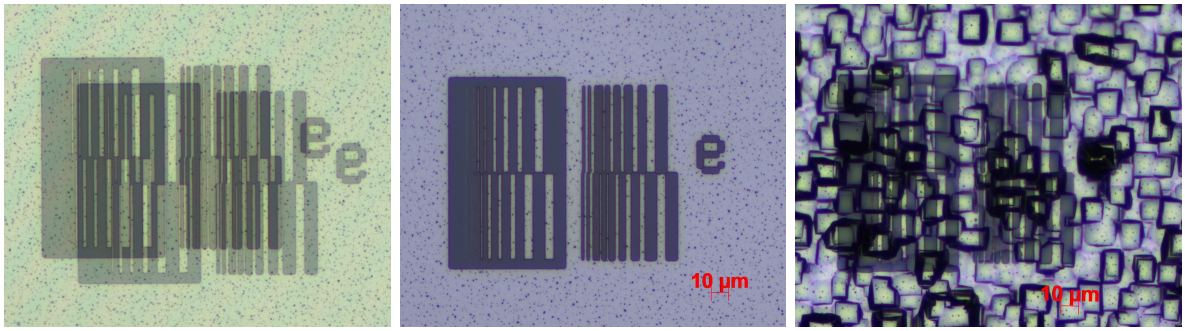

Figure 5.8: *Quality patterns a) resist and aluminium mask, b) results of the etching of the polished backside, c) results of etching on a rough backside*

5.6 Etching of the membranes

In order to allow for testing and ensure a maximal yield in this process, etching is done die per die. This advantages the yield since the end of the etching can be adapted to each membrane size as their aspect ratios varies.

5.6.1 Dicing of the wafers

First step before etching is to dice the wafer. To protect the membrane layer, a protective blue resist coating is applied to the front side of the wafer and the full wafer is covered with a blue tape to keep

the dies together once diced. Dicing is then done using a diamond tip and water for cooling. Once diced, the dies are carefully removed from the blue tape and washed in acetone, isopropanol and DI water before any other step to remove residues and resist.

5.6.2 Dies preparation for etching

To prepare a die for etching, it is first glued on a substrate to ease manipulation. This is done with the following steps :

- dropping a drop of blue resist on the substrate,
- placing the die on the droplet,
- placing it in a vacuum chamber and cycle three times from atmospheric pressure to remove air bubbles,
- baking at 130°C for 120 seconds twice

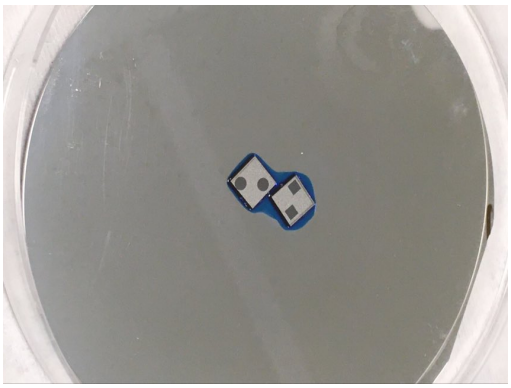

Figure 5.9: *Dies ready for etching, glued with resist on an aluminium-coated substrate*

The result is presented is Figure 5.9. The substrate used is a standard silicon wafer coated with at least 500nm of aluminium. Using an aluminium covered wafer limits the etching of the substrate itself.

5.6.3 Deep RIE of membranes

The used wafers are around 280µm or 380µm in thickness. The release of the membranes structures is performed using deep RIE in order to maintain the form of the membrane since TMAH does not preserve the form of the circular membranes and XeF_2 rounds out the square membranes. The machine used is the etching chamber of the Oxford Plasmalab System 100.

In order to control the etching speed, the formation of grass and the end of the etching, the etching is done 100 cycles per 100 cycles. For the last two rounds the number of cycles is adapted to limit overetching and avoid damaging the stop layer of SiO_2.

The formation of grass is very dependent of the surface condition of the backside of the wafer : double polished wafer develop less grass than standard wafers. This grass development can be attenuated by an additional isotropic etch step that is adapted to the wafer type : 1 second for the double polished wafers and 14 second, the equivalent of an additional etch step, for the standard wafers. This step is kept as short as possible to limit the loss of precision linked to isotropic etching.

The recipe used for RIE is given in Table 5.4. This recipe etches 1 to 1.2 µm per cycle. The temperature was fixed to -10°C on the chiller of the machine, pressure is 10 mTorr and the power used for the plasma is 1000W for the ICP plasma and 30W for the RF one. These parameters ensures that the chamber does not heat too much.

The results of the RIE etching gives wall slopes of about 2.86 degrees which results in the membranes to be larger by 10µm for 100µm thickness of the die : around 30µm for the double polished 280µm-thick one and around 40µm for 380µm-thick standard wafers. The isotropic etches cause around 1µm enlargement of the membranes per use of a 14 second one, so 1µm per round. This isotropic etch is clearly visible in Figure 5.10 taken using the SEM.

Step	Time [s]	SF_6 [sccm]	C_4F_8 [sccm]	Utility
Isotropic etch	1 or 14	120	0	Reducing the grass (double polished or standard wafer)
Deposition step	10	0	140	RIE loop passivation
Etch step	14	120	0	RIE loop etching

Table 5.4: *Bosh process recipe*

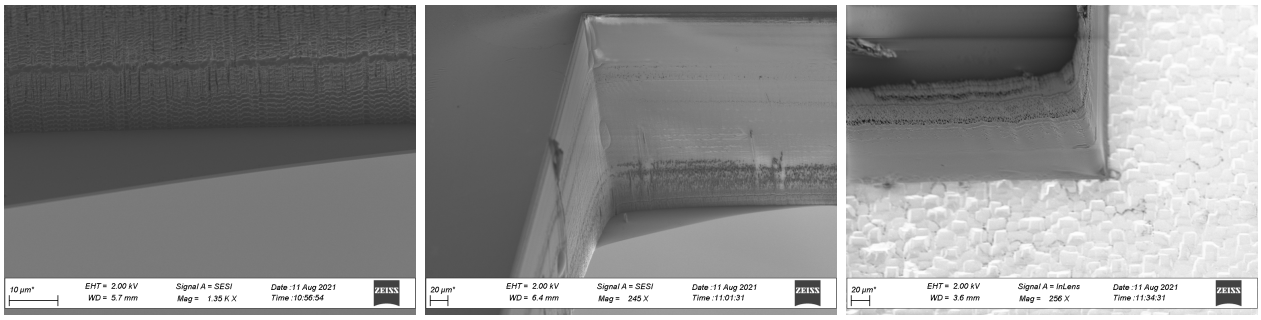

Figure 5.10: *Pictures taken in SEM showing a) the trench caused by an isotropic etch step, b) results on double polished wafer with 1" isotropic etch steps and c) results on standard wafers with 14" isotropic etch steps*

The variation in thickness from one wafer to another and in surface to etch as well as in aspect ratio causes variation in the number of cycles. The Table 5.7 gives the number of cycles for each set of dies that was etched.

5.6.4 Die release from support wafer

The die releases are done using acetone and avoiding ultrasounds to accelerate the release to avoid damaging the membranes. A light manual shake or a 50°C heating have been used in some case to shorten the release time.

Once the dies are released, they are simply taken out of acetone carefully and left to dry on absorbing layer with the membrane facing upwards. This choice was made to avoid any possible damage to the membrane that could occur during the rinsing. The bigger membranes are particularly at risk of breaking during release and even more during a rinse off. The main consequence of this is that it can leave some residues of resist on the membrane. However, since it is the last step of processing and has no real impact on the nature of the stack, it is preferred to a very high risk of breaking the membranes.

5.7 Grinding dies to reduce the impacts of etching non-idealities

Dies are grinded in this process to determine the impact of different parameters : the loss of precision between mask and membrane due to the angle of the slopes of the etching, the thickness of the substrate, the impact of several surface quality of the backside on the precision of the mask and the etching.

The process sheet for grinded dies begin at step 18 since the dies need to be diced already to avoid using a full wafer. This choice was made to be able to have grinded equivalent membranes for each stack since the residual stresses vary from one stack to another even in a same batch. The adaptation of the process sheet to this alternative process is given in Table 5.6. Having two process types enabled testing two alternatives for the coating and lithography steps on these grinded dies.

The grinding step is done using the GN MPS 2R 300S Grinder. To prepare the dies, they must be glued on support wafers so that these can be secured on the chucks of the grinder. This is done with blue resist and two bakes at 130°C for 120s. They are glued on backside of standard wafers to increase

adhesion and once in place, the frontside of the support wafer is covered with protective yellow tape. This tape helps evening out the grinding since it is softer than silicon and can thus absorb part of the vibrations. The wafers are then placed in the grinder, secured on the chuck with vacuum and the grinder is programmed to etch them down to 150μm thick at 10μm/min. After hitting the 150μm mark, it slows down to 1μm per minute and completes the etching down to 100μm. The results are presented in Table 5.5.

Batch	Wafer	Initial number of dies	Final number of dies	Destination
1	WF7	7	6	2 used in process
	WF8	7	5	2 used in process
2	WF4	7	2	unusable
	WF5	7	2	unusable
	WF6	4	3	unusable
3	WF4	5	4	3 used, 1 broken in coating
	WF5	5	5	1 used in process
	WF6	5	5	1 used in process, 2 broken in coating

Table 5.5: *Grinded dies*

After the grinding comes the metalisation of the backsides of the dies. This is done directly on the same support wafer as for grinding for the process type A whereas the dies from process type B are placed on the wafer that will be the support for lithography and etching afterwards. Every manipulation of the dies alone is risky since they are very thin so their number is reduced as much as possible.

Step	Process step type	Type A	Type B
18b	Die gluing on wafer	x	x
19b	Grinding 10µm/min and last 50µm at 1µm/min	100µm	100µm
20b	Release of the dies in acetone	-	x
21b	Die gluing on wafer	-	x
22b	VST aluminium deposition	500nm	500nm
23b	Release of the dies in acetone	x	-
24b	Kapton tape covering of the die	-	x
25b	Protective resist coating, spin coat 3000rpm	x	x
26b	Kapton tape removing	-	x
27b	Die gluing on wafer	x	-
28b	Positive resist coating of the die, spinning 300 rpm	x	x
29b	Lithography with membrane mask	x	x
30b	Lithography development and post-exposure bake 120°C 90s	x	x
M9b	Lithography check on microscope	x	x
31b	Aluminium etching in H3PO4	x	x
32b	Deep RIE of Si layer in Oxford etching chamber	Full layer	Full layer
M10b	Dektak measurement of the etched membrane	x	x
33b	Release of the dies in acetone	x	x

Table 5.6: *Adaptation of the process sheet for grinded dies*

Process type A involves grinding the dies and then directly metalise these on the same substrate that was used for grinding. Once done, the dies are released from the substrate. This requires to cut the aluminium layer around the die to expose the resist manually with an exacter knive. Next, they are simply released in a standard acetone bath, avoiding the ultrasound treatment since the grinded dies are much more fragile than standard dies. Once released, they are placed on a Si substrate with an 500nm Al-layer covered with blue resist using a classical spin coating before a hard bake of the

assemblage. Once the bake is done, AZMIR positive resist can be spread manually on the die only before being spincoated to remove any excess. This process allows to only do the lithography on the die.

For process type B, the dies are glued on the substrate with blue resist and then metalised in the VST with a 500nm thick layer of aluminium. The die is then protected using a piece of Kapton tape for the blue resist protective coating of the substrate. In this case, blue resist is also spin coated on the full wafer and bake afterwards. Once this is done, the Kapton tape is removed and some positive AZMIR resist can be applied on the die manually and spun to remove the excess.

In order to perform a lithography on a grinded die glued on a substrate with resin, the lithography technique was adapted. To allow for a good placement of the wafer and pre-alignment with the mask, 3inch wafers are placed on a 4inch support plate. The vacuum is also better to keep the substrate clamped to its support in these conditions. Once the wafer is approximately aligned with the mask, it can be placed in the machine. Next, the first alignment in machine is done visually again and a check and some correction are then applied using the camera and the microscope. The parameters of the alignment and exposure are adapted with a gap (alignment gap and exposure gap respectively) corresponding to approximately the thickness of the die. In this case, 100μm is estimated to be close enough to minimise the impact of such a gap on the quality of the exposure while avoiding to get the die stuck on the mask by the positive photoresist.

The development is performed manually using a AZ 726 MIF developer bath for 90 s followed by a 5 min rinse off in DI water. The wafers are then left to dry before etching steps. The results are shown in Figure 5.12. It can be seen that, due to the exposure gap, the exposure is less clean than with a classical lithography on a wafer. The pattern is larger, as measured in Figure 5.12 a, and the corners are rounded due to the diffraction of light through the mask. Diffraction causes variations in the exposure doses of the borders of the pattern resulting in imperfect development as seen in Figure 5.12 b.

Next step is the etching of the aluminium maks, which is the same as presented in section 5.5.3. The resulting mask is here dependent on the quality of the resist pattern. Results of the irregularities in this pattern are showed in Figure 5.13 which compares before and after aluminium etching and shows the results seen in SEM imaging after RIE. The irregular borders of the resist pattern are transfered on the aluminium mask causing irregular borders in the RIE process.

The etching process is slightly adapted to the grinded dies. The recipe used is the same as for the dies from standard wafers : an isotropic etch of 14 seconds before the RIE cycles as stated in Table 5.4. The number of cycles per round is changed according to the thickness of the grinded dies. First round is 50 cycles. The next round of cycles is adapted based on a Dektak measurement of the results after the first round to avoid overetching.

5.8 Results of the fabrication process

The samples resulting from the process are listed in Table 5.7 for the type A process and Table 5.8 for the type B process. It can be observed that some membranes were lost due to various causes among which the residual stresses being to high, overetching and die handling during the release in acetone. However, most the membranes of the type A process made it through whereas none of the process type B were usable in the end.

The type B process presents higher residual stress in the silicon nitride layer due to the longer thermal treatment it underwent to increase the stress in this layer. This thermal treatment was then corrected for the type A process. It turns out that such a high average stress value results in the layer being very fragile because the stress value is an average. This means some higher local stresses can emerge and cause its breaking once it is released from the silicon substrate. Such broken membranes are shown in

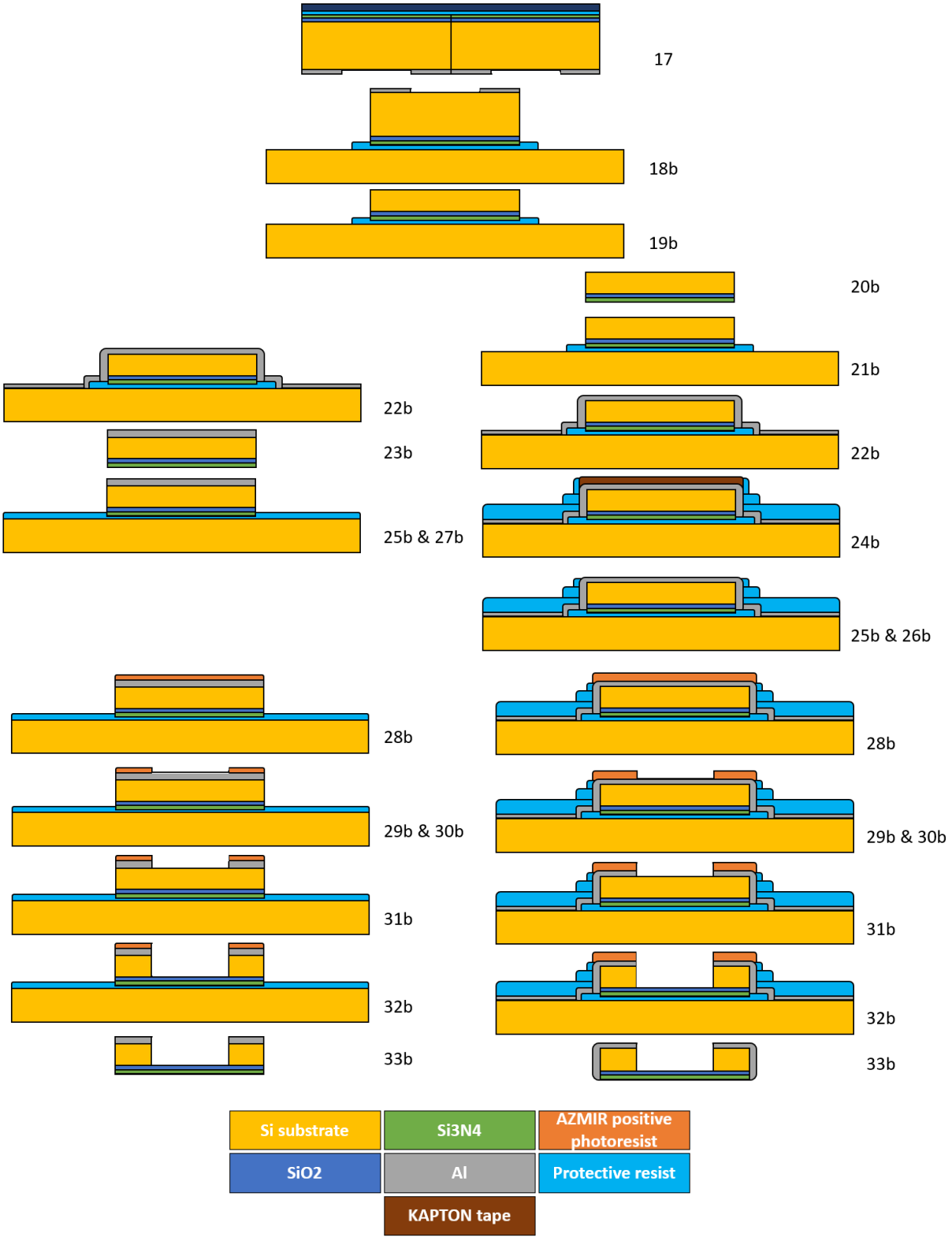

Figure 5.11: *Coating process for a) type A process and b) type B process*

Figure 5.14. Both normal and grinded dies were etched but the impossibility to get any membrane out of this process. After several tries, it was decided to stop using these dies and focus on type A stack for the etching of the membranes. Further investigation and a better knowledge of the stress in the film could help to solve the issue.

Regarding the grinded dies, the results are not as ideal as expected. The non-idealities due to etching : the impact of the slope of the walls, the loss of precision in form during etching, the height of residual

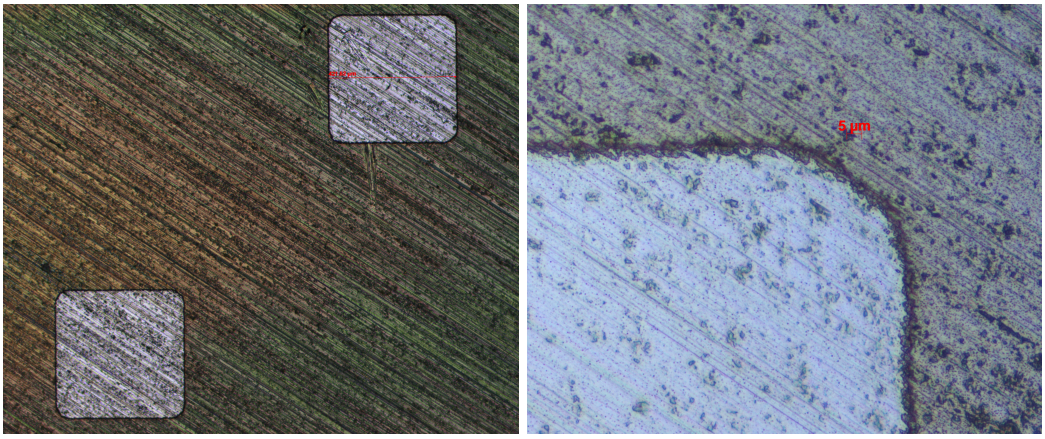

Figure 5.12: *400 µm membrane pattern on a grinded die a) general result and diffraction effects and b) imperfections : rounded corners and irregular borders*

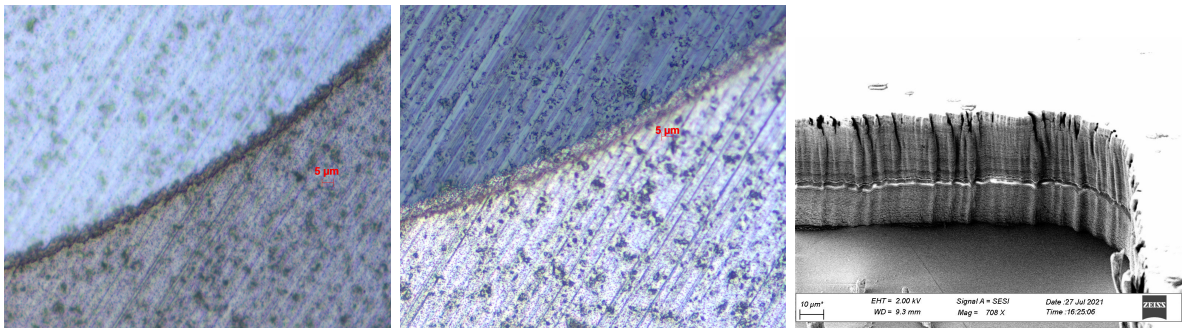

Figure 5.13: *Comparison between a) before and b) after etching of the aluminium mask in a 950 µm ciruclar pattern on grinded die, c) SEM imaging after RIE etching of a 400µm pattern on grinded die, the imperfections of the aluminum mask are visible in the top layer*

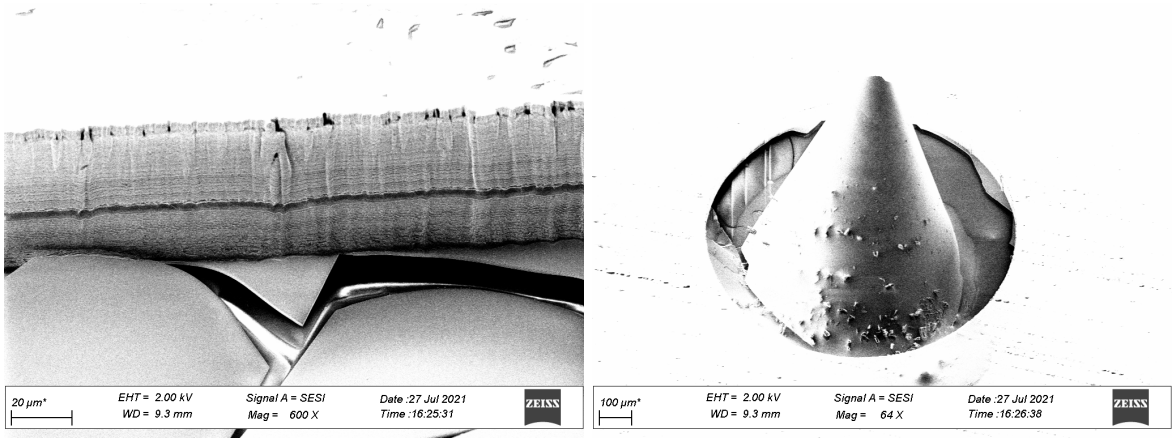

Figure 5.14: *Broken membrane from wafer 7 a) crack in the film and b) rolling up of the film under the residual stresses in it*

grass, the need for isotropic etch steps etc. are reduced. However, other non-idealities arise due to the lithography process that requires an exposure gap and a manual development. These non-linearities limit the benefits of grinding the dies when it comes to improving the shape of the membranes. Moreover, grinding the dies makes the dies potentially difficult to manipulate and adds numerous steps to the process. Steps such as the gluing on support wafers with spin coated protective blue resist and the coating with AZMIR positive resist are highly failure-prone. The solvent present in the AZMIR resist can dissolve the blue resist used to glue the die and cause it to come off the support wafer during spinning or baking.

Wafer	Die set	Number of RIE cycles	Number of rounds	Usable membranes after release
WF4	1600 x1 - 1850 x1	380	5	0 (overetching)
WF4	1600 x1 - 1850 x1 bis	400+ (grass)	4	0 (shattered in Barrel)
WF4	1200 x1 - 1350 x1	370	6	1200 x1, 1350 x1 (others lost in acetone)
WF4	800 - 950 x2	362	6	800 x3, 950 x3 (others lost in acetone)
WF4	400 - 600 x2	360	5	400 x7, 600x7 (others lost in acetone)
WF4 Grinded	1600 x1	90	2	1600 x1
WF4 Grinded	1200 x1	-	-	die lost during lithography steps
WF4 Grinded	800 - 950 x1	100	3	800x1, 950x1
WF4 Grinded	400 - 600 x1			
WF5	1600 x1 - 1850 x1	253	4	1600 x1
WF5	1600 x1 - 1850 x1 bis	280	4	1600 x1, 1850 x1
WF5	1200 x1 - 1350 x1	253	4	1350 x1 (others lost in acetone)
WF5	1200 x1 - 1350 x1 bis	293	5	1350 x2 (others lost in acetone)
WF5	800 - 950 x2	245	5	800x3, 950 x3 (others lost in acetone)
WF5	400 - 600 x2	265	4	400 x8, 600x8
WF5 Grinded	800-950 x1			0
WF6	1600 x1 - 1850 x1	360	4	1600 1850
WF6	1200 x1 - 1350 x1	390	5	0 (all lost to overetching)
WF6	1200 x1 - 1350 x1 bis			1200 x2, 1350 x2
WF6	800 - 950 x2	353	5	800x3, 950x3
WF6	400 - 600 x2	400	5	400x8, 950x8
WF6 Grinded	800 - 950 x1	110	3	800 x2, 950 x1

Table 5.7: *Results of the type A process*

All these reasons make the process substantially more complicated, time-consuming and costly for a limited benefit in the precision of the large patterns this process uses. Since the etching non-idealities can be reduced, it could help with more intricate patterns such as islands but solutions need to be found regarding the lithography process.

Wafer	Die set	Number of RIE cycles	Number of rounds	Usable membranes after release
WF8	1200 - 1350	240	3	0 (residual stress)
WF7 Grinded	1200 x1			0 (residual stress)
WF7 Grinded	400 - 600 x1	90	2	0 (overetching)
WF7 Grinded	800 - 950 x1	90	2	0 (residual stress)

Table 5.8: *Results of the type B process*

6 Measurements methods

This section covers the methodology used to characterize the membranes produced as in previous chapter. First part covers the types of measurements that were taken. Next sections respectively describe the sample preparation and the setups that are put in place. After the installation of the setup, the procedures and chosen settings are explained.

6.1 Taken measurements

In order to characterize the membranes for their resonant aspect, several measurements were taken : width of the membranes at the end of fabrication, topography and finally vibrometric measurement.

The width of the final membranes was measured to examine the deviation of this parameter regarding the initial expected width. It will enable comparison to a more accurate model of the membrane to discuss the results. These measurement are taken using the Zeiss Axio Imager .A2 Vario microscope in Winfab.

The topography of the membranes is realized using the Polytec MSA-500 Micro System Analyzer probe station. It uses the interferometric topography. This measurement enables to evaluate the curvature of the membranes and then assess if the residual stress in the film is tensile or if its compressive. Tensile films give flat membranes whereas compressive ones provoke buckling.

Last but not least, laser vibrometry is performed in order to evaluate the eigenfrequencies of the produced membranes and their full frequency response. The Polytec MSA-500 Micro System Analyzer also allows to take these measurements.

6.1.1 Principles behind white light interferometry for topology scanning

White light interferometry is a technique used for determining the height and surface of an element. It is based on the Michelson interferometer.

A Michelson white light interferometer works as follows : a white light source produces a beam that is directed towards a semi-transparent mirror called "beam splitter". The main beam is separated in one reflected beam toward mirror M1 and one transmitted beam towards mirror M2. The difference between the path to M1 and the path to M2 can then be seen in the interference between the two beams reflected on these mirors and going back to the observation point. These interferences produce fringes and their distance from one another is an image of the difference in distance of the two mirrors to the beam splitter. [42] This principle is illustrated in Figure 6.1 a.

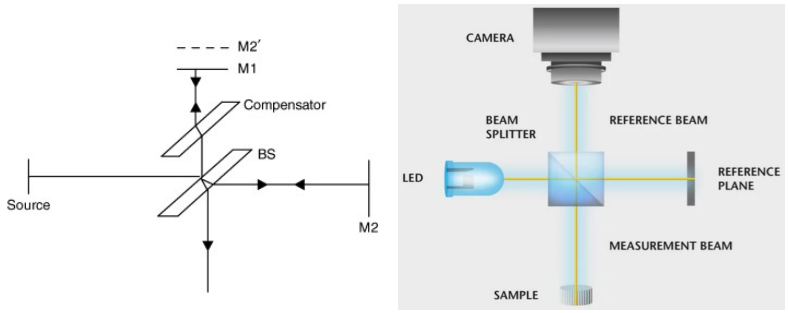

Figure 6.1: *Michelson interferometers a) general case [42] and b) Polytec configuration [43]*

The Polytec White-light interferometer is a specific case of a Michelson interferometer. The topology measurement of the surface is done placing a camera at the watcher place and an object that is reflective enough at the place of the M1 mirror. The surface of the sample is then scanned by moving the M2 mirror which is here called the reference plane. The fringes will form where the distance between the sample and the beam-splitter is the same as the one between M2 and the beam-splitter. This is then monitored by the camera and post-processed to give the topology of the surface of the examined object. [43] This configuration is represented in Figure 6.1 b.

6.1.2 Basics of the laser-Doppler vibrometry

The base principle of the laser-Doppler vibrometery is to read the movement of the sample from the variation is causes in the reflection of a laser beam pointed on it.

This is performed using an interferometer to compare a reference beam to its reflection on the sample. The sample reflects the incident reference beam back to the mirror that sent it. However, as the sample moves, the phase and frequency of the back scattered beam change along which is due to the Doppler effect. This modified beam is superposed to the reference one inside the interferometer and modulates the signal. This signal is then read by a photodetector and post-processed to display the movement of the sample. To discriminate between a positive and a negative displacement, a pre-shift, here applied by the Bragg cell, can be added to the reference beam hitting the sample. The information contained in the back scaterred beam is now read relatively to an expected frequency shift and provides thus information on the movement direction. [44, 45] The principle is illustrated in Figure 6.2.

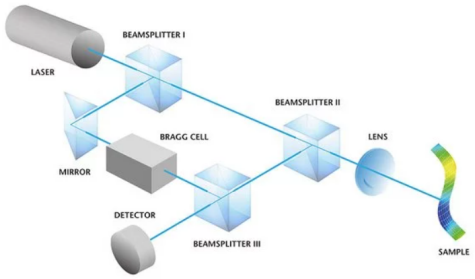

Figure 6.2: *Illustration of the principle of laser-Doppler vibrometry [45]*

In the Polytec, this measure is performed on each point of a defined mesh for a given signal of actuation of the test object. The combination of all these points allow to reconstruct the displacement and velocity of the whole sample visible structure.

6.2 Sample preparation

The membranes are actuated by a piezoelectric disc that vibrates under the signal sent by the Polytec. This piezoelectric disc is wired to the machine by soldered wire to either faces of the disc. This disc is glued on a plate that gets secured to the adjustable support of the Polytec set up.

The disc is prepared first. It is glued on a plate and wires are added on its conductive surfaces for actuation. The same Epotec conductive glue is used for all of these operations. Next, the assembly is placed in an stove at 120°C for at least 10 hours for the Epotec to cure.

Once the disc is ready, the membranes can be fastened to the disc with different glues. This choice was a trade-off between some advantages and inconveniences of each possibility :

- Epotec glue : This conductive glue is normally used for soldering and gluing together elements. The Epotec glue requires curing at 120°C for several hours before use. It can be removed using simmering water.
  In this case it is used for the soldering of the wires to the disc and was also tried for gluing the dies with the membranes. However, the later usage levered some inconvenience for the sample measurements of this project : it was difficult to ensure the full die had enough adhesion to the piezoelectric disc and that the glue would not damage the membrane at the same time since it is thick and requires to apply some pressure on the die to create adhesion. The choice of this glue was discarded after some testing on dies from other projects.

- Pattex Mini Trio : This glue is more liquid than the Epotec, so that less pressure is needed to be applied on the die, it allows to ensure good fastening of the dies to the disc and there is no need for curing. Main inconveniences of this glue are that it can be stripped with acetone but it is a slow process and its low viscosity generates more capillarity. This means that if too much glue is applied it can end up touching the membrane.
  This was used for gluing the dies of most samples.

- Resist : Replacing the glue with some resist allows to ensure good fastening, fast curing of 2 minutes at 130°C and easy stripping in acetone. This was used in order to allow to strip the gluing layer to allow for reprocessing of the membranes. Main problem of this technique is the uncertain behaviour of the resist during and shortly after the curing. First hypothesis is that the resist can degas and cause pressure on the membrane. Second is that the curing can be incomplete and cause stresses or deformation that could slowly release themselves as the resist can still move.
  This was used for the samples of wafers 4 in set B.

Different plates were also used : a metal one and glass ones. These were selected to support the curing of the glue to fasten the disc on the plate and the wire to the disc with Epotec.

The Table 6.1 gives the exact sample preparation for each membrane set. The sample are illustrated in Figure 6.3.

Sample serie	Set composition	Plate	Glue	Curing
A : WF5	1600 x1, (1350 x1), 800 x2, 950 x2, 400 x, 600 x	metal	Pattex	-
B: WF4	1200 x1, 1350 x1, 800 x, 950 x, 400 x, 600 x	glass	Blue resist	120°C for 3min
C: WF6	1850x1, 1350x1	glass	Pattex	-
D: WF5 & WF6	1850x1, 1350x2 1600x1, 1200x2	glass	Pattex	-
E: WF4G & WF6G	1600x1, 950x1, 600x2, 400x2 800x1, 950x1	glass	Pattex	-

Table 6.1: *Sets of samples*

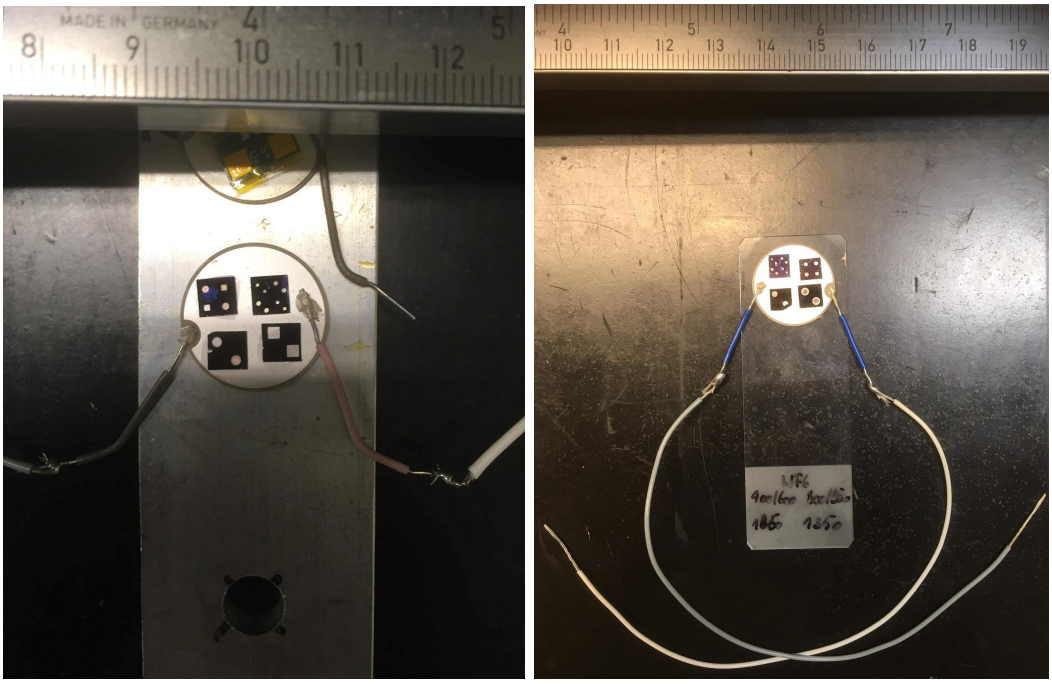

Figure 6.3: *Samples on a) metal and b) glass plates*

6.3 Measurement setups

This section describes the set-ups that were put in place for the measurements in the Welcome laboratory facilities. Both use the Polytec MSA-500 Micro System Analyzer measurement set up.

6.3.1 Set-up for topography determination

To make a topographic measurement, an interferometric set up is used. It is put in place using the Polytec MSA-500 Micro System Analyzer microscope with its laser, an interferometric lens and a goniometer. The full set up ready for measurement is displayed in Figure 6.4.

The chosen interferometric lens has a x2.5 zoom. This lens is fixed on the microscope and set on the interferometric mode.

Under the microscope, the samples are placed on the goniometer. This helps to orient the samples in order for the dies to be as flat as possible. Each die can have a different inclination since the glue layer can vary from die to die so this part of the setup must be adapted before each measurement. The die is considered flat enough when the fringes of the diffracted beam can be seen distinctively. The difference between fringes that are too close versus fringes that are correctly placed is displayed in Figure 6.5.

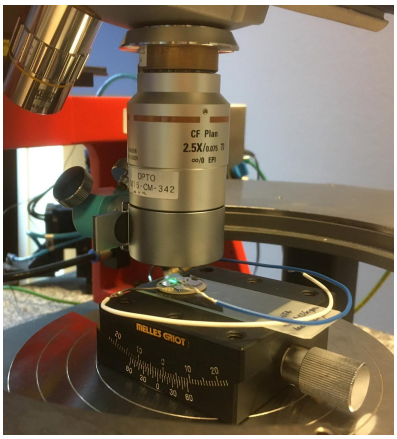

Figure 6.4: *Set up for topology measurements of the membranes*

6.3.2 Polytec setup for a vibrometric measurement

Once ready the samples are placed and secured on the Polytec set up. Tape is used to fasten the samples on the chuck. This prevents the vibrations induced in the piezoelectric disc from making the sample move out of camera sight or focus.

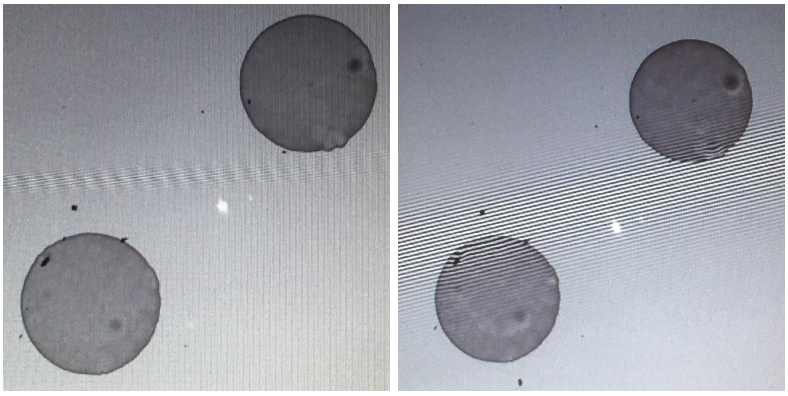

Figure 6.5: *Adjustment of the angle of the goniometer a) before : fringes can not be distinguished, b) after : fringes are well spread*

The right objective is chosen for laser-Doppler vibrometry and placed on the microscope. The zoom can be chosen to be adapted to the membrane size. The larger one can be handeled with a x5 zoom and the smaller ones with a x10 zoom.

The wires of the piezoelectric disc are wired to the Polytec vibrator auxiliary using cables with probe or crocodile ends. Securing the cable to the platform around the measuring area is needed to avoid pulling on the wires and damaging these or the soldering to the piezoelectric disc. Additional length of flexible cable can be soldered to the small wires to reduce the stress put on the soldering even more. The generator and the velocity analyser must then be switched on as well as the laser and the microscope. This set up is visible in Figure 6.6.

Last comes the positioning of the membrane to measure and the laser : the membrane is placed so that it is centred on the display of the microscope, the focus is set on the membrane and the reference laser beam can then be moved to reach a point near the edge of the membrane but clearly on the die. The goal of this reference beam is to offset the movement of the die and the supporting disc.

6.4 Topology of membranes

Topology measurement of the membranes is used to determine the curvature of the membranes. These measurement are taken with the Polytec white light interferometry system and associated program. This section describes the procedure for taking a topographic image of the samble once the setup is in place and the post-processing that is done to extract the final image.

6.4.1 Procedure for topology scanning

Once the goniometer is well adjusted, the Polytec's topography measurement system (TMS) software can be set up. In the measurement settings window, the right zoom must be indicated. The precision is also chosen here. The more precise the measurement, the longer the scanning.

The region of interest is defined arround the membrane to measure. A sufficient amount of die space must be included in the measured region. This is used in post-processing to level out the measurement. To visualise better the region, contrast enhancement can be used.

Next, the start and end points of the scan can be determined. To do this, the measurement position is set to zero and focus is changed to have the fringes centered in the region of interest. The fringes are then moved using the software to actuate the mirror in the interferometer. Once the fringes are just out of the region of interest, the displacement of the mirror can be stopped and the setting can

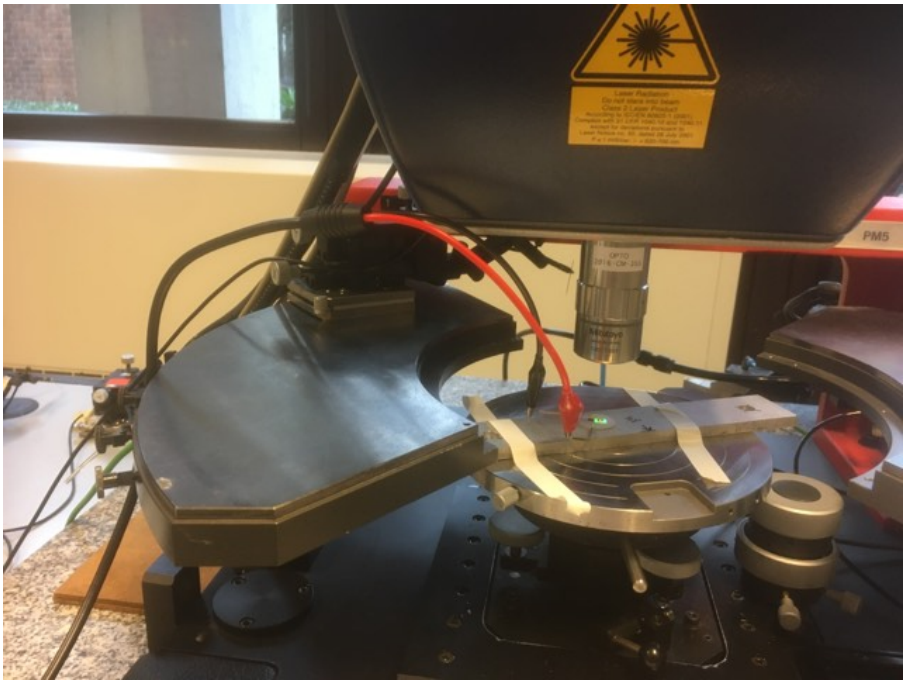

Figure 6.6: *Polytec Set up for vibrometric measurement: here the cable has crocodile ends and is fastened to the edge of the chuck, the metal plate secured to the platform, the piezoelectric disc glued on the plate, the zoom and the laser are adjusted above the sample.*

be saved as either start or end point. At this moment, configurations can be added for redundancy in the measurement.

Lasts settings determine the exposures and threshold for the measurement. The highlight pixel let the user to visualise the pixels that can be measured or are over ranged. The exposure and threshold can be defined individually for each of the configurations. To chose these settings, the intensity of reflection display is used. In order for the object to be measurable, the reflection intensity must range between the 100 and 200 limits indicated on the graph. This can be changed by varying the exposure time and the threshold. Last step is simply to start the scan.

6.4.2 Post-processing and artefacts

Once the measurement is taken, the data must be post-processed to obtain the final image. The first step is to level out the measurement. To reach this goal, a linear regression filter is applied on regions that are on the die, outside the membrane. This is based on the hypothesis that the die is sufficiently flat.

First, some masks boundaries are placed on the die surface in the scanned region. Next, the region outside the delimited spaces is masked and the linear regression filter is applied. The masked region is then unmasked. This levels the die surface out. Last, the automatic range box is unticked and the boundaries are adapted to the new levelled measurement to have a clear measurement of the membrane. Some defects can be left out of range for more readability.

Last, a filter can be applied to reduce the impact of artefacts and interferences. In this project, either an averaging filter on 5 to 10 points was used or a Gaussian low-pass filter are applied to the measurement.

To analyse the measurement, the obtained profile is compared with the reflexion intensity chart. Since this measurement technique depends partially on the reflectivity of the structure that is examined, a brutal change in it can generate artefacts.

6.5 Vibrometric measurement

The vibrometric measurement was done using the Polytec and more specifically the Polytec Scanning Vibrometer (PSV) software. This program is named PSV measurement. The next sections describes how measurements are taken and how the parameters are chosen.

6.5.1 Procedure for measurement taking

Once the setup is in place, the measurement is taken using the laser and the vibrometer of the Polytec and comparing the data coming from the scanning beam to the ones from the reference beam to extract the movement of the membrane.

First step to a scan of a membrane is to verify the alignment of the reference beam. To ensure correct processing of the data, the 2D alignment feature enables to position reference points. Here it was chosen to work with five points, one at each corner of the membrane if square or the inscribed square if circular and one at the centre. The 3D alignment is ignored in this case as displacement are extremely small.

Upon taking the actual measurement, a virtual mesh needs to be fitted on the membrane to determine the points that will be measured during the take. The mesh should be fitted on the membrane and can be sized and oriented to ensure full coverage. This is, however, easier done for a square membrane if it is aligned with the microscope camera. The size of each step in the mesh can also be adjusted with a trade-off between precision and number of points on one side and duration of the scan on the other.

Next step is to determine the A/D characteristics of the measurement and the generated signal that will actuate the piezoelectric disc: the bandwidth, the number of FFT lines for precision, measurement type for velocity and displacement, waveform, waiting time between signals, amplitude, offset, limits of the output voltage and enabling or not of amplification.

Last, the generator is set to active and the scan can occur.

6.5.2 Settings choices

This section explains the choice of parameters for the A/D characteristics of the scans in this project. It covers the bandwidth of the measurement and filtering of the received signal but also the type of signal that is sent to the piezoelectric disc for actuation.

The frequency bandwidth and the fft lines define together how many frequencies will be measured. In this work, the frequency bandwidth was taken as 1kHz up to 1MHz in order to cover the region of the expected first mode frequencies. The number of fft lines was pushed to the maximum for precision: 12800.

The actuation signal is chosen to be a periodic chirp to explore a wide range of frequencies. Its amplitude is set to 20 V peak to peak, between -10 and 10 V. This requires to check the box for amplification.

Table of the taken measurements and parameters in appendix.

6.6 Set of scans and choice of parameters to analyse

This section summarises the measurement strategy that was applied in this master thesis to guaranty for quickly exploitable results. The composition of the measured sample is first reviewed before moving on the type of measurements taken and the strategy behind those.

Regarding sample set choices, the measurement that drives the decisions is the vibrometric measurement, as resonant frequency is the main parameter of interest in this project. The samples membrane sets are composed to present at least one die of each available design for each of the wafers. First, for non-grinded dies, most of the membranes sizes were available for each wafer. Some are present in several exemplars but the chosen strategy here is to measure as much different sizes as possible. The goal here is to enable comparison with the models and simulations. The membrane sets for each sample are detailed in Table 6.1.

Concerning grinded dies, there were only four available dies. All of them have been measured. The initial goal was to measure a full square membrane set from 400 to 1600 µm side length from one of the wafer i.e. WF4. To allow for a comparison across all wafers, one die with 800 µm membrane was fabricated for WF5 and WF6. The comparison here will be indicative and done between only two wafers due to failure during the etching of the WF5 die.

Before the vibrometric measurement, the membranes are scanned for their topography to determine their curvature. This measurement's purpose is to check for any curvature or other problems that could arise during the sample preparation such a glue on the membrane. This gluing done can occur because the capillarity inside the membrane allows it to climb up to the membrane. If the membrane is fastened down to the sample PZT support, it can be easily detected with a topographic measurement.

The vibrometric measurement is done next. This order is chosen because the set-up for vibrometry requires more time for its proper installation and check for correct membranes to measure before actually measuring them can avoid measuring membranes that are not comparable to the models. However, modifying the order between topography and vibrometry does not impact the measurement quality.

Some gluing techniques can have impact on the dies because they require a curing in a oven. This curing modifies the gluing material and can provoke several phenomenons. In case of unexpected measurement looks, the full measurement procedure can be repeated to determine if these effects are temporary.

7 Results and discussion

This chapter presents the results of the full fabrication process. It compiles the results of fabrication and post-fabrication basic characterisation to the topologic and vibrometric measurements. The techniques used for the post-fabrication characterisation, the topology determination and the vibrometry are described in Chapter 6.

First, the results are reviewed directly in sections 7.1 for topology and section 7.2 for vibrometry. They are discussed regarding their relevance and the analysis that was made to extract the parameters of interest is explained. The main axes are the comparison between results themselves and the potential hypotheses for some out-of-range measurements that were taken. After this first hand discussion, section 7.4 proposes a comparison with theoretical models, simulations and state of the art. This section discusses the results relatively to what was expected. Last section examines opportunities for further improvement of this work regarding the previous discussion. It also makes a link back to the applicative context of this project.

7.1 Topographic results analysis

Before reviewing the obtained frequencies, the membrane topography is analysed. The first thing is checking the consistency of the measurements and locating optical artefacts to identify them. Next, each of the measurements could be reviewed. The analysis is performed as follows: first step is to take the measurement axis along the direction of the residual fringes to avoid these artefacts in the measurement. The second is to locate the artefacts due to the change in reflectivity of the surfaces. Last step is the extraction of the potential curvature of the membrane to determine whether it is in tension or if it shows buckling due to compressive residual stress or any other pressure that could be different under the membrane than the atmospheric pressure.

The check for optical artefacts begins before the scanning occurs when verifying the reflective intensity. An abrupt change in intensity can systematically be noticed at the membrane borders. This is illustrated in Figure 7.1 and 7.2 that show respectively the measured membrane and the intensity of the reflection. In Figure 7.2, the membrane can be identified as the less reflective region with the fringe crossing it. The edge of the die can also be seen, with a close to zero intensity.

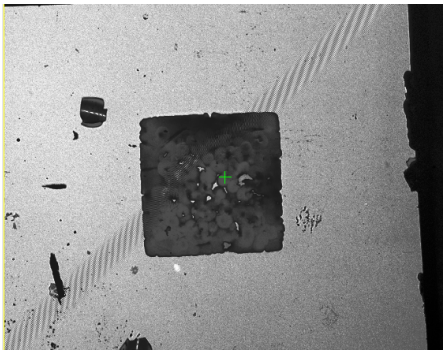

Figure 7.1: *Membrane during topology measurement*

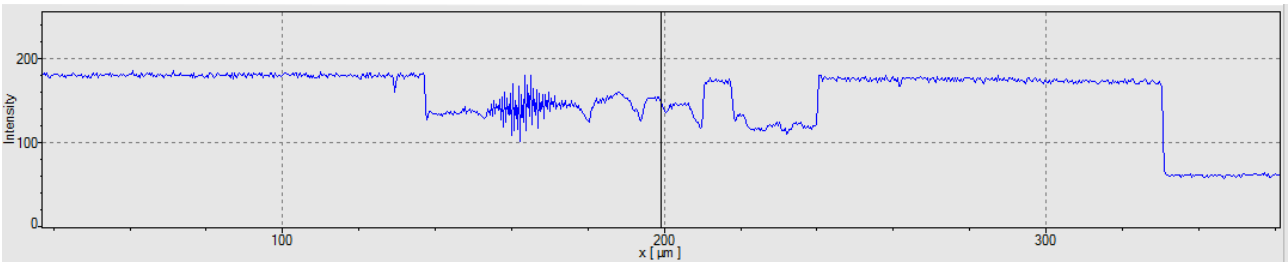

Figure 7.2: *Intensity of the reflection corresponding to the membrane from Figure 7.1*

In the measurements, the artefact caused by reflective change can be seen in the scan display as the darker border around the membranes as in Figure 7.3. The full membrane is also shown as being globally higher than the other parts of the die due to the reflectivity of the film on substrate being different than that of the film in air. Other artefacts are also present in the form of visible fringes. A more correct measurement is simply obtained by taking the profile along a line parallel to these fringes.

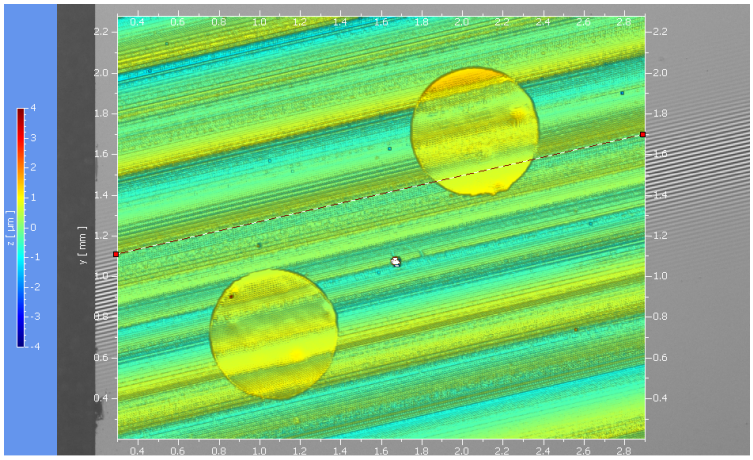

Figure 7.3: *Topology results of a 600 µm diameter membrane*

Next, the height is extracted using the step measurement included in the Polytec TMS software. The height measured between the global membrane and the rest of the dice was consistant at around 700 nm and the height of the borders of the membranes are systematically close to 1 µm. This corresponds to the thickness of the film and the same type of reflection loss region at the membrane edge that can be seen in Figure 7.2.

Membrane	Step [nm]	Max. Deflection [nm]
WF4		
400	742	40
600	631	<10
800	621	<10
950	601	<10
1200	693	<10
1350	1327	165

Table 7.1: *Topology measurements of membranes from wafer 4*

Regarding the curvature of the membranes, every measurement for wafer 4 samples can be found in Table 7.1. Most of them present curvatures too small to be discriminated from the present noise. They are indicated with maximum values in the table. Only the 400 and 1350 membranes showed higher values and the most alarming was that of the 1350µm membrane as it exceeds 1% of its side length.

These measurements were taken to allow for a better knowledge of the membranes, especially in specific cases such as that of the membranes glued with blue resist on the B sample. It also allowed to confirm that some membranes got partially glued to their edges. This is the case of the 1350µm membrane of wafer 5. This membrane was kept in the sample because its gluing remained small enough to still have an interesting measurement. This is shown in Figure 7.7.

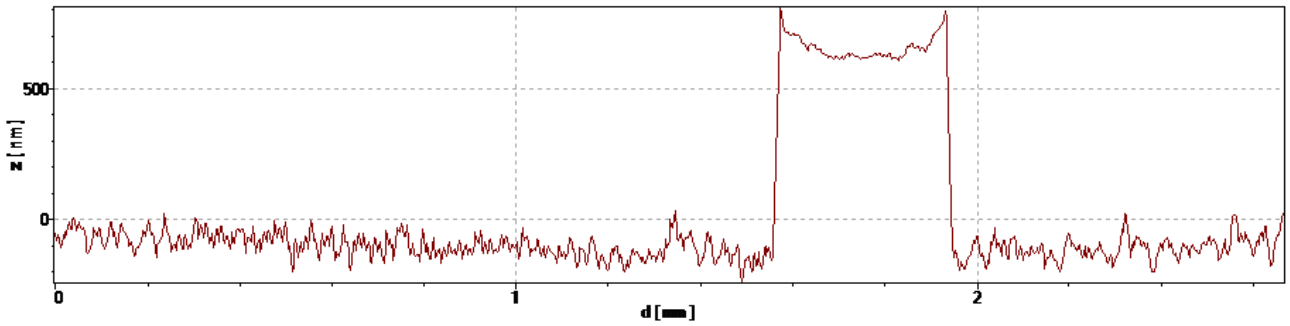

Figure 7.4: *Profile line of the curvature measurement of the 400µm square membrane from wafer 4*

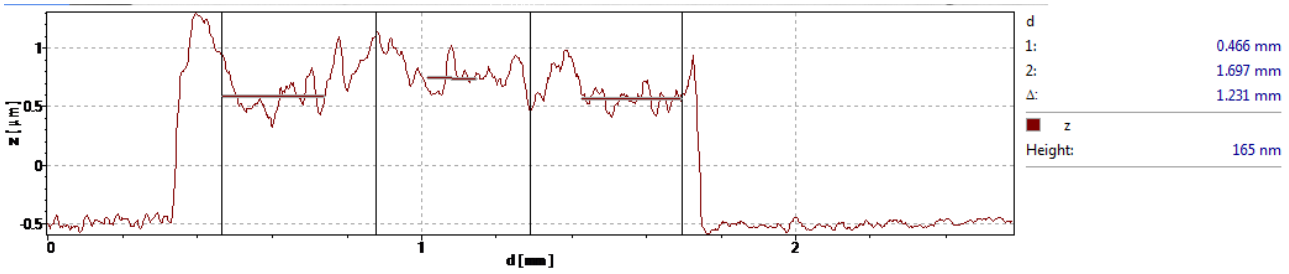

Figure 7.5: *Profile line of the curvature measurement of the 1350µm circular membrane from wafer 4*

7.2 Laser vibrometry results for standard thickness dies

This section presents the results that were obtained using the Polytec laser vibrometry and how they were analysed to extract the resonant modes. Before moving to the die per die analysis, some general observations can be made regarding the global look of the spectrums from Figure 7.10, 7.11 and 7.12. On the curves, the red round markers indicate each new detected mode shape. The exact values for mode 1 frequency are given in Table 7.2 along with the measured values of the design parameters : stack thickness, width of the pattern and residual stress.

First of all is that all of these spectrum present strong response around 100kHz. This is identified as a resonance of the die-PZT-plate system rather than the membranes in most cases. It can be an issue for membranes with expected resonance frequencies close to these frequencies. Most of the time, it could still be discriminated thanks to the camera view available on the Polytec setup and the display of the modes on the PSV software.

Second is that the most clean form of the mode do not always show the highest amplitude. This can be due to the measurement type : the periodic chirp is composed of a discrete set of frequencies. Hence, it happens sometimes that the measurement is taken right next to the best expression of the mode, resulting in a lower amplitude.

The last general observation that can be made is that these measurements are analysed and displayed with an amplitude chosen to be the speed of the membrane. This also reflects the kinetic energy of the membrane. It it easier to locate the modes as they have much higher amplitude than the noise around them. Using a distance based measurement is another possibility but at large frequencies, the displacement tends to be very small even though the kinetic energy is high. This makes modes difficult to locate in a displacement-based plot. Such a displacement plot is displayed in Figure 7.6 for illustration. It can be seen that the distances are measured in nanometers and that the strongest resonant mode merely reaches a third of the maximal deflection at the lowest frequency, here 1kHz.

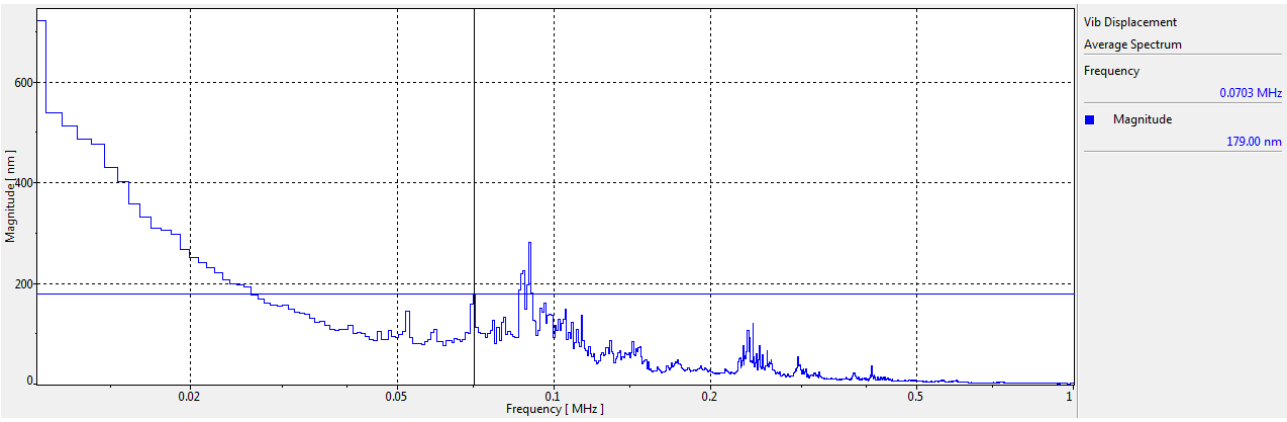

Figure 7.6: *Displacement plot of the vibrometric measurement of the 1600µm membrane from wafer 5*

7.2.1 Double side polished wafer - Wafer 5

The analysis of the measurements starts with the wafer 5 as it is the simplest to analyse. Measurements, except for the 1850µm membrane, show a readable amplitude. Regarding the largest circular membrane, the degradation of the scan quality could be due to residues of organic material that got stuck on the die during a manipulation to retrieve it from the broken piezoelectric disc.

Membrane by membrane, the 1600µm spectrum shows a first high spike that corresponds to the first mode at 70.3kHz. The second is the mode 12 or 21 in a diagonal fashion on the second peak at 89.8kHz. This mode shows higher speed and higher displacement if the spectrum is compared with Figure 7.6. This is in contradiction with the classical assumption that first mode is the strongest. Around 100kHz, the numerous spikes are not pure modes as the die itself moves a lot. The three other indicated modes correspond to the 13 (or 31), 23 (or 32) and 33 mode shapes. The highest spike is the 14 (or 41) mode. The comparison with the displacement chart in Figure 7.6 helps here to understand that even though this mode has high energy, its displacement is smaller than the lower modes.

Other spectrums can be analysed the same way. The larger membranes all show the same tendency to have lower energy in mode 1 than in mode 12 or 21. This is less true for smaller membranes. It can be seen that 400 and 600µm membranes have much larger mode 1 than the rest of their modes.

Regarding the first mode resonant frequencies, they follow the model and simulation results within a 5% margin for the square membranes. The circular ones are also close to the expected values within a larger 10% with an exception for the large 1850µm membrane that is 20% below the awaited first mode resonant frequency. The measured first mode frequencies are in general slightly lower than the theoretical previsions for the large membranes. This can be linked to the damping that is not taken in account in these models and simulations. It can be observed that this effect is not as strong as the multiphysics simulation predicted it. This indicates that there could be an issue with the simulation. It can also be observed that the larger stress, the broader patterns and the slightly thinner stack seem to compensate for each other and balance out the effects that one of these change alone could provoke.

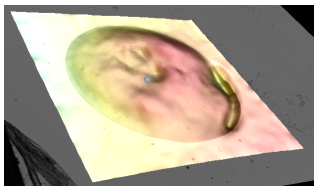

Figure 7.7: *1350µm membrane from wafer 5, partially glued*

As explained in section 7.1, the 1350µm membrane is a special case : the accidental gluing of the membrane to the edge from the backside narrowed the surface but did no stop it from resonating. This explains why this membrane is showing a higher mode 1 frequency than what the model predicted. The glue can clearly be seen, in the bottom right corner, as the stripe in Figure 7.7 showing the first mode of this membrane.

7.2.2 Dies from standard wafers 4 and 6

Spectrums of wafer 4 and 6 show the same tendency regarding the lower first mode energy for large membranes and higher for smaller ones. However, some differences must be noticed.

The spectrums of wafer 4 in Figure 7.10 show way lower speed than those of wafer 5 in Figure 7.11. Yet the spectrums present clear spikes at the modes. The disturbance around 100kHz can also be seen in these curves.

The spectrums of wafer 6 also show very low speeds over all frequencies. This means the displacements are very small at all modes. The die displacement and the noise appear thus stronger and can create confusion or even supersede the modes of the membranes. It is the case in the 1200µm membrane where Figure 7.12 shows only one mode. The other ones could not be identified. Since these membranes are glued using the same Pattex glue as those of the membranes of wafer 5 that present modes closer to the models, several hypotheses are proposed but none could be verified as it would require to fabricate more membranes :

- stresses induced by the curing of the glues when preparing the samples could impact the stress in the membranes
- large amounts of grass residues are visible on wafer 6 membranes, these could impact the vibrometric measurement as they change the reflection of the surface
- the grass piles could directly influence the deflection and the resonance frequency as these change locally the rigidity of the membrane
- because the membranes are very fragile once released, they were not rinced in isopropanol and water after release, this makes it possible for more organic residues of the resist to stay on the dies, this could further impact the quality of the measurement

The values from wafer 4 follow the same tendency as wafer 5 for the small membranes : they are close to the analytical expectations. However, the larger ones, here 1200µm side and 1350µm diameter respectively, show much lower resonant frequencies than what they were designed for. The dies here are thicker, which causes the membranes to be a little larger than those of wafer 5, by approximately 10µm. The measured stress is also lower by 6MPa. However, since the small membranes remain very close to the theoretical previsions, these small effects can not explain by themselves the gap between expectations and reality for these two membranes. The topology measurement showed a curvature that was higher for the 1350µm membrane so an effect that is linked to external stress impacting the membrane could be present. This could be anything such as a gas from the resist used to glue these dies that remains trapped underneath or stress caused during the curing and the following cool down.

The change of density inside the resist during the curing time and the residual stresses inside that resist could induce such stresses. A complementary experiment reproducing this gluing technique should be done to check on this hypothesis.

In the case of wafer 6, most membranes show resonant frequencies ways lower than expected, except for the smaller ones. Here, the curing of the glue used should have no thermal residual stress impact as Pattex glue cures in seconds at ambiant temperature. This should thus have another origin. It could still be linked to the curing changing the density of the glue but this glue was used the exact same way for dies of wafer 5 and no frequency change was observed. Another observation can also be linked to lower frequencies in this project : the presence of grass piles on the membrane.

The residual grass piles are more present on the dies of the wafer 6 than on those of the wafer 4 because the numerous RIE etching steps that were performed in the Oxford Plasmalab gradually made the etching chamber dirty. This is caused by accumulation of teflon layers inside the chamber. During fabrication, it was noted that the backside of the support wafers was more and more dirty after the

etchings. Some teflon that deposit on a small area in a layer that is too thick can provoke micromasking inside the etched pattern. This tends to happen more in dirty chambers and on rough backsides. Since the overetching is minimised to preserve the membrane and the slopes are very straight, these can not be underetched and removed easily. This results in large grass piles such as shown in Figure 7.8. The membranes presented there are 400µm and 600µm large but more of such piles can be found in larger membranes as it tends to be localised at the centre of the membrane.

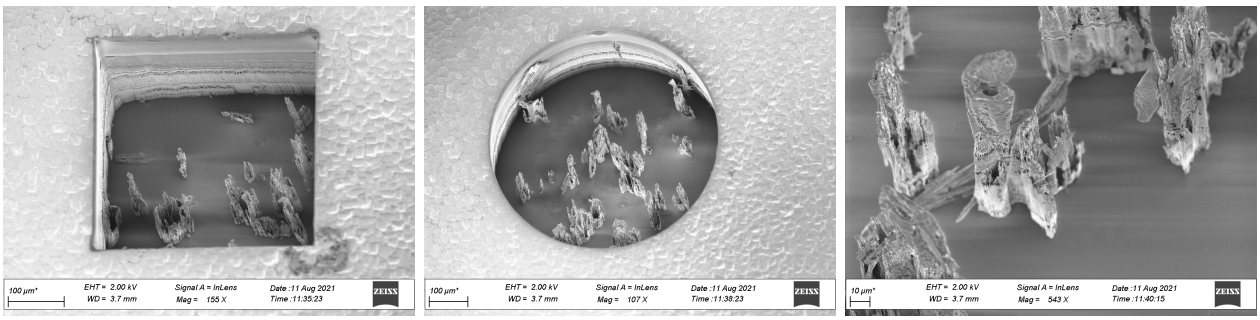

Figure 7.8: *SEM images of the grass piles in membranes of wafer 6 a) 400µm square membrane b) 600µm circular membrane and c) close up*

The frequency values that can be seen in all measurements that are off the expected value by a large margin can all be linked to membranes showing more grass piles as indicated in Table 7.2. The Figure here below illustrates this for the wafer 4 : the 400 and 800µm membranes show no piles or only very sparse ones whereas the 1200µm one shows lots of these.

The exact way these grass piles impact the resonant frequencies of the membrane remains to be determined and would require more experiments and reprocessing of some of the samples to remove these grass piles. However, several hypotheses can be made, based on the fact that the mode 1 frequency is lowered. They are proposed here for further investigations :

- Etching is stronger around the grass piles and causes the membrane to be thinner. However, this would mean the residual stresses are higher as the stop layer is the compressive silicon dioxide layer.
- The localised position of these piles has sufficiently low density to have a very small impact on the membrane properties but the additional weight of these long piles that can reach more than 100µm could be sufficient to change the resonant frequencies and the maximal deflections.
- Stress concentrations around the grass piles could also change the visible modes.

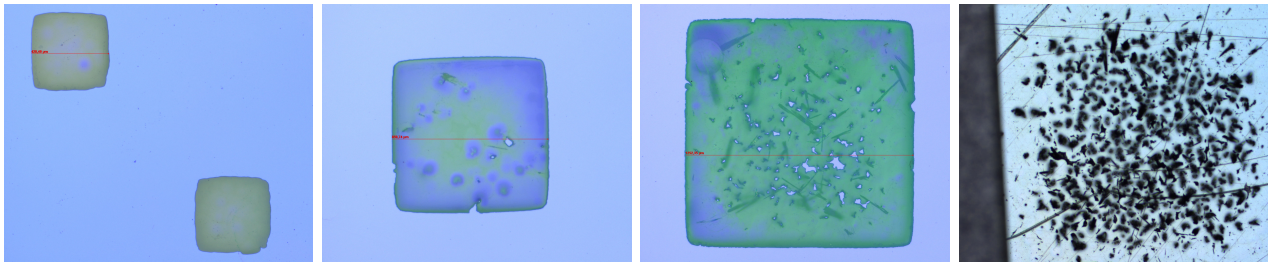

Figure 7.9: *Comparison of the membrane state for grass piles for square membranes of the wafer 4 a) 400µm b) 800µm c)1200µm and d) grass from the backside of a membrane*

Membrane	Membrane thickness [nm]	Measured side/diam. [µm]	Total residual stress [MPa]	Expected Mode 1 Freq. [kHz]	Measured Mode 1 Freq. [kHz]	Grass Piles -
WF4						
1200	965.5	1252	67	97	40.6	Dense
800	965.5	860	67	147	148.4	Very sparse
400	965.5	428.5	67	304	310.9	No piles
1350	965.5	1402	67	78	46.9	Dense
950	965.5	1001	67	138	137.5	Very sparse
600	965.5	628.92*	67	312	218	Dense
WF5						
1600	967	1625*	73	73	70.3	No piles
800	967	825.93	73	147	152.3	No piles
400	967	435.42	73	304	288.3	No piles
1850	967	1844.701*	73	50	40.47	Sparse
1350	967	1386.9	73	78	89.11 **	No piles
950	967	972.659*	73	138	139.8	No piles
600	967	637.26*	73	312	288	No piles
WF6						
1600	980	1640.38	72	73	22.19	Very dense
1200	980	1253.05	72	97	28.0	Very dense
800	980	841.81	72	147	104	Dense
400	980	447.199*	72	304	300.62	Very sparse
1850	980	-	72	50	28.1	Very dense
1350	980	1383.5*	72	78	45.3	Very dense
950	980	990.15	72	138	67.19	Very dense
600	980	648.44*	72	312	296.88	Very sparse
Grinded WF4						
1600	965.5	1620.98	67	73	58.05	No piles
800	965.5	831.78	67	147	40.47	No piles
400	965.5	428.49	67	304	312.5	No piles
950	965.5	975.66	67	138	75	No piles
600	965.5	626.08*	67	312	232.89	No piles
WF6						
800	980	817.04	72	147	138.98	Very sparse
950	980	970.83	72	138	113.44	No piles

Table 7.2: *General results for first mode resonant frequency, width measurements marked with * are taken using the Polytec and are thus approximations, the frequency marked ** was measured on a partially glued membrane*

7.3 Vibrometric exploratory measurement of resonant frequency for membranes on grinded dies

This section presents the spectrums obtained for the membranes etched in grinded dies. They can be found in Figures 7.16 for wafer 4 and 7.17 for dies from wafer 6. These measurements are exploratory as no comparison can be made across more than two membrane sizes for the circular design or across all wafers for any membrane size. The measured membranes are 1600µm, 800µm and 400µm square membranes from wafer 4, 950µm and 600µm circular ones from wafer 4 and 800µm square and 950µm circular designs from wafer 6. This section begins with some preliminary general remarks on these dies and the measured parameters available in Table 7.2.

These dies are approximately 100µm thick. This makes them difficult to handle and to glue on the piezoelectric discs. Some of the membrane could thus touch the glue or dies could be badly glued. Two of those from the 800µm and 950µm die of wafer 4 even broke during manipulation.

The same die disturbances around a little more than 100kHz can be seen in the spectrum. These tend to be relatively larger on grinded dies compared to standard dies. This could be directly linked to the more difficult manipulation of the dies during sample preparation, leading to the dies being poorly fastened to the piezoelectric disc compared to the full thickness ones.

Comparing the first mode frequencies, it can be seen that even though some show very low frequencies, others are very close to the expectations. The amplitudes are quite small but most of the modes can correctly be identified.

7.3.1 Grinded dies from wafer 4

The 1600µm square design shows some glue touching the membrane and fastening it to the edges. It is illustrated in Figure 7.13 a. This reduces the amplitude that can be attained in terms of displacement even if the membrane is fastened and thus the amplitude of the measured speed signal is lowered. This still does not totally explain totally the low frequency that is measured. Another thing to note is that the measurement is very irregular even if the membrane shows no grass piles as illustrated in Figure 7.13 b. This could be linked to the teflon residues covering the die as can be observed in Figure 7.13 a. This is not confirmed yet and would require further experiment for confirmation.

It can be seen in the Grass piles column that these die are almost totally spared from this phenomenon. However, the frequencies are lower than expected. Only the 400µm shows a frequency within a 10% margin. The membranes are larger than what is designed due to the lithography imperfections. However this is not sufficient to explain the largest differences.

The two membranes showing the lowest frequencies are the 800µm and 950µm ones also show an irregular film. This film is depicted in Figure 7.14. Such irregularities are linked to local stress concentrations inside the film or to buckling. This would explain why the frequencies are so much lower than what was awaited. Still, the modes from the 950µm membrane are very clear on the measurements, even with higher ones such as the 41 mode with 4 nodal circles and one nodal diameter.

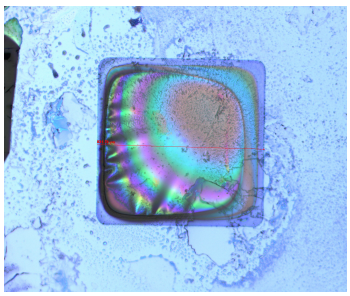

Figure 7.14: *Irregular membrane film from 800µm square membrane from wafer 4*

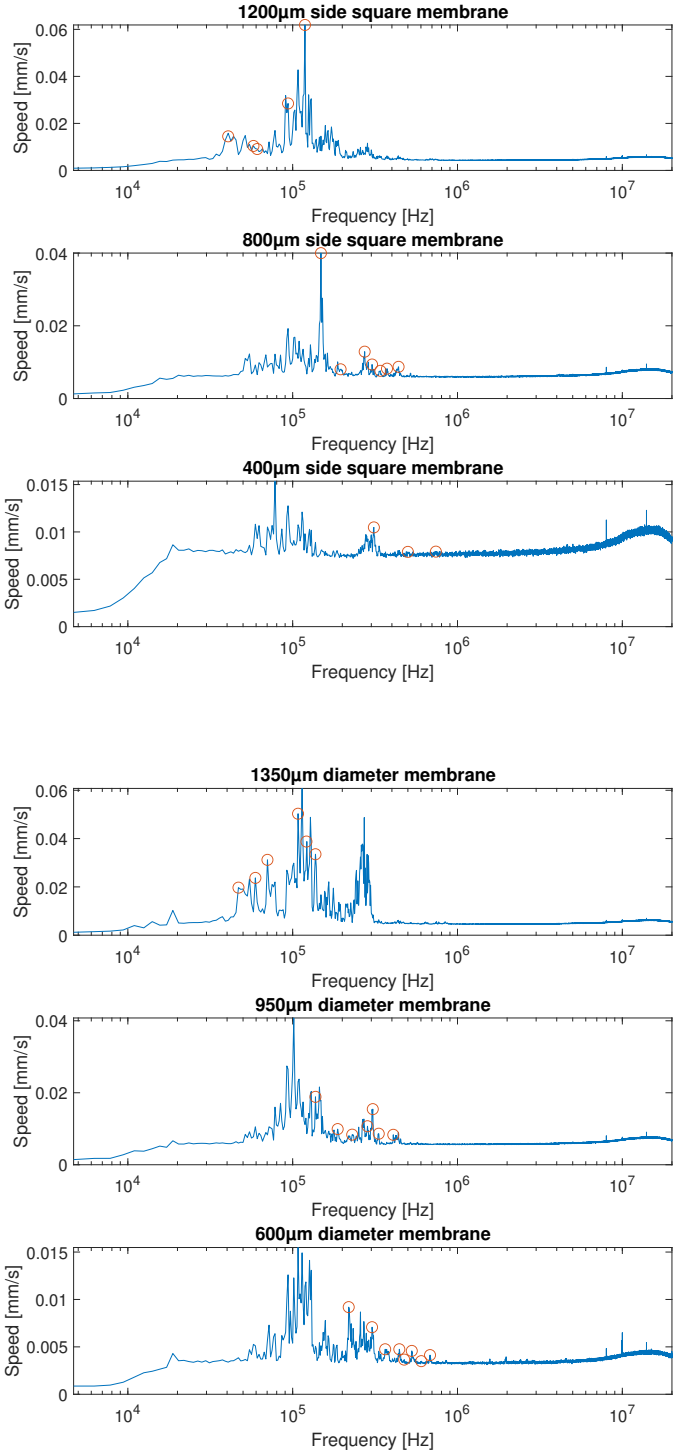

Figure 7.10: *Spectrums obtained from membranes of the wafer 4 with the identifiable modes indicated*

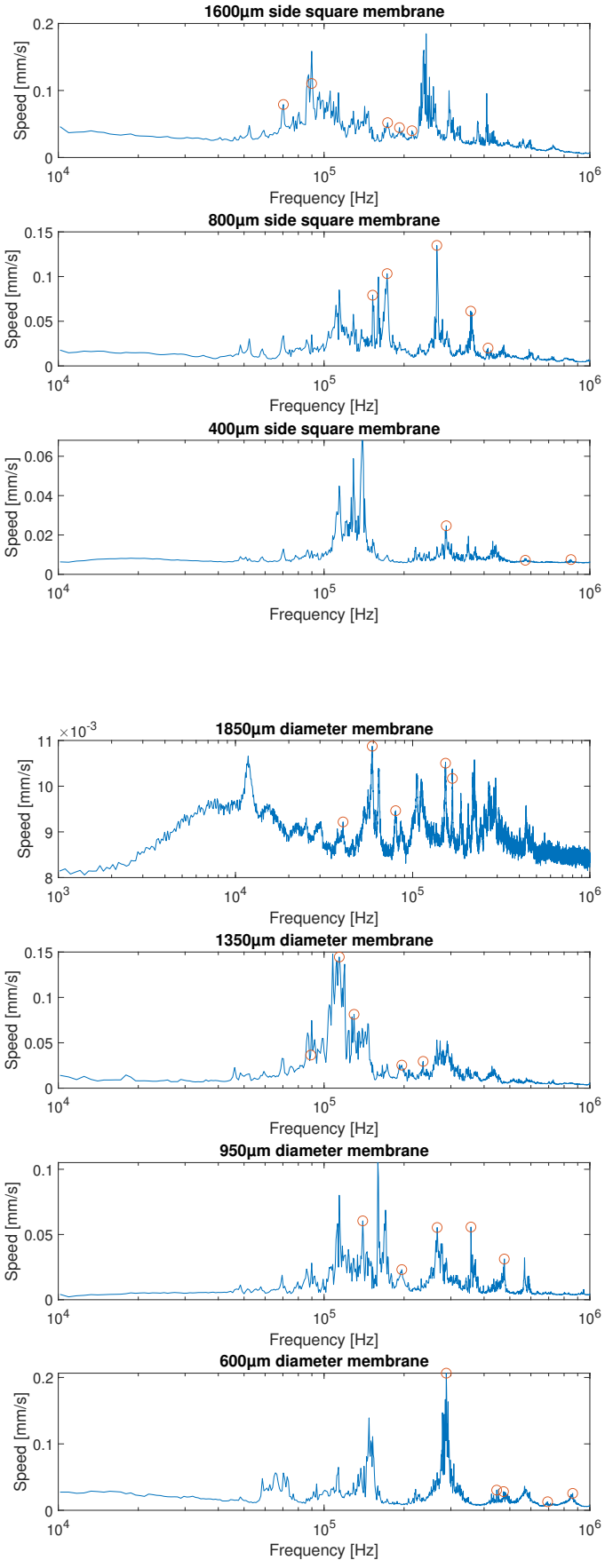

Figure 7.11: *Spectrums obtained from membranes of the wafer 5 with the identifiable modes indicated*

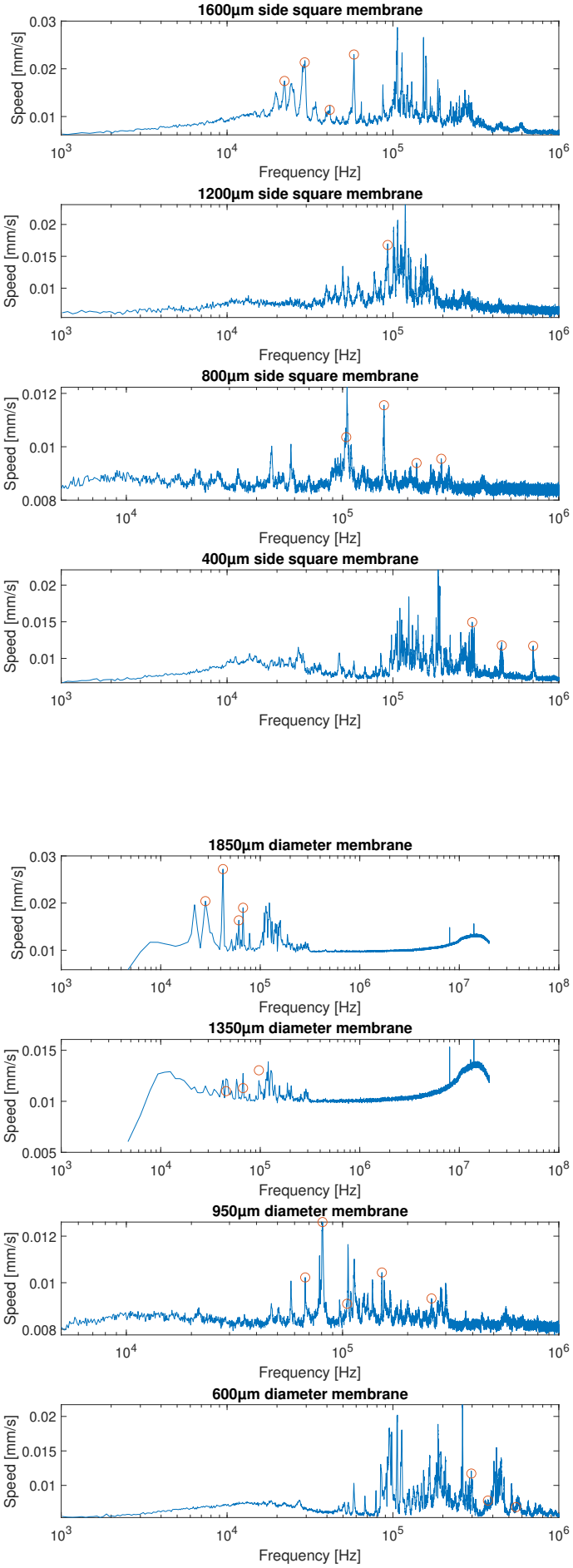

Figure 7.12: *Spectrums obtained from membranes of the wafer 6 with the identifiable modes indicated*

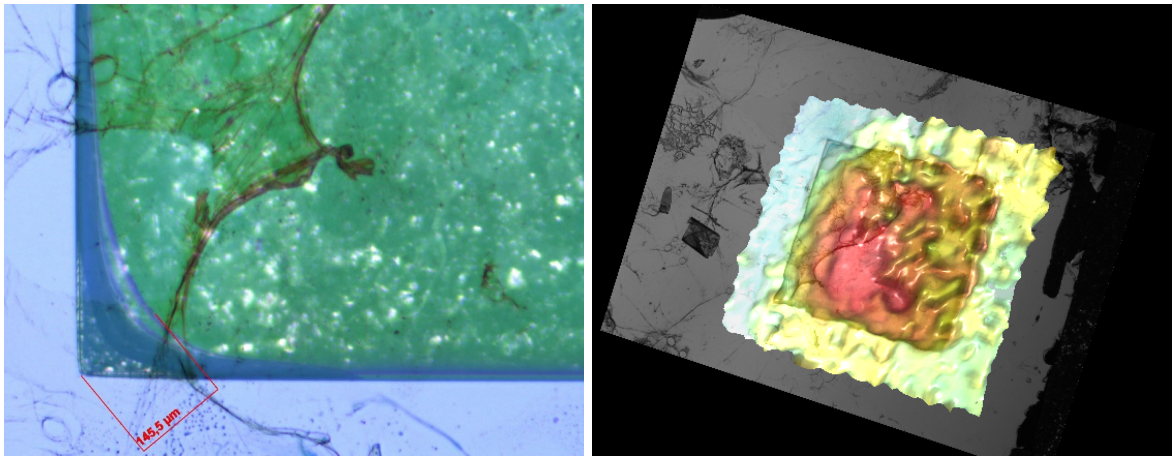

Figure 7.13: *a) Glued corner of 1600µm membrane from wafer 4 grinded die and b) irregular look of the measurement*

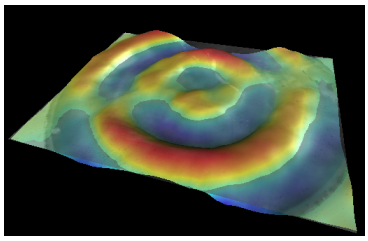

Figure 7.15: *41 mode of the 950µm membrane*

Regarding the smallest membranes, the 400µm membrane is totally in line with the expectation. The 600µm circular shows lower first mode. This is closer to what the Comsol simulations show but in contradiction with what could be observed on the other dies. To find the cause of this lower frequencies, further experiments would also be needed.

7.3.2 Grinded dies from wafer 6

The two dies from wafer 6 show low amplitude in their spectrum but this could be because these membranes are relatively small. They also show very little grass piles. Their first mode resonant frequency are relatively close to the predicted one. The error margin is still higher than for the non-grinded dies.

Observing the 800µm membrane measurement, it can be noted that only two modes could be identified. This is due to large die disturbance that make it difficult to distinguish correctly between a real membrane mode and a vibration affecting the whole die.

The spectrum of the 950µm membrane is quite busy and shows a lot of pseudo-modes linked to the membrane moving along with the die. However, the spotted modes are well defined, even the higher ones, the same way as the ones from the other 950µm circular membrane from grinded dies.

7.4 Results comparison with analytical models, design parameters and simulation outcomes

The following paragraphs propose a comparison of the results from the measured membranes to the models and simulations that are used in Chapter 4 for the theoretical approach. The main objective is to determine whether the chosen or proposed models are relevant enough and how alignment between fabricated devices and theoretical models could be improved.

The first comparison is done regarding the used parameters for design : thickness, width, internal residual stresses in the stack and first mode frequency. The second is based on the modes that can be observed in reality versus in simulation. An important point to note is that all these comparison are done with the mutlilayer in vacuum Comsol simulation. The simulation including the damping gives

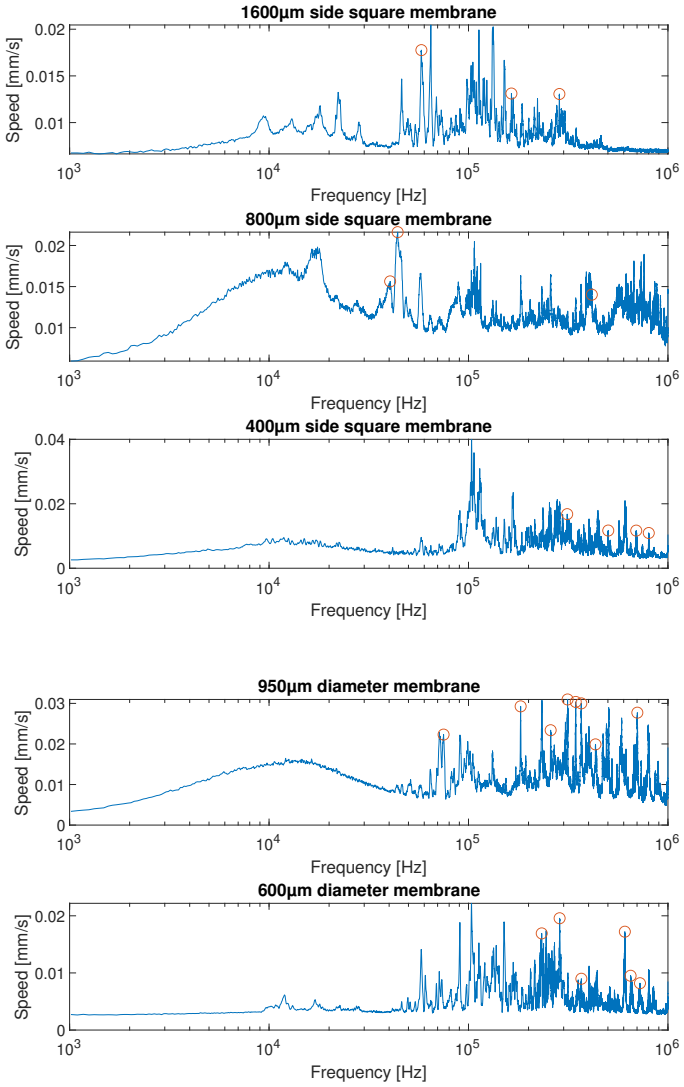

Figure 7.16: *Spectrums obtained from membranes of grinded dies of the wafer 4 with the identifiable modes indicated*

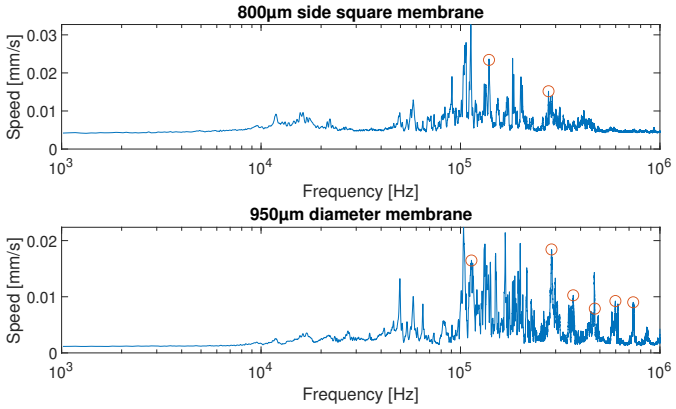

Figure 7.17: *Spectrums obtained from membranes of grinded dies of the wafer 6 with the identifiable modes indicated*

much lower expected frequencies and no membrane was found to be in line with these expectations.

7.4.1 First mode comparison between analytical models, Comsol simulation and real measurements

Figures 7.18 and 7.19 show the design curves that were used and the frequencies obtained with the Comsol simulation as in Figures 4.23 and 4.23 compared with the frequencies obtained with the fabricated membranes. The experimental datapoints only reflects the full-thickness dies in these graphs. Generally, it can be seen that the membranes that do not suffer from grass piles effects follow the awaited tendencies. It is less clear for the circular model than for the square one because no grass-pile-free membrane of 1850µm could be measured. Yet, based of the other points, the general look is close to the prediction.

The square grass-piles-free membranes follow the models almost perfectly. Their mode 1 frequency tends to be slightly higher than the expectation for the smaller ones. This behavior is closer to the Comsol FEM simulation than to the model. The error margin still remains very small. Regarding those with grass piles, it can be seen, by comparing the three 1200µm membranes, that their impact on the first resonant frequency seems to be correlated with their observed density. This could correspond to the same behavior as the membranes with islands used for sound wave absorption whose mode 1 resonant frequency is modified by the distance between the islands and tends to be lower for closer islands [46].

The circular membranes show less clear behavior. The mode 1 frequencies for the membranes that present no grass piles seem to be closer to the proposed model for the smaller membranes but closer to the Comsol simulation for the larger ones. The proposed model, even if it gives a good idea of the order of magnitude, is confirmed to overestimate the impact of the diameter of the membrane. It should be revised before being used further for design.

The membranes impacted by grass pile at a high density tend to follow a curve with the same general look but simply shifted downwards. The same considerations regarding the density of the grass piles can be made as with the square membranes. Modelling these could be attempted by changing the density of the material to simulate the presence of the weight of the grass piles. As a higher density lowers the resonant frequency, charging the membrane with additionnal mass without modifying its properties otherwise would produce approximately the same effect. This could be compared to the effect of seismic mass in membrane-based accelerometers.

7.4.2 Higher modes comparison with Comsol simulation

Regarding the higher modes, the values have not been thoroughly extracted from the theoretical models but a comparison with Comsol can be made. It is done here for two membranes that are in line with expectations for their first mode resonant frequency : 800µm square and 950µm circular from wafer 5.

Comparing the mode shapes that appear in the Comsol simulation and those that can be found during the measurements of the real membranes is done in Tables 7.3 for the square design and 7.4 for the circular one. The Comsol simulation always gives the same sequence of mode shapes as it can be seen in Tables 4.6 and 4.7. These can be found in Figures 4.14 and 4.15 for illustration. In the case of the fabricated membranes, the modes that could be located do not always follow the same sequence as some of them are covered by the die disturbances or simply inhibited by the grass piles or any other external residue. The frequencies obtained for these higher modes are in agreement with the simulated ones with a slightly growing error margin as the modes gets higher.

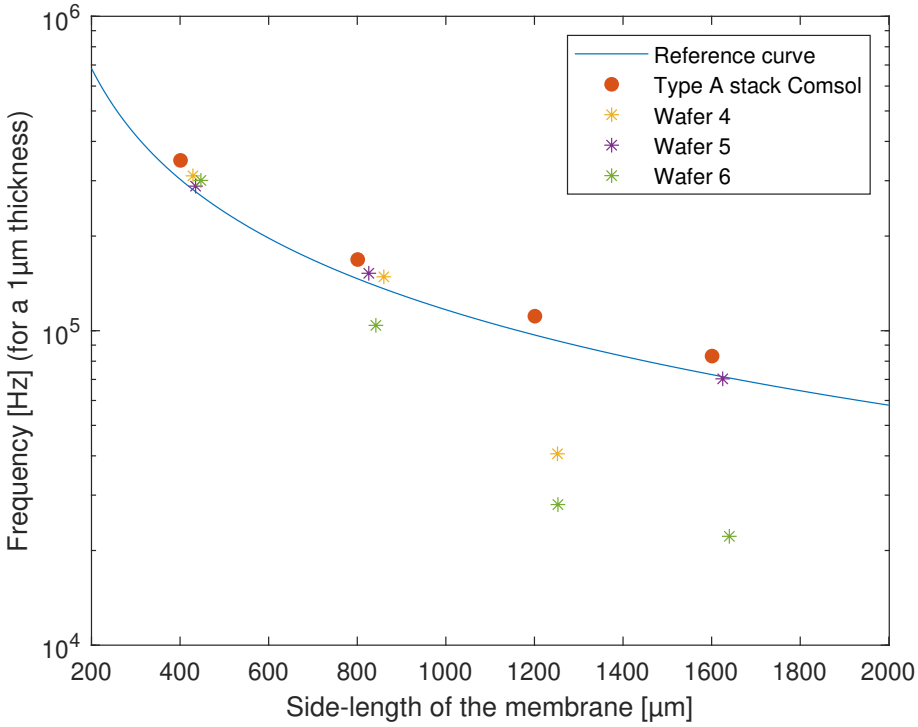

Figure 7.18: *Comparison between the model used for design, the FEM simulation results in Comsol and the fabricated membranes for the square designs*

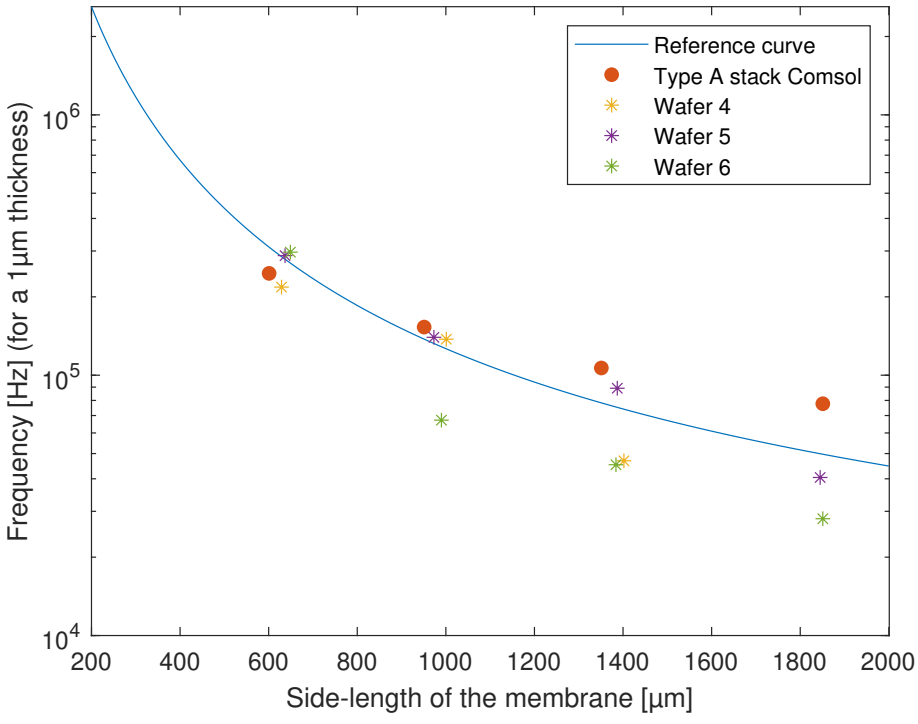

Figure 7.19: *Comparison between the model used for design, the FEM simulation results in Comsol and the fabricated membranes for the circular designs*

Another phenomenon that must be noted is the superposition of square and circular modes for the lowest ones in square membranes with rounded corners. It is the case with the 800µm membrane from wafer 5 that presents a circular 10 mode, with one nodal circle and zero nodal diameters and this phenomenon could also participate in the lowering of the first mode of the membrane.

Mode shape	Comsol [kHz]	Real [kHz]
11	168.5	152.3
Circ.10	-	172.7
12	267.0	265.6
21	267.2	-
22	339.0	-
22 bis	379.2	-
31	379.7	356.3

Table 7.3: *Comparison of the higher modes frequencies with Comsol prediction for 800µm square membrane from wafer 5*

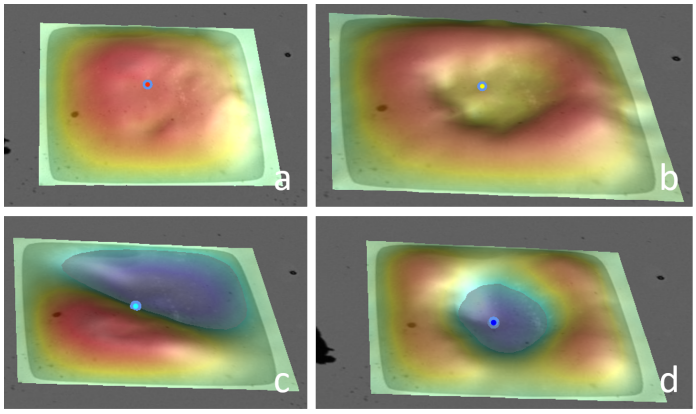

Figure 7.20: *Mode shapes of the 800µm square membrane from wafer 5 a) 11 b) Circ. 10 c) 12 and d) 31*

Mode shape ij	Comsol [kHz]	Real [kHz]
00	153.0	139.8
01	244.4	196.1
01 bis	244.5	266.4
02	328.7	-
02 bis	328.7	-
20 bis	353.7	357.0
21	-	476.6

Table 7.4: *Comparison of the higher modes frequencies with Comsol prediction for 950µm circular membrane from wafer 5, i : nodal circles j: nodal diameters*

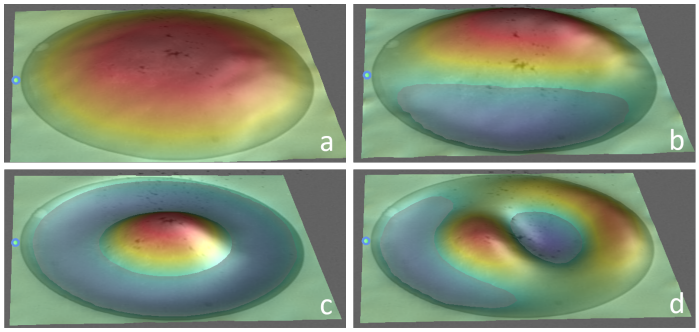

Figure 7.21: *Mode shapes of the 800µm square membrane from wafer 5 a) 00 b) 01 c) 20 and d) 21*

The lower eigenfrequencies could be interesting to work at, especially mode 12 or 21 square that can possibly be found to be stronger in displacement than the first mode as in membrane 1600µm square from wafer 5 and other square ones. No experiment was done to determine why this happened and it should be investigated. However, if one wanted to use such larger mode 12, the question of the application of the membrane must be taken in account : the interesting signal should not be diminished if the membrane is used at this resonant mode. Most of the applications rely on the deflection of the membrane but not all in the same way. Piezoresistive and piezoelectric application could benefit from it as deflection is larger and stress goes along. On the other side, for capacitive or interferometric applications, such higher modes would make the sensor totally inefficient as mean displacement is zero for capacitive applications and the center of the membrane is not moving anymore.

7.5 Interesting pathways for further improvements on the present results

This section covers the different aspect of this work : theory, fabrication, in process and final metrology and reviews interesting pathways that could be followed to improve the obtained results.

7.5.1 Model for circular designs

Regarding the theoretical aspects, this master thesis proposes a model for eigenfrequency computations of circular membranes that includes the impact of both the thickness and the stress. This model is not precise enough and should be corrected. It should also be tested to see if it predicts correctly the higher modes. To improve this model, a pathway that could be explored is to adapt a model for plates. Such models include all needed parameters, thickness, width, stress and material parameters.

The following model is proposed by [15]. This expression is given for fully clamped circular plate with a tensile stress :

$$f_{ij,plates} = \frac{\lambda_{ij}^2}{2\pi a^2}\left[\frac{Eh^3}{12\gamma(1-\nu^2)}\right] \tag{7.1}$$

where the λ_{ij} coefficient is function mode shape and $\frac{12(1-\nu^2)Na^2}{4.2Eh^3}$ with N the tensile load on the plate.

Still, membranes and plates are not exactly the same : while membranes sustain only tensile loading through in-plane stresses as they have negligible rigidity, like a cable would do for a 1D equivalence, plates will rather reply with bending behavior, like a beam in 1D. [15] Both behaviours are always present but one is most of the time taking over on the other. The change in dominance from plate to membrane behaviour can be estimated to occur approximately when the maximal deflection gets larger than thickness or when internal stresses are high enough. In this project, as seen in Figure 7.6, the thickness and displacement are of the same order of magnitude and stresses are clearly tensile but relatively low. The plate inspired model could thus offer better results.

7.5.2 Simulation of damped eigenfrequencies

The multiphysic simulation that is proposed should be thorougly checked and corrected as its results are absolutely not in line with reality. The boundary conditions seem to be okay but the waves and pressures that are applied should probably be corrected to be more in line with reality.

Adding other non idealities in this simulation could also give a better insight of the real behavior of these membranes. Among the eometric non-idealities that could be interesting, rounded corners and curved edges for square membranes or irregular edges could be tested. Other heavy non-idealities like the impact of grass piles could also be investigated.

7.5.3 Fabrication

Some complementary samples, either new or reprocessed, could give a much better understanding of the taken measurements. The propositions here are not exhaustive but give an idea of what could be realised to pursue the experiments that are done in this master thesis.

The impact of gluing and curing of the dies on the piezoelectric disc could be easily investigated by reproducing the gluing and measuring the frequency right after gluing and some days or weeks later. This would enable the detection of an effect of incomplete curing in the blue resist that was used for sample B with the dies from wafer 4. Other gluing methods using tapes or new glue types could also

be experimented.

The grass piles would also be of great interest for further easy to produce complementary results : some dies could be reprocessed with a isotropic etching to remove them. As the effect of size is correctly modelled and simulated, changing it, even heavily because of underetching, would allow the experiment to show if grass piles are really the reason behind this eigenfrequencies lowering.

Last but not least, process adaptation for thinner dies could be tried. This could include trying the process on grinded wafers, using several sacrificial dies on the same wafer for better results during lithography etc. This process type could also be tried on membranes with islands as these are difficult to process correctly with full-thickness dies and could benefit more of the grinded process than the large patterns used in this master thesis.

7.5.4 In process stress metrology

The main concern about the metrology in process is that stress measurements are very different between the two methods for processing of the data using the Stoney formula if the curvature difference for a step is very large. Whatever the used method, it is clear that using the Stoney formula is making an approximation even though it is widely used.

This could be solved by using a more accurate model specifically for stresses in multilayer thin films. Several possibilities can be found in the state of the art nowadays and could be applied here with or without adaptation of the model [47, 48, 49, 50].

7.5.5 Complementary measurements propositions

To complement the measurements that are analysed in section 7.1 and 7.2 of this chapter, some other set ups could be used to determine the impact of several parameters that are not taken in account in this master thesis. These parameters impact either material properties or the membrane itself and could be of great interest for any application of the proposed designs. This section goes from the easiest set up to build to the most complicated.

The easiest setup would be adding a temperature sensor on the piezoelectric disc and a heating plate to the Polytec laser vibrometry set up to allow measurements at controlled temperature. Even though very small temperature variations should not impact the membrane, largers ones of even a few dozen of degrees could already make a difference in stress inside the film. This would directly impact the resonant frequency.

Testing the sensitivity of the membrane to an accoustic signal could also be implemented. This would imply to use a loudspeaker to produce the wave that hits the membrane. Quantifying the amplitude of the signal could then be a bit of a challenge but similar set ups can be found on a regular basis in literature and even in works done at EPL [21].

Another measurement setup of interest would be to add a vacuum chamber to place the membranes inside. It would allow to detect the imapct of damping on the membrane eigenfrequencies. This is much more complicated to put in place as the piezo electric disc requires electrical wires and the laser vibrometry must have the membrane in sight and focus.

The membranes developped in this master thesis are originally designed for the detection of PD through AE sensing. The current state of development of the project did not allow to test them in a setup reproducing the real conditions of occurence of PD. Such setup is not available in UCLouvain and putting one in place requires a lot of work and competencies that are not related to MEMS or sensor design. This was thus not implemented for this master thesis.

7.6 In context application

This section gives a short insight on the use of the present results in the initial applicative context. It suggests some uses that could be made of the present designs.

These membranes offer a possibility for CMOS integrable ultrasound microphones that would work in resonance in the common AE range for PD. Using several of them in a filter bank or a matrix would allow to have larger bandwidth than a sensor relying on a single resonant membrane.

The obtained results show the proof of concept of adjusting resonant frequency in membranes through residual stress control in the thin film stack be the form square or circular. This allows to implement any conventional transduction. In their current state, the easiest transduction to apply would probably be the piezoresistive or the piezelectric ones on the square membranes. Their main advantage is that these do not require to add a metal layer to the full surface of the membrane like the capacitive of the FP interferometric sensing technique would. However, the design process can be adapted to such a change very quickly.

8 Conclusion

The present research work takes place in the broader context of monitoring of high-voltage equipments for Partial discharges and the increase of the use of sensors in industrial processes. Starting from the interest for non-invasive sensing techniques based on ultrasounds, it quickly narrows down the subject to membrane-based MEMS devices and the quest for improvement in sensitivity. The choice is made to focus on mechanical sensitivity enhancement, through the use of membranes around their resonant frequencies, and the interest to use residual stress control to adjust these eigenfrequencies to the requirements of the application.

The work here goes back to the theory of vibrating membrane structures and uses theoretical models and numeric simulation to predict resonant frequencies. The experimental part of the work focuses on ultrathin membranes made of CMOS-compatible material stack. The membranes that are produced are composed of simplified stacks of stress-controlled silicon dioxide and silicon nitride. These are deposited one on top of another in order to balance out the global equivalent residual stress to the wanted value.

The simple design process that is developed could still be made more accurate : the used analytical model for the circular membranes is not precise enough and should be corrected. Yet, the simplicity of the models makes them perfect to perform quick checks for on-the-go adaptation of the process. The simulation using Comsol Multiphysics multilayered material module enables precise prediction of the behaviour of the membranes in terms of eigenfrequencies. It can also be adapted quickly to the in-process fabrication results in terms of measured stress, thickness and other key parameters to account for possible deviations from the goal of a fabrication step and enable prediction of the effect of process adaptations. However, damping effects remain to be more accurately represented.

The fabrication process puts several key steps and parameters in evidence to ensure good results. The first crucial step is the adaptation of thermal treatments needed in terms of both temperature and timing to control stress in the deposited layers. Improvements on the precision of the data processing technique used to retrieve the value of the stress in the manipulated layer could help to achieve better accuracy in these steps. The second critical step is the etching process and every parameter that favours or inhibits the occurence of grass piles, as their density conditions the accuracy of the frequency control through stress. Several parameters play in the management of this phenomenon but a few simple guidelines can be followed to limit it : using double polished wafers and controlling their development with appropriate periodic isotropic etch steps during the RIE process.

Regarding the fabrication process alternative using thin grinded dies, it is considered functional but its complexity seems unjustified for such simple and large design patterns. It could be interesting to use this type of process for more intricate designs if the lithography steps can be improved.

The fabrication process produces results that are in close adequation with design and simulation expectations. The membranes that do not present dense grass piles not only comply to the design requirements for the first mode resonant frequency within a small (5%) error margin but also show predictible higher modes at frequencies that are close to the predictions from the Comsol simulations.

Event though PD detection applications are at the origin of the frequency range choice, the developed membranes designs and fabrication processes are currently very versatile. It would be easy to use them in designs that comply to the requirements of another pressure sensor.

This master thesis contributes to the foundation for future sensors designs using ultrathin CMOS-compatible membranes in resonance modes. Several aspects were covered : a simple and fast design method relying on Matlab implementation and simple Comsol Multiphysics simulation checks, fabrication techniques exploration to underline some key parameters and a characterization of the obtained samples using laser vibrometry to observe the frequency response of the samples and their mode shapes. These methods can be integrated in full pressure sensor design and fabrication process for any type of transduction. The final words of this text can be : stress should always be under control.

Appendix A : Alternative process using LPCVD

This Appendix describes the alternative process that could have been done to compare PECVD with LPCVD in the process of controlling the residual stresses in a stack.
This stack is similar to the one in proposed in [31, 37] but has been modified to ensure the global equivalent residual stress in the stack is 50MPa.
The chosen stack in this case is an ONO stack, such as represented in Figure 4.5, with :

- bulk SiO2 : 400 nm thick layer of wet thermally oxidised silicon dioxide with a compressive residual stress of 300MPa
- Si3N4 : 200 nm thick layer of LPCVD deposited silicon nitride with a tensile residual stress of 1GPa
- SiO2 : 400 nm thick layer of PECVD silicon dioxide, with a compressive stress of 70MPa

The process for this stack is given in Table A.1. The illustrated process is very similar to type A that is presented in Figure5.7 with an additionnal layer of silicon dioxide on top of the stack. The final fabricated die is displayed in Figure A.1.

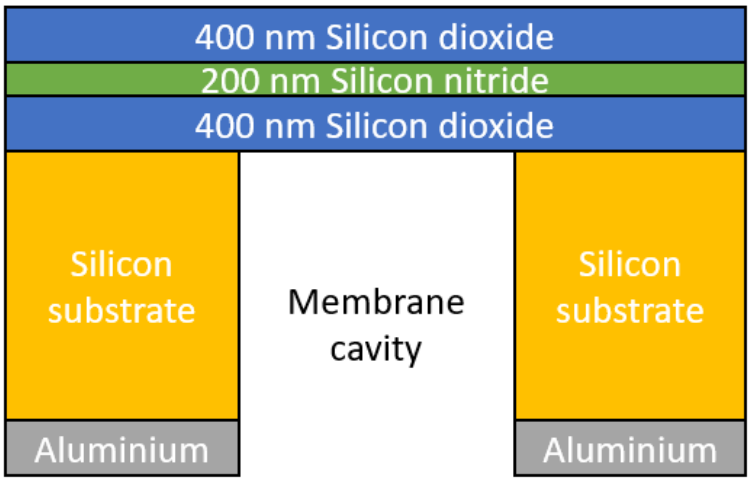

Figure A.1: *Final membrane structure for Type C process*

Step	Process step type	Type C
M0	Palmer	x
M1	Dektak 5500mm, 60s	x
1	Standard cleaning with HF bath	x
2	Wet Thermal Oxidation in Koyo 1 furnace	400 nm
M2	Ellipsometer	x
4	Protective blue resist coating 3000rmp, bake at 120°C for 90s	x
5	Backside SiO2 stripping in BHF bath	x
6	Protective resist stripping in Barrel (10 min from 200 to 500W)	x
M3	Dektak 5500mm, 60s	x
7	Si3N4 deposition in LPCVD Koyo furnace	200nm
M4	Ellipsometer	x
M5	Dektak 5500nm, 60s	x
8	Stress increase in the Si3N4 layer	x
M6	Dektak 5500nm, 60s	x
9	SiO2 deposition in PECVD Oxford chamber	400nm
10	Stress annealing in Tempress furnace 800°C for 30min, 0.5L/s N2	x
M7	Dektak 5500mm, 60s	x
11	Aluminium metalisation of backsides in VST	500nm
12	LPIII and backside AZMIR resist coating 4000rpm, 90°C 90s	x
13	Lithography with designed membrane mask 200W 2s	x
14	Lithography development and post-exposure bake 120°C 90s	x
M8	Lithography check on microscope	x
15	Aluminium etching in H3PO4, 2min 30s	x
16	Backside resist stripping in Barrel (10 min from 200 to 500W)	x
17	Frontside protective resist coating 3000rpm, bake at 130°C for 120s	x
18	Dicing	x
19	Die gluing on wafer	x
20	Deep RIE of Si layer in Oxford etching chamber	Full layer
M9	Dektak measurement of the etched membrane	x
20	Release of the die in acetone	x

Table A.1: *Process sheet for Type C stack*

Bibliography

[1] Klaus Schon. *High Voltage Measurement Techniques*. Power Systems. Springer, 2019. ISBN 978-3-030-21770-9. https://dial.uclouvain.be/ebook/object/ebook:130724.

[2] *International standard IEC60270 : High-voltage test techniques – Partial discharge measurements*. International Electrotechnical Commission, Switzerland, 2000.

[3] Bill Higinbotham. Partial discharges causes, effects and online detection techniques. https://www.youtube.com/watch?v=ae7JLrdKxgY&ab_channel=EATechnology.

[4] HVTechnologies Inc. The basics of partial discharge testing. https://hvtechnologies.com/the-basics-of-partial-discharge-testing/.

[5] EATechnology. Why is partial discharge important? https://www.youtube.com/watch?v=CqHZ5jIct4s&ab_channel=EATechnology, accessed Aug. 5, 2021.

[6] L E Lundgaard. Partial discharge - part XIV: Acoustic partial discharge detection -practical application. B(5):10, .

[7] M.D. Judd and O. Farish. High bandwidth measurement of partial discharge current pulses. In *Conference Record of the 1998 IEEE International Symposium on Electrical Insulation (Cat. No.98CH36239)*, volume 2, pages 436–439. IEEE. ISBN 978-0-7803-4927-8. doi: 10.1109/ELINSL.1998.694827. URL http://ieeexplore.ieee.org/document/694827/.

[8] L E Lundgaard. Partial discharge - part XIII: Acoustic partial discharge detection -fundamental considerations. 8(4):7, .

[9] Qi-Chao Chen, Wei-Chao Zhang, and Hong Zhao. Response bandwidth design of fabry-perot sensors for partial discharge detection based on frequency analysis. 2019:1–11. ISSN 1687-725X, 1687-7268. doi: 10.1155/2019/1026934. URL https://www.hindawi.com/journals/js/2019/1026934/.

[10] Xiaodong Wang, Baoqing Li, Zhixiong Xiao, Sang Hwui Lee, Harry Roman, Onofrio L Russo, Ken K Chin, and Kenneth R Farmer. An ultra-sensitive optical MEMS sensor for partial discharge detection. 15(3):521–527, . ISSN 0960-1317, 1361-6439. doi: 10.1088/0960-1317/15/3/012. URL https://iopscience.iop.org/article/10.1088/0960-1317/15/3/012.

[11] Michał Kunicki, Andrzej Cichoń, and Sebastian Borucki. Study on descriptors of acoustic emission signals generated by partial discharges under laboratory conditions and in on-site electrical power transformer. 41(2):265–276. ISSN 2300-262X. doi: 10.1515/aoa-2016-0026. URL http://journals.pan.pl/dlibra/publication/116596/edition/101347/content.

[12] Kulite. Kulite | the leader in pressure transducer technology. https://kulite.com, accessed Dec. 23, 2020.

[13] UE Systems. Ultraprobe 9000 atex. https://www.uesystems.com/engb/product/ultraprobe9000atex/atex/, accessed Dec. 23, 2020.

[14] R Horstink. How ultrasound can detect electrical discharge non-invasively and help eliminate arc flash incidents. page 5. IEEE.

[15] Robert D. Belvins. *Formulas for natural frequency and mode shape*. Krieger Publishing Company, 1993. ISBN 978-1575241845.

[16] V. Kaajakari. *Practical MEMS*. Small Gear Publishing, 2009. ISBN 978-0-9822991-0-4. http://www.kaajakari.net/PracticalMEMS/.

[17] EPFLx memsx. Micro and nanofabrication (mems). https://learning.edx.org/course/course-v1:EPFLx+memsX+3T2017/home, accessed July 15, 2021.

[18] Minhang Bao. *Analysis and Design Principles of MEMS Devices*. Elsevier Science, 2005. ISBN 9780080455624.

[19] Thibault P. Delhaye, Nicolas Andre, Laurent A. Francis, and Denis Flandre. New universal figure of merit for embedded si piezoresistive pressure sensors. pages 1–1. ISSN 1530-437X, 1558-1748, 2379-9153. doi: 10.1109/JSEN.2020.3013017. URL https://ieeexplore.ieee.org/document/9153028/.

[20] G Szego. On membranes and plates. 36(3):210–216. doi: 10.1073/pnas.36.3.210.

[21] Laurent Francis. *Thin film acoustic waveguides and resonators for gravimetric sensing applications in liquid*. Phd thesis, Université Catholique de Louvain, 2006.

[22] P. Peyla. Buckling of a compressed elastic membrane: a simple model. 48(3):379–383. ISSN 1434-6028, 1434-6036. doi: 10.1140/epjb/e2005-00415-9. URL http://link.springer.com/10.1140/epjb/e2005-00415-9.

[23] C R Helms and E H Poindexter. The silicon-silicon dioxide system: Its microstructure and imperfections. 57(8):791–852. ISSN 0034-4885, 1361-6633. doi: 10.1088/0034-4885/57/8/002. URL https://iopscience.iop.org/article/10.1088/0034-4885/57/8/002.

[24] D. Hiller, R. Zierold, J. Bachmann, M. Alexe, Y. Yang, J. W. Gerlach, A. Stesmans, M. Jivanescu, U. Müller, J. Vogt, H. Hilmer, P. Löper, M. Künle, F. Munnik, K. Nielsch, and M. Zacharias. Low temperature silicon dioxide by thermal atomic layer deposition: Investigation of material properties. 107(6):064314. ISSN 0021-8979, 1089-7550. doi: 10.1063/1.3327430. URL http://aip.scitation.org/doi/10.1063/1.3327430.

[25] Bharat Bhushan, S.P. Murarka, and Jeff Gerlach. Stress in silicon dioxide films deposited using chemical vapor deposition techniques and the effect of annealing on these stresses. 8(5):1068. ISSN 0734211X. doi: 10.1116/1.584918. URL http://scitation.aip.org/content/avs/journal/jvstb/8/5/10.1116/1.584918.

[26] K D Mackenzie, D J Johnson, M W DeVre, R J Westerman, and B H Reelfs. Stress control of si-based PECVD dielectrics. pages 148–159. Electrochemical Society.

[27] M. F. Ceiler, P. A. Kohl, and S. A. Bidstrup. Plasma-enhanced chemical vapor deposition of silicon dioxide deposited at low temperatures. 142(6):2067–2071. ISSN 0013-4651, 1945-7111. doi: 10.1149/1.2044242. URL https://iopscience.iop.org/article/10.1149/1.2044242.

[28] Onursal Onen, Lynford Davis, Christopher Nelson, and Rasim O. Guldiken. Thermal stresses on membrane based microdevices. 16(11):1967–1973. ISSN 0946-7076, 1432-1858. doi: 10.1007/s00542-010-1130-9. URL http://link.springer.com/10.1007/s00542-010-1130-9.

[29] Omar Zohni, Gregory Buckner, Taeyun Kim, Angus Kingon, Jeff Maranchi, and Richard Siergiej. Investigating thin film stresses in stacked silicon dioxide/silicon nitride structures and quantifying their effects on frequency response. 17(5):1042–1051. ISSN 0960-1317, 1361-6439. doi: 10.1088/0960-1317/17/5/026. URL https://iopscience.iop.org/article/10.1088/0960-1317/17/5/026.

[30] Nan Wang, Jinghui Xu, Xiaolin Zhang, Guoqiang Wu, Yao Zhu, Wei Li, and Yuandong Gu. Methods for precisely controlling the residual stress and temperature coefficient of the frequency of a MEMS resonator based on an AlN cavity silicon-on-insulator platform. 26(7):074003, . ISSN 0960-1317, 1361-6439. doi: 10.1088/0960-1317/26/7/074003. URL https://iopscience.iop.org/article/10.1088/0960-1317/26/7/074003.

[31] N André, T P Delhaye, M Al Kadi Jazairli, B Olbrechts, P Gérard, L A Francis, and D Flandre. Ultra-low-power SOI CMOS pressure sensor based on orthogonal PMOS gauges. In *Ultra-low-power SOI CMOS pressure sensor based on orthogonal PMOS gauges*, page 6. IMEKO. URL http://hdl.handle.net/2078.1/189404.

[32] Chen Zhou, Yanmin Zhang, Beirong Zheng, Wei Xue, and Quan Wang. Effect of internal stress on nonlinearity and sensitivity of a pressure sensor with SiN composite diaphragm. 381(4):284–291. ISSN 03759601. doi: 10.1016/j.physleta.2016.10.024. URL https://linkinghub.elsevier.com/retrieve/pii/S0375960116307769.

[33] Daniel A. Russell. Vibrational modes of a circular membrane. https://www.acs.psu.edu/drussell/demos/membranecircle/circle.html, Accessed Aug. 11, 2021.

[34] AZO Materials. Silica - silicon dioxide (sio2), . https://www.azom.com/properties.aspx?ArticleID=1114, Accessed Aug. 12, 2021.

[35] AZO Materials. Silicon nitride (si3n4) properties and applications, . https://www.azom.com/properties.aspx?ArticleID=53, Accessed Aug. 12, 2021.

[36] Jean Laconte. *Micromachined Thin-film sensors for SOI-CMOS co-integration*. Phd thesis, Université Catholique de Louvain, 2004.

[37] B. Olbrechts, B. Rue, T. Pardoen, D. Flandre, and J.-P. Raskin. A novel approach for active pressure sensors in thin film SOI technology. 25:43–46. ISSN 18777058. doi: 10.1016/j.proeng.2011.12.011. URL https://linkinghub.elsevier.com/retrieve/pii/S1877705811056803.

[38] *Vibrating Membrane*. COMSOL Inc., Burlington, MA 01803, 2018. Tutorial, https://www.comsol.fr/model/vibrating-membrane-12587.

[39] *Failure Prediction in a Laminated Composite Shell*. COMSOL Inc., Burlington, MA 01803, 2020. Tutorial, https://www.comsol.fr/model/failure-prediction-in-a-layered-shell-48371.

[40] *Baffled Membrane*. COMSOL Inc., Burlington, MA 01803, 2018. Tutorial, https://www.comsol.fr/model/baffled-membrane-9771.

[41] Norihisa Hashimoto and Masahito Yasuoka. Natural frequencies of a plate, or a membrane, with an air layer. 13(3):187–193. ISSN 0388-2861, 2185-3509. doi: 10.1250/ast.13.187. URL http://www.jstage.jst.go.jp/article/ast1980/13/3/13_3_187/_article.

[42] J.C. Wyant. *Interferometry*, pages 351–356. Elsevier, Duke University, Durham, NC, USA, 2005. ISBN 978-0-12-369395-2. doi: 10.1016/B0-12-369395-0/00693-X.

[43] Polytec GmbH. Basic priciples of scanning white-light interferometry, . https://www.polytec.com/eu/surface-metrology/technology/white-light-interferometry, accessed Aug. 11, 2021.

[44] S.J. Rothberg, M.S. Allen, P. Castellini, D. Di Maio, J.J.J. Dirckx, D.J. Ewins, B.J. Halkon, P. Muyshondt, N. Paone, T. Ryan, H. Steger, E.P. Tomasini, S. Vanlanduit, and J.F. Vignola. An international review of laser doppler vibrometry: Making light work of vibration measurement. 99:11–22. ISSN 01438166. doi: 10.1016/j.optlaseng.2016.10.023. URL https://linkinghub.elsevier.com/retrieve/pii/S0143816616303724.

[45] Polytec GmbH. Basic principles of laser doppler vibrometry, . https://www.polytec.com/eu/vibrometry/technology/laser-doppler-vibrometry, accessed Aug. 11, 2021.

[46] C Gao, D Halim, and C Rudd. Vibration absorption performance of membrane-type metamaterial on a thin plate. In *Vibration absorption performance of membrane-type metamaterial on a thin plate*, page 6. inter.noise. URL https://www.researchgate.net/publication/341576220_Vibration_absorption_performance_of_membrane-type_metamaterial_on_a_thin_plate.

[47] E. Suhir. An approximate analysis of stresses in multilayered elastic thin films. 55 (1):143–148. ISSN 0021-8936, 1528-9036. doi: 10.1115/1.3173620. URL https://asmedigitalcollection.asme.org/appliedmechanics/article/55/1/143/390028/An-Approximate-Analysis-of-Stresses-in.

[48] C.H. Hsueh. Thermal stresses in elastic multilayer systems. 418(2):182–188. ISSN 00406090. doi: 10.1016/S0040-6090(02)00699-5. URL https://linkinghub.elsevier.com/retrieve/pii/S0040609002006995.

[49] W Z Yao, F Roqueta, J C Craveur, S Belhenini, P Gardes, and A Tougui. Modelling and analysis of the stress distribution in a multi-thin film system pt/USG/si. 5(4):046405. ISSN 2053-1591. doi: 10.1088/2053-1591/aaba4b. URL https://iopscience.iop.org/article/10.1088/2053-1591/aaba4b.

[50] Yan Shi, John A. Rogers, Cunfa Gao, and Yonggang Huang. Multiple neutral axes in bending of a multiple-layer beam with extremely different elastic properties. 81(11):114501. ISSN 0021-8936, 1528-9036. doi: 10.1115/1.4028465. URL https://asmedigitalcollection.asme.org/appliedmechanics/article/doi/10.1115/1.4028465/370114/Multiple-Neutral-Axes-in-Bending-of-a.

UNIVERSITÉ CATHOLIQUE DE LOUVAIN
École polytechnique de Louvain
Rue Archimède, 1 bte L6.11.01, 1348 Louvain-la-Neuve, Belgique | **www.uclouvain.be/epl**